Optimisation de Contrôle Commande des Systèmes de Génération d'Electricité à Cycle de Relaxation

Mariam Ahmed

UNIVERSITÉ DE GRENOBLE

THÈSE

pour obtenir le grade de

DOCTEUR DE L'UNIVERSITÉ DE GRENOBLE

Spécialité: Génie Électrique

Arrêté ministériel : 7 août 2006

Présentée par

Mariam Samir AHMED

Thèse dirigée par **Prof. Seddik BACHA** et

coencadrée par **Dr. Ahmad HABLY**

préparée au sein du

Grenoble Génie Électrique Laboratoire (G2ELAB)

En collaboration avec

Grenoble Images Parole Signal Automatique Laboratory (GIPSA-Lab)

dans l'**École Doctorale:Electronique, Electrotechnique, Automatique, Télécommunication et Signal**

Optimisation de Contrôle Commande des Systèmes de Génération d'Électricité à Cycle de Relaxation

Thèse soutenue publiquement le **28 Février 2014**,

devant le jury composé de:

M. Brayima DAKYO

Professeur à l'Université du Havre, France, Président

M. Mohamed BENBOUZID

Professeur à l'Université de Brest, Rapporteur

M. Rachid OUTBIB

Professeur à l'Université d'Aix-Marseille, France, Rapporteur

M. Lorenzo FAGIANO

Scientist at ABB Corporate Research, Switzerland, Examinateur

M. Garrett SMITH

Président et COO de Cosmica Spacelines, Examinateur

M. Seddik BACHA

Professeur à l'Université Joseph Fourier, Directeur de thèse

M. Ahmad HABLY

Maître de Conférences à Grenoble INP, Co-encadrent de thèse

Dédié à la Syrie

Acknowledgment

Three years of my life went by, three years that shaped a new future for me, a future I didn't know has been waiting for me. More than a scientific research trip, these years were a journey full of emotions, happiness, stress, homesickness and love. The journey wouldn't have end successfully without the support, directly or indirectly, of many people that I would like to thank here.

Firstly, I would like to thank the thesis jury members I was honored to have to help conclude this work: Mr.Dakyo the president of the jury, and Mr.Benbouzid and Mr.Outbib for their feedback and proofreading of the manuscript. Also I would like to thank Mr.Fagiano for making part of the jury and offering his expertise in the novel field of kite-based systems, as well as Mr.Smith for the passionate discussions on renewable energy we had.

Back to 2010, For my master internship I was honored to work under the guidance of Professor Seddik BACHA, Professor Daniel Roye and Mathieu Hauk a PhD student at the time in the Electrical Engineering Laboratory G2ELAB. They introduced me to a very innovative interesting subject! Using kites to generate electricity! I was completely concurred and when a PhD was proposed to continue on the same idea I jumped at the opportunity. I'm very grateful to having worked with M.Bacha et M.Ahmad Hably during my PhD, who I thank for their guidance and patience.

My gratitude goes to the staff of G2ELAB and GIPSA-Lab for the scientific friendly environment they offer, in addition to their help and guidance in the administration work.

Further, I would like to thank M.Gérard Meunier for welcoming me and helping me join the Master 2R - Génie Electrique in INP, as well as my master friends who helped me catch up with them (being 2 months late for the course), we spent a great time preparing for exams, eating and partying together: Ionela, Minh, Christina, Julian, Luiz, Lyubo, Soul, Loic, thanh, and Hai, thank you so much. I won't talk about this period without having a thought for my friend Moustafa to whom I own my deepest gratitude, he helped me settle down in Grenoble and taught me about adminstration work, university system among other things. Thank you Moustafa for everything.

Thanks to the thesis, I had the chance to be part of the OPLAT association with which

I spent a great year organizing activities in the lab, as well as the ZIK music group that was a relaxing escape during the hardest times. The thesis brought me also a great group of friends that I'm counting on keeping them forever: Nathalie, Raha, Angelina, Soulafa, Rachelle, Sinan, Antony, Bibi, and many other.

The best that the thesis has done was allowing me to meet my colombian soul mate José, something I wasn't expecting at all when I first arrived to France. He was always there for me during both the happy and the sad moments. I would never be where I am now without you by my side. Thank you Josito for introducing me to your lovely family that I'm so proud to call mine.

My heart goes to my parents in Aleppo. My father who walked me, a little girl of five years old, and pointed stars to me and explain how the universe works in simple inspiring words. He would hand me over scientific books and teach me about electricity and statistics when I was eight. He planted the passion for science in my heart and always encouraged me to follow this passion. Thank you mom for your encouragement and patience, I remember when I tried to help her with the house work she would always tell me to concentrate on my studies and that I "will have the time to worry about these stuff later" even though she would have used some help being a working mom of four children, I wish to have half the energy you have when I become a mother. This work is dedicated to you dad and mom. Thank you my little brothers: Ahmad, Obada and Amr, for always supporting my decisions and enforcing my confidence by looking up to me and making me feel specially perfect for them.

Contents

List of Figures

List of Tables

List of Acronyms

AWE	Airborne Wind Energy
DCM	Direct Current Machine
HPS	Heaving Point-absorber System
HAWE	High Altitude Wind Energy
KGS	Kite Generator System
NMPC	Nonlinear model predictive Control
OECD	Organization for Economic Co-operation and Development
PHIL	Power Hardware In the Loop
PA	Point Absorber
SM-PM	Synchronous Machine with Permanent Magnets
VCC	Virtual Constraints-based Control
WEC	Wave Energy Conversion

List of Notations

Kite Generator System

A	Kite's area
A_c	Tether crosswind area
C_L	Lift coefficient
C_D	Drag coefficient
C_{dt}	Tether's drag coefficient
C_R	Kite's resistive torque
$\vec{e}_r$	Unit vector in the kite's tether direction
$(\vec{e}_r, \vec{e}_\theta, \vec{e}_\phi)$	Kite spherical coordinates
$\vec{e}_p$	Unit vector following $\vec{W}_e^p$
$\vec{e}_o$	Perpendicular on $(\vec{e}_r, \vec{e}_p)$ plan
F_{grav}^t	Tether's weight
F_{aer}^t	Aerodynamic force
$F^{c,trc}$	Tether's traction force
$\vec{F}^{grav}$	Gravity force
$\vec{F}^{app}$	Apparent force
$\vec{F}^{aer}$	Aerodynamic force
$\vec{F}_L$	Lift force
$\vec{F}_D$	Drag force
$\vec{F}^{c,trc}$	Tether traction force
γ	Surface friction coefficient
g	Gravity acceleration
$\vec{\gamma}$	Kite acceleration
G_e	Kite aerodynamic efficiency coefficient
J_0	Normalized mean generated power
L	$\vec{W}_e^p$ amplitude
μ	Mass per length unit
m	Kite's mass
Ω_S	Rotor rotational velocity
ψ	Kite's roll angle
P_M	Mean generated power

R	Rotor diameter
r_0	Initial tether's length
ρ_a	Air density
T	Orbit's period
θ	Tethers inclination angle
v	Normalized tether radial velocity
V	Wind speed
V_L	Radial velocity
$V_{\|\|}$	Crosswind speed
$\vec{W}_e$	Effective wind speed
$\vec{W}_e^p$	Effective wind projection on $(\vec{e}_\theta, \vec{e}_\phi)$ plan
$w_{\|\|}$	Normalized crosswind velocity
x	Kite's state vector
$\vec{x}_w$	Unit vector carried on the kite longitudinal axis
$\vec{y}_w$	Unit vector carried on the line connecting the kite's tips
$\vec{z}_w$	Perpendicular on the kite surface and directed upwards
z	Altitude

Heaving Point-absorber System

ρ	Water density
H	Wave amplitude
T	Wave period
h	Sea depth
$S^i(w)$	Wave power spectrum
λ	Wave length
d	Point-absorber diameter
E_w	Wave energy
V	Point-absorber volume
P_{av}	Average power
P_{max}	Maximum power
C_G	Generator torque
P_A	Optimum destructive interference power
P_B	Budal upper limit power
P	Pressure on the floating point-absorber
B	Fluid's external acceleration
μ	Fluid's viscosity coefficient
V	Fluid velocity field
ϕ_I	Wave proper potential
ϕ_D	Diffraction scalar potential
ϕ_R	Radiation scalar potential
$\vec{n}$	Unit normal vector on the floating body surface
S	Body's surface
$\vec{r}$	Unit rotational vectors

m	Floating body mass
m_r	Added mass
R_r	Radiation damping coefficient
z	Point-absorber translation
v	Point-absorber translation velocity
F_{ex}	Excitation force
$Z(t)$	Sea surface elevation
$\hat{A}_n$	Normal distribution random wave amplitude
T_n	Normal distribution random wave period
S	Power spectrum
R_{PTO}	Power take-off

Power Transformation Chain

C_G	Generator torque
C_{DC}	DC-bus filtering capacitor
D	Damping factor estimation
$e_{sk} : k = a, b, c$	Electromagnetic force voltage source in Behn-Eschenburg machine model
$\bar{\phi_{fs}}$	Induced flow vector
$\bar{i_s}$	Stator currents' vector
$\bar{i_G}$	Grid currents' vector
$I_{DC_{REC}}$	Machine converter output current
I_{DC}	DC bus current
J	Total inertia of kite, drum; and machine's rotor
K	Gearbox factor
K_p	Proportional gain
K_i	Integral gain
L_s	Inductance in Behn-Eschenburg machine model
ω	Machine's electric pulsation
ω_G	Electric grid pulsation
ω_n	Resonant pulse of the injected currents harmonies
p	Poles' pairs number
R_s	Resistance in Behn-Eschenburg machine model
R_f, L_f	Loss and filtering components
R_{DC}	DC-bus resistance
T_i	Corrector time constant
U_{DC}	DC bus voltage
$\bar{v_s}$	Stator voltages' vector
V_G	Grid RMS voltage

Power Hardware-In-the-Loop

C_{DCM}	DC-Machine torque
C_{cor}	Correction torque
J_E	Total inertia of the DCM and PMSM rotor
D_E	Damping factor estimation between DCM and PMSM
Ω_E	Rotor rotation velocity

General Introduction

Answering for the growing demand for energy and the expectations of oil depletion, as well as, reducing the negative effects of human's industrial and technological advance on earth's climate are some of the most important issues facing us at present. One of the major challenges is how to decarbonize the electric grid by eliminating fuel-based electricity generators, and replacing them, preferably, by green and publicly accepted resources. That is where renewable energy resources rise as a promising solution.

Lately, renewable energy has been undergoing a lot of research and development, that aims at solving renewable resources problems such as efficiency and grid integration, and exploring new methods and structures to exploit them. The later research axis led to the birth of *relaxation-cycle renewable energy systems*. Those have a periodic power cycle with two phases:

- A generation phase during which the system is working in its "power" region, and this enables it to generate electricity until it reaches its boundaries.
- A recovery phase that resets the system's state to start a new generation phase, and consumes energy while doing so.

Hence, an optimization operation is required to insure the consumed energy's minimization and the generated energy's maximization.

Relaxation-cycle renewable energy systems are the interest of this thesis. In particular, two examples of those are considered case studies. The first is the kite generator system (KGS). It is a solution proposed to extract energy from the steady and strong wind found in high altitudes. Its operation principle is to mechanically drive a ground-based electric generator using one or several tethered kites. The second case study is the heaving point-absorber system (HPS), which is a floating wave energy system that employs wave oscillations to turn an electric generator and generate electricity.

In addition to the classic problems accompanying renewable energy resources, those with relaxation-cycles are a very interesting field of open challenges, such as finding solutions to multi-dimensional optimization problems, and grid integration of their alternating output power. Those challenges are addressed in this thesis realized in Grenoble Electrical Engineering laboratory (G2ELab) with collaboration with Grenoble Image Parole Signal Automatique laboratory (GIPSA-Lab). The thesis is organized in four chapters:

The first chapter presents the *Relaxation Cycle Renewable Energy Systems*. It introduces the thesis subject and key words. It includes a brief overview on energy history, current situation and expectations, in addition to presenting the new technologies in the field of wind and wave energy while concentrating on those with relaxation cycles. The chapter also states the problems handled and the challenges confronted in the thesis, in addition to listing the objectives.

The second chapter handles the *Structure and Modeling* of two relaxation-cycle systems. Those are the kite generator system and the heaving point-absorber system. Simplified structures of both systems are presented and modeled. Their relaxation cycle is defined and methods to maximize their generated power are listed. A comparison shows the resemblance between both, and only the KGS is considered in the rest of the thesis.

The third chapter deals with the *Kite Generator System Supervision*. Here, two strategies to optimize and to control the KGS are proposed. Those strategies are based on a nonlinear model predictive controller (NMPC) and virtual constraints-based controller (VCC).

The last chapter is about the *Kite Generator System Grid Integration and Control Validation*. The topology applied to grid integrate the KGS or use it to supply an isolated load is modeled and controlled. Afterwards, the proposed control functioning is insured through simulations and experimental validation. It is achieved via testing on a power hardware-in-the-loop simulator which is real-time hybrid simulation system.

Chapter I

Relaxation Cycle Renewable Energy Systems

Contents

Abstract

Triggered by the fear of oil depletion and dependence, an intensive research on alternative to fossil fuels is going on recently. A huge part of this research is concerning renewable energy resources, and looks for new methods and technologies to improve their integration. An interesting and particular group of renewables assembles systems with relaxation cycles. Such systems need to regain periodically a state that allows energy production, which results in a recovery phase that consumes energy, hence a generation-consumption cycle is created and should be optimized to maximize the system's average produced power.

This first chapter presents the thesis main key words: Renewable energy, in particular wind and wave energy, and relaxation cycle systems. It introduces, as well, the problems handled and the objectives of this PhD dissertation.

I.1 Introduction

Modern civilization is very energy dependent, especially on its non-renewable resources that are expected to run out sooner or later, and shortly will not be able to satisfy the growing energy demand. The global demand in 2010, of which 86.5% is covered by fossil fuels [Pet10], is expected to increase by 40% in 2030. An increase that will not be accompanied by a similar growth in fossil fuels production, and even if it does, new fossil fuels fields will be much harder to be dug out and exploited thus much more expensive. Thereby, demand increase must be covered by other energy sources.

In addition, fossil fuels consumption should be limited as their usage is accompanied by emitting huge amounts of Carbon Dioxide CO_2 which endangers the earth climate by its greenhouse effect [IEA11].

Renewable energy resources, such as solar, wind and tidal[1] systems, rise as a very promising ideal clean solution to cover for fossil fuels decline. Nonetheless, renewable energy generation is accompanied with a lot of scientific challenges, such as substitutability and intermittency [Fri10].

The major interest in sustainable development and the continuous research for new renewable energy exploitation systems have led to the birth of a new family of systems: Those with relaxation-cycles. A relaxation-cycle system produces energy until it reaches certain limits after which it must recover a state that allows it to reproduce, this recovery operation could consume energy. Examples of those are: Kite-based traction and tidal systems that uses waves or swell energy.

All renewable energy systems are more or less intermittent, but do not have major issues in terms of control. The problem is rather in improving their integration into the electric grid technically and economically. However, when considering power generation system with relaxation periodic phases, new difficulties are added. Firstly, providing the needed power during the recovery phase, and secondly, controlling the system's generation/consumption cycle in order to recover the maximum possible energy. This should be achieved while considering the constraints on the system itself, the primary source of energy, and grid loads.

In this first chapter, the thesis subject and objectives are introduced. It starts by an introduction on renewable energy history and expectations. Among the different investigated renewable resources, a couple is addressed in detail in Sections.I.3 and I.4: Wind Energy and Wave Energy. Classic and innovative methods to extract these energies are presented and compared, and examples of structures that employ the notion of relaxation cycles are as well introduced.

Section.I.5 presents the relaxation-cycle system's concept supported by some examples. Next, the problem's statements and challenges, and the work objectives are addressed in Section.I.6.

[1] Tidal Systems should not be confused with the conventional hydraulic systems.

I.2 Renewable Energy

Renewable energy is the oldest exploited form of energy, starting from using wind energy to drive sail boats along the Nile more than 7500 years ago, and replacing man and animal effort by vertical wind mills in the middle east in $200BC$, and by Norias[2] (Fig.I.1) in Syria in $469AD$ [Bur63]. In Europe, windmills were the essential energy resource that supplied industry in the 12^{th} century. Fig.I.2 displays a time chart of some of the important events in the history of energy.

Figure I.1: Norias on the Orontes river in Syria

The development in renewable energy systems stopped and renewable resources became secondary in the 17^{th} century, because of the arrival and the domination of coal. Coal was the main reason for the industrial revolution in Europe around 1760. It fed steam machineries and trains at the time, and later, in 1881, was used in first electrical power generation plants[3].

The "Coal peak", in 1873, created a fear of coal depletion, which regained renewable energy attention back. The years 1883 to 1891 witnessed many discoveries that contributed to solar energy evolution, and in 1891 the first solar cell appeared and the first solar heater was introduced. Furthermore, in 1887 a windmill was used to produce electricity for the first time.

Renewable energy resources were diminished again by the arrival of oil and natural gas at the beginning of the 20^{th} century. Since then, fossil fuels are being heavily exploited in order to keep pace with the huge technological and industrial development the twentieth century had witnessed.

The problem is that fossil resources have

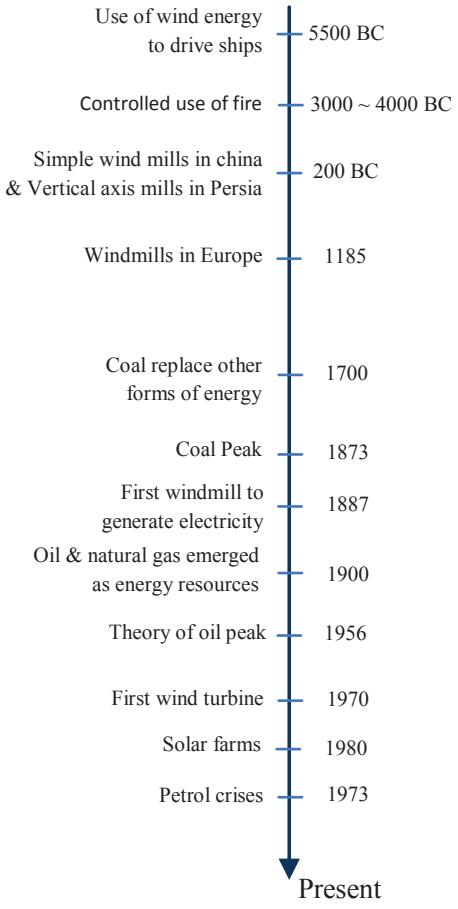

Figure I.2: Important events in the history of energy.

[2] Comes from the Arabic word Naaurah meaning the first water machine

[3] The very first electricity plant was a hydroelectric facility built on Niagara falls.

been generated and stored underground since the birth of earth, billions of years ago, and are decreasing very fast that they will soon come to an end. This issue, in addition to some governments taking advantage of their fossil fuels and using it as a pressure to control international policy, has encouraged research to reconsider renewable energy as the future energy resource in fear of oil depletion and dependence.

In the following, the current and future energy situation and the results of the current energy policy are discussed. As well as, some statistics on renewable and non-renewable energy evolution are presented.

I.2.a Global Energy Situation and Expectations

Many studies are carried on to predict future energy situation, and answer the questions:

- How long oil will be able to satisfy its demand?
- Will this demand continue to grow?

Those studies take into account many different variables [Fin08], such as proved reserve, expected population growth and economy evolution. They all agree on two points: First, the oil peak, or what is referred to as "Peak of the Oil Age", if has not already occurred, it will very soon, some claims before 2020 [AHJ10]. Secondly, oil will become much more expensive, as it will be much deeper and more difficult to be extracted [HR11], and its production will not meet the demand level.

In addition to limited future availability, fossil fuels are endangering the earth's climate, because of their CO_2 emissions. The emissions have already changed the earth climate dramatically during the last ten years due to global warming effect [IEA11]. Fig.I.3 shows how CO_2 emissions have increased in the last two decades [Pet10]. Moreover, they are expected to grow 26% in 2030, according to the BP 2013 report, if the current global energy strategy were still adapted.

The use of fossil fuels is a serious problem, not only economically and climate wise; but on the humanitarian side as well, as its lack has and will enhance wars. These threats to our earth have led to research replacing fossil fuels dependent machinery to electricity dependent ones; an electricity that is produced in a nature-friendly procedure.

One non-fossil energy resource once considered very promising for future energy, is nuclear energy. This resource, however, is facing many accusations considering its safety and cleanness. These accusations are now more intense after the recent Fukushima Daiichi nuclear disaster on March 2011 [Str11], which raised serious doubts about the future of nuclear energy.

All mentioned points led to considering renewable energy resources, such as biomass, geothermal, solar photo-voltaic, solar thermodynamic, wind and tidal systems, as they offer the safest and cleanest type of energy.

Fig.I.4 shows the evolution of energy production distribution by energy resource according to the BP[4] energy outlook released in 2011[Pet10]. Though fossil fuels are expected to

[4]The British Petroleum society

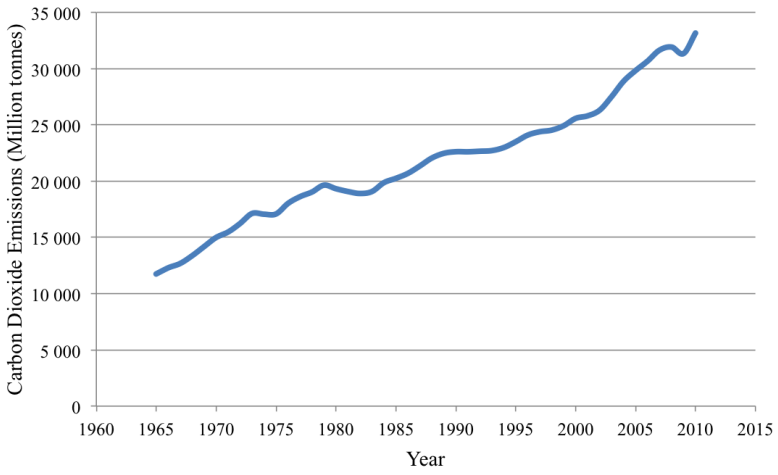

Figure I.3: CO_2 emissions evolution since 1965.

continue to supply the majority of energy demands in 2030, renewable resources (wind, biofuels, hydroelectricity,...) are expected to witness a huge relative increase in the coming decade. For instance, renewable energy share in global energy consumption is estimated to have risen from 11.78% in 2011 to 13.20% in 2012, which means an 11.74% rise, of which, renewables', other than hydro and bio-fuels, rise is estimated to 16.56% and have contributed 12.7% of world energy growth according to the latest statistics published by the BP society.

Moreover, extensive studies are ongoing on how to extract energy from natural renewable resources and transform and inject it in the electric grid in order to increase renewable energy partition in future energy.

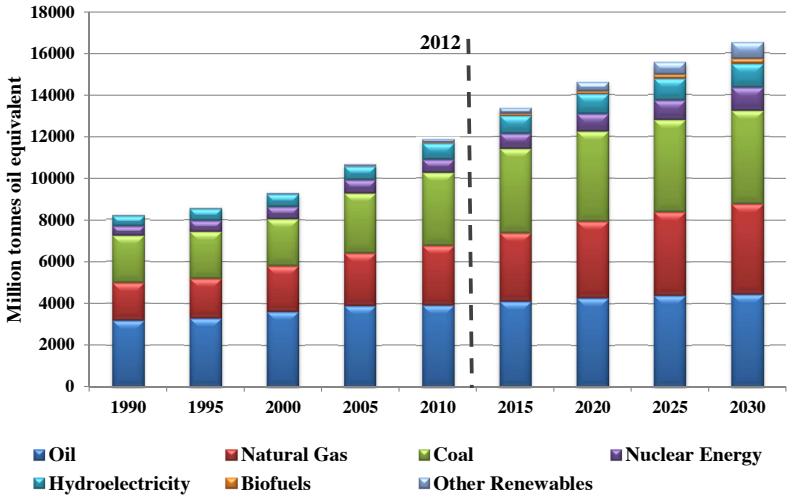

Figure I.4: Energy production history and expectations.

Another objective is to increase investments and awareness on this field of energy should be achieved, mainly in the Non-OECD (Organization for Economic Co-operation and Development) countries, whose share of energy demand is the largest according to Table.I.1.

This can be achieved through collaboration between OECD and non-OECD countries via sharing information and advancements in renewable energy extraction technologies.

Table I.1: Energy consumption development by region: OECD and Non-OECD (*Million tons oil equivalent*)

Year	1995	2000	2005	2010	2015	2020	2025	2030
Total Energy Demand	8578	9382	10801	12002	13360	14627	15635	16632
OECD	4992	5435	5667	5568	5571	5679	5729	5765
Non-OECD	3586	3947	5134	6434	7789	8948	9906	10867

It may be somehow late to provide the needed energy using only non-fossil energy resources, but it worth working on to minimize the disastrous results of fossil fuels draining off.

I.2.b Renewable Energy Evolution

When electricity was first being produced in the late 19th century [Mar13], a huge part was due to renewable energy resources, mainly hydroelectric facilities. Apart from hydroelectricity, renewable resources provided expensive electricity compared to fossil fuels based generators. For instance: In 1940 in the USA, one kWh of wind-based generated electricity cost 12 to 30 cents, while a fossil fuel-based generated electricity cost only 3 to 6 cents/kWh [KS46], this price even declined to below 3 cents/kWh in 1970. The big difference in prices led to ignore renewable energy resources for the sake of fossil fuels and very limited improvement was done in this field.

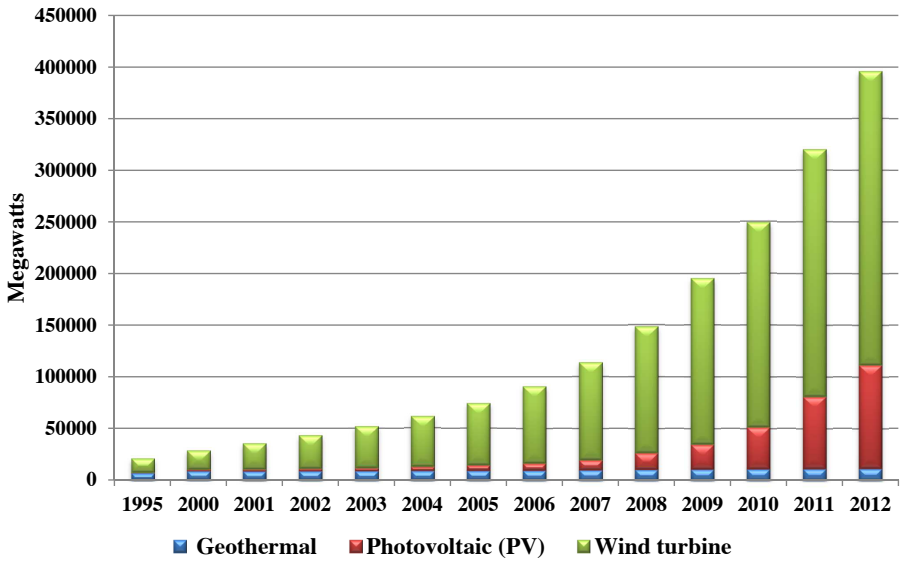

Figure I.5: Main renewable energy cumulative installed evolution between 1995 and 2012 (excluding hydro and bio-fuels).

The crisis of 1973, as well as realizing that fossil fuels might come to an end one day or

another, forced politicians to adapt new policies to limit fossil fuels dependence, which gained back attention to renewable resources and nuclear plants. Since then, huge effort, development and research in the field were achieved. Cost was reduced and renewable energy share in power consumption has grown 5 folds from 0.43% in 1990 to 4.7% in 2012. As shown in Fig.I.5, wind energy contributed to the most substantial increment. During the last decade, wind energy global capacity increased more than nine-fold, growing from 17.4 GW in 2000 to 158.6 GW in 2009 [AWE10]. That makes wind, not only the fastest growing renewable energy resource, but also the fastest growing electric power resource of all [AJ05].

In the following, wind energy is addressed, as well as wave energy. Though wave energy does not represent a significant resource at present, it is believed to hold an important part in the future energy as it offer a dense and a vastly available storage of energy, and can be exploited without scenery negative effects.

I.3 Wind Energy

Human efforts to harness wind energy date back to the ancient times. This energy was employed to sail ships, grind grains, and pump water thousands of years ago. The first time man thought about using wind for mechanical power is believed to be during the seventeenth century B.C when the Babylonian emperor Hammurabi planned to use wind power for an ambitious irrigation project. However, the earliest documented design of using wind's mechanical power to feed a machine is the wind wheel of the Greek engineer Heron of Alexandria (Fig.I.6) in the first century AD.

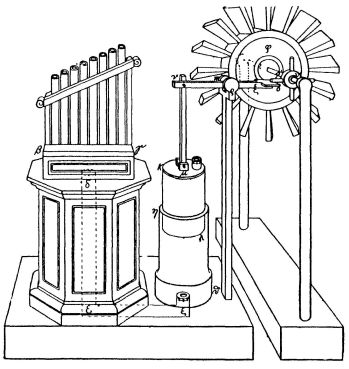

Figure I.6: Heron's wind wheel used to supply an organ[Dra61].

Wind is considered an ideal renewable energy resource, since it is infinitely sustainable and clean, which explains the global interest in exploiting its energy. In the following, wind power conversion technologies are briefly presented and compared.

I.3.a Conversion Technologies

In addition to classic wind turbines, other solutions are proposed to harness wind power, including floating turbines that aims at capturing the strong offshore wind and structures that works at high altitude where strong stable wind is available continually.

I.3.a-i Wind Turbines

Traditionally, wind energy is exploited using a wind turbine (See Fig.I.7). Wind turbines technologies has evolved an varied greatly during the last 3 decades, however, a conventional turbine is a two/three-blade rotor, that captures wind's kinetic energy. This is done by a direct, or through a gearbox, coupling with an electric generator. The turbine is connected to the electric grid directly or via a power-electronics interface. The turbine power is controlled by commanding the pitch and yaw blades angles. Notice that the eventual power electronics interface is exploited for this reason as well. The whole conversion chain and the blades' control unit are placed up next to the rotor hub, on the turbine's tower.

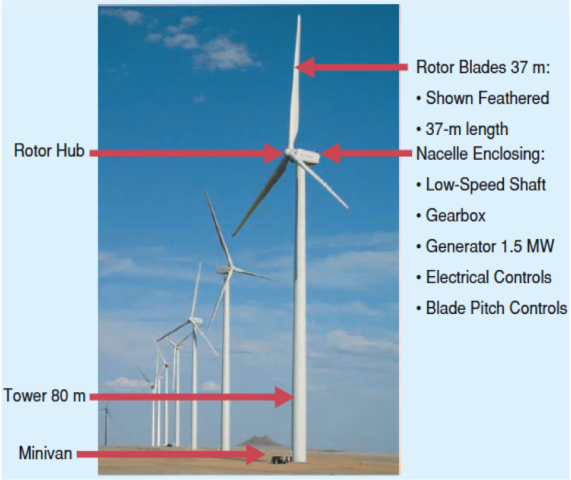

Figure I.7: A 1.5-MW wind turbine installed in a wind farm[TRV07].

Wind energy is written in eq.I.1, where ρ is the air density, A is the considered cross-sectional wind area, and V is wind speed.

$$P = \frac{1}{2}\rho A V^3 \tag{I.1}$$

Hence, following the development of wind turbine's industry, a trend to increase the size of the turbine is particularly clear. One aim of this increase is to reach higher altitudes where winds are supposed to be stronger and more stable since the aerodynamic friction of the earth surface slows down low altitude wind speed. This can be shown via the dependency function of wind speed V on altitude z:

$$V(z) = v_0(\frac{z}{z_0})^\gamma \tag{I.2}$$

where v_0 is the measured wind speed at an altitude z_0, and γ is a surface friction coefficient.

The other objective is to increase the blades size thus the turbine working area, thus A, with which the available wind power increases linearly (eq.I.1).

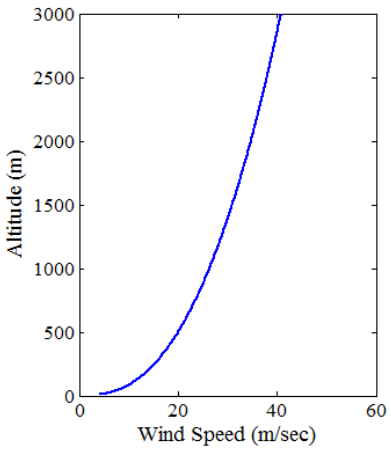

Figure I.8: Wind speed evolution with altitude above a flat open coast ($\gamma = 0.4$).

Nevertheless, turbine size is not expected to grow as dramatically in the future as it has in the past without significant technological advancement and change in the design [TRV07]. As well as, despite the improvements of wind turbines efficiency, according to Betz limit [Gam07], it can only extract a maximum 59% of the available energy in an air stream with the same area as its working area. Moreover, although modern turbines are designed to capture 80% of this maximum limit, in reality their efficiency is about $40 - 50\%$. Besides, the turbine does not produce its rated power continuously, due to wind irregularity.

To overcome these limitations, new axes of research have started. One solution is building "Floating turbines" that take advantage of strong and regular open-sea wind (See Fig.I.9). The down point of this solution is that it does not solve the problem of costly construction and maintenance. The other solution looks for new flying structures able to extract wind energy at high altitudes (HAWE) of about $400 - 2000m$.

Figure I.9: Off-shore wind turbine for the great lakes in Ontario-Canada [Flo10].

I.3.a-ii High Altitude Wind Energy Technologies

Several designs are proposed to harness HAWE, such as Air Rotor Systems, Airborne wind turbines and tethered airfoils (kites).

The principle of the air rotor systems developed by Magenn (MARS) Power Inc[Meg], shown in Fig.I.10, is as follows: a helium-filled balloon stationary at an altitude between $200m$ and $350m$ rotates around a horizontal axis [OS92] in response to wind because of the magnus effect, generating electrical energy via a generator connected to its horizontal axis. The energy produced is then transmitted to the ground by a conductive cable. Magenn Inc. tested a $2kW$ prototype in 2008, and in 2010 has started manufacturing and commercializing a $100KW$ balloon.

Figure I.10: The balloon of Magenn Power Inc.

The second solution adapted by Sky WindPower [Skya], Joby energy [JE], and Makani Power [mak] is to use airborne wind turbines to harness energy directly in high altitude winds and send it to the ground through conductive cables. Fig.I.11 shows the airborne wind turbines proposed by Joby energy. This solution has some technical complexities, high cost and heavy structures. Only Makani Inc., acquired by Google.org as part of GoogleX, has passed to the production phase. They have already started producing a $1MW$ airborne wind turbine named "Makani M1".

Figure I.11: Airborne wind turbines Imagined by Joby energy

The third option is to use power kites as renewable energy generators such as the "Kite Wind Generator" of Politecnico di Torino, and the "Laddermill" of the Delft University of Technology shown in Fig.I.12. In this case, mechanical power is generated when the kites are pulled by wind, transformed then into an electrical one using an on-ground generator. This allows the flying part of the system to be much lighter and avoid using conducting cables. This technology is expected to produce huge amounts of power using a much simpler and safer structure.

Figure I.12: Imagined laddermill of Delft University of Technology

I.3.a-iii Comparison between Different Technologies

After introducing the different proposed solutions to capture wind energy, in the following, the advantages and disadvantages of each solution are discussed. They are classified in three categories: Conventional wind turbines, airborne wind turbines and kite-based systems.

From the grid connection point of view, wind turbines are not able to produce their rated power continuously, due to wind irregularity at their working altitudes, a problem that is less significant in the case of HAWE systems which are supposed to be working at an altitude higher than $400m$ where the winds are more regular.

Concerning the quality of generated power, it depends whether the system returns power to the energy source or not, meaning whether it has a recovery phase or not. In general, a classic turbine has only one phase of functioning that is generation, which means that while generating, the resulted power is continuous as long as the turbine is in the power region limited by its cut-in speed and cut-out-speed. This is the case of stationary air rotor systems also. Meanwhile, kite-based systems and airborne wind turbines have a recovery phase whose goal is to maximize the average generated power and the respect of the systems constraints, but reflects negatively on the generated power which becomes intermittent. This, however, may be balanced out by the high reversibility of these systems that allows using two or more system with a suitable choice of the kite's orbits to filter the resulted generated power.

Furthermore, HAWE systems offer mobility and can be invested hugely as it works at a high altitude where strong wind could be present with little or no wind at low altitudes. Besides, they offer a very high adaptivity, as their rated power, as well as, generation/consumption phases, can be modified by changing the orbit the kite is following e.g. size, rotation

and/or inclination, or changing the altitude. Notably, a kite-based system rated power can also be adjusted by changing the kite surface. These adjustments are important to optimize the system's generated power for changing conditions and constraints on it, e.g. Wind speed and direction.

Cost-wise, HAWE systems economize the manufacturing, transportation and construction cost compared to a wind turbine, e.g. they eliminate the turbine mast cost.

Finally, a kite-based System backs down when it comes to the real-time control issue. That is due to the complexity of the system's behavior, a matter that will not be a problem thanks to the rapid development in computer and information technology, allowing to have fast and reliable real-time data processing.

We are interested in HAWE relaxation-cycle systems, and particularly in kite-based system due to the advantages that can be obtained using it. This is the focus of the next section.

I.3.b Flexible Power Kites

Kites were used in China approximately 2,800 years ago. Apart from being child-toys, their early uses involved measuring distances, testing the wind, lifting men, signaling, and communication for military operations. After spreading in Asia, kites were brought to Europe by Marco Polo at the end of the 13th century [Gom]. In the 18th and 19th centuries, in addition to military operations, kites were used to tow buggies in races against horse carriages in the country side [Gri09], and researchers like Alexander Graham Bell and the Wright Brothers invested kites in their development of the airplane, such as the Wright's Glider 1900 shown in Fig.I.13. At the beginning of the 20th century, interest in kites was diminished by the invention of airplane [Sch12]. Kites drew back attention in 1972 when Peter Powell introduced a steerable dual lines kite, and flying kites became a sport. Afterwards, in 1979, M.Loyd wrote a paper [Loy80] on how to use an airplane connected by a tether to generate huge amounts of energy. Though his paper was completely ignored at the time, it is now considered a revolutionary idea that will compute hugely in the future of renewable energy.

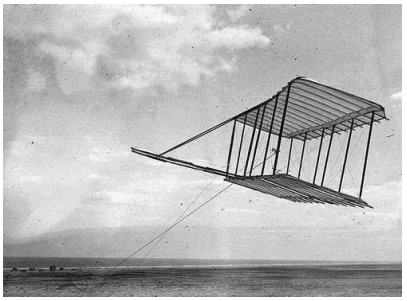

Figure I.13: Wright brothers Glider 1900.

It is not until 1996, however, that the idea was proposed again when W.J. Ockels registered his Laddermill patent [Ock96] proposing the usage of kites connected in a cycle to turn an electric machine and generate electricity. Fig.I.14 shows the proposed Laddermill

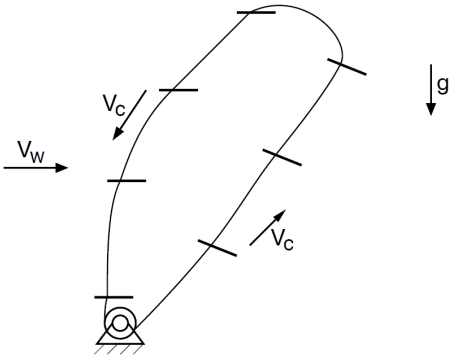

Figure I.14: The Laddermill concept proposed by W.J. Ockels [MOS99].

structure of Ockels's patent. Since then, few groups around the world have been working on this concept including Ockels team in T.U.Delft, Netherlands. For example, an Italian project named "Kitegen" was launched in 2007 in the Politecnico di Torino. A prototype was built and tested, but the project has unfortunately slowed down recently due to lack of investment and the division into two companies: KiteGen and EnerKite.

Other university groups are carrying out these research, like for instance: K.U.Leuven in Belgium [FHGD11], the university of Heidelberg in Germany [DBS05] [HD07], the university of Oulu in Finland [AS13]; and the university of Grenoble in France [AHB11a] [AHB11b] [LJADH12].

In the industry sector, using flexible kites for towing ships is already in the market by Skysails GmbH Company in Hamburg, Germany [Skyb]. In fact, installing kites on huge ships proved to reduce their fuel consumption up to 30%, and now the company is studying the possibility of installing floating kite-based system in the sea to extract energy from off-shore strong winds. Some other companies' names in the field include: Makani Power Company in the USA [mak], Windlift [Win], SwissKitePower [Swi], and Worcester Polytechnic Institute (WPI) project #DJO-0408 [Bal08]. Fig.I.15 lists some of the main projects in kite power field.
New fabrication technologies permitted providing strong and light tethered kites, as well as, the huge development in electronics, communication, and computer sciences allows a fast and robust real-time optimization and control.

I.3.b-i Crosswind Kite Power

In his paper [Loy80], Loyd analyzed three ways by which the kite can generate energy. Two are significantly more effective:

- The The drag power that can be exploited by having air turbines on the kite. This idea was employed in the Air Rotor system and the airborne wind turbines presented in section.I.3.a-ii.

- The crosswind power. Loyd showed that by neglecting the kite's weight and the tether effect, and considering the kite motion to be directly in crosswind[5]; then the

[5]This means the tether is parallel to the wind.

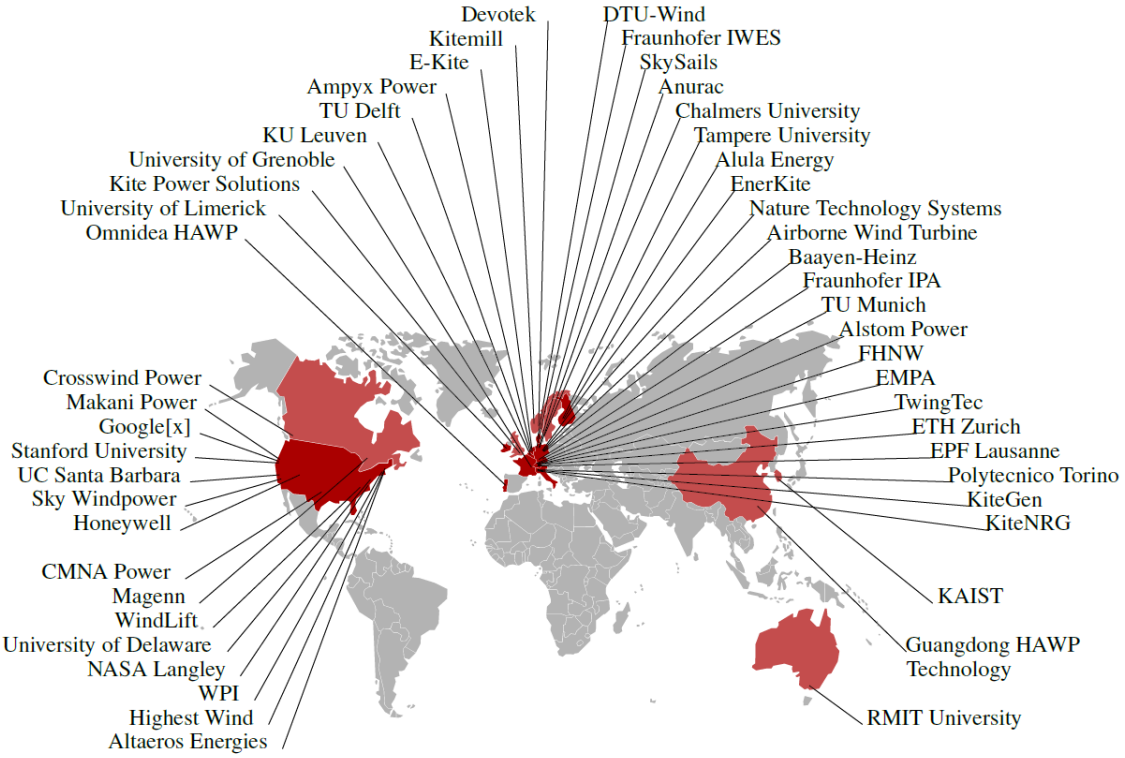

Figure I.15: Airborne wind energy research and development activities by country and by group as shown in the Airborne Wind Energy book [ADS13].

kite's speed is increased significantly above the wind speed, which leads to increasing the can-be-generated power.

It is, however, not possible to let the kite fly always in a crosswind direction. In [ARS09], the refined crosswind motion low is found and expressed in eq.I.3. In the case of a small kite and a constant tether length, the refined crosswind formula is:

$$\begin{aligned} \vec{W}_e^p &= \vec{W}_e - (\vec{e}_r.\vec{W}_e).\vec{e}_r, \\ |W_e^p| &= G_e V_{||} \end{aligned} \tag{I.3}$$

where $\vec{W}_e$ is the effective wind speed, that is the difference between the wind velocity $\vec{W}$ and the kite's velocity $\vec{V}_k$, $(\vec{e}_r.\vec{W}_e).\vec{e}_r$ is its projection on the tether direction, $V_{||}$ is the crosswind speed and G_e is the aerodynamic efficiency.

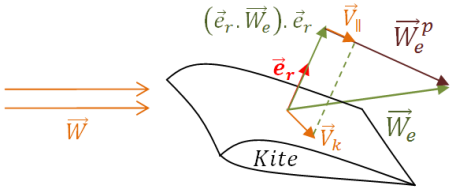

Figure I.16: Refined crosswind law.

An eight-shaped trajectory of the kite is highly adapted, since it maximizes the apparent

wind blowing against the kite, and ensures the non-tangling of its tethers. But it should be mentioned that, according to [HD06], a circular trajectory will provide a 0.9% to 1.3% higher traction force than that of an eight-shaped one, in addition to ignoring the wind direction that may affect the system's safety and control complexity [AC09]. Still, tethers tangling and coiling remain a serious problem and render the eight-shaped trajectory preferable.

I.3.b-ii Energy Generation

The concept is to mechanically drive a ground-based electric generator using one or several tethered kites[6]. Energy is extracted from high altitudes by controlling the kite to fly with a high crosswind speed. This develops a large pulling force that turns the generator, thus generating electricity. However, due to limitation in the tether's length and the power region, the tether must be reeled in to its initial position, consuming energy as doing so. The system optimization will aim at maximizing the generated power and minimizing the consumption. The kite-based system should offer the tethered kite the flexibility to change its flying direction following the wind direction.

In general, kite-based systems are classified in three groups according to the energy generation concept:

The Pumping System[7]

It is largely adapted by several research teams. The system has two operation phases:

- Traction phase, in which the kite is pulled by the wind, unrolling the tether which turns the ground-based machine
- Recovery phase, that begins when the tether reaches its predefined maximum length or height, and needs to be reeled in, an operation that consumes energy.

To minimize this consumption the KiteGen project has presented two methods [FMP10]:

- Low power recovery maneuver: The kite is driven to the borders of the "power zone" defined later in Sec.II.2.a-i, where the aerodynamic forces become much weaker, and it can be recovered with low energy expense. One down point of this maneuver is that it occupies a huge space, which is a problem when it comes to considering a kite-farm for example.
- Wing glide maneuver: Here the kite is controlled to be parallel to the tether, thus it loses its aerodynamic lift and can return fast with low energy losses. Nonetheless, this maneuver, subject the system to instability and difficulty to restart its cycle.

Other than sequent eight-shaped orbits with increasing altitude that are usually adapted in the traction phase (see Fig.I.17) [AS10b], [LO05], [PO07a], [HD10], [CFM10], other ideas are also investigated. In GIPSA-Lab of Grenoble university, France, researchers are

[6] The generated mechanical power can be used directly to pump water or to tow a ship

[7] Referred to as the yo-yo mode of KiteGEN [CFM10], or the open-loop orbit of Argatov [AS10a].

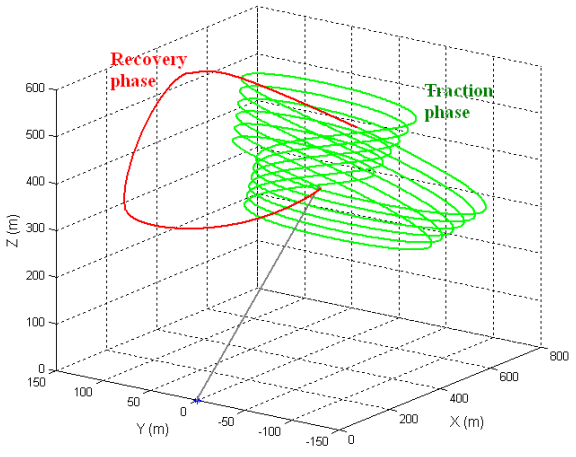

Figure I.17: An example of the pumping mode.

working on a pumping kite in which the kite's tether has a constant flight angle and the kite is controlled by its attack angle and traction force [LJADH12].

Apart from this, another idea started in SEQUOIA Company is the Rotokite. The idea proposes having two opposed kites connected to a single tether [Ver]. They are controlled to rotate around the tether, generating a lift force that will pull out the tether, and when the maximum height is reached, they are warped to minimize the aerodynamic lift and then pulled down.

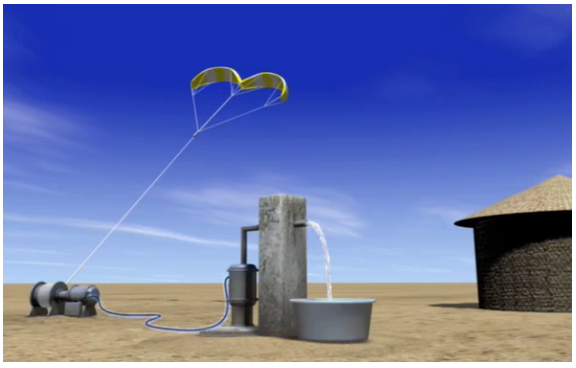

Figure I.18: An imagined Rotokite system used to pump water.

The Closed-Orbit System

In this system, the kite is kept on a single eight-shaped orbit. During one orbit, two regions can be distinguished: A high and a low crosswind region. In the high crosswind region, the kite pulls out the tether which forms the "traction phase", and in the low crosswind region, the tether is reeled in, and that is the "recovery phase".

This mode may not generate as much energy as the pumping mode [AS10a], but it is easier to be stabilized and controlled, as it needs only one controller compared to at least two controllers in the pumping mode, as well as it occupies a small space [LW06]. Moreover,

its production can be optimized by a careful choice of the orbit and adding the possibility to control the aerodynamic coefficients through control of the kite's attack angle [AS10a].

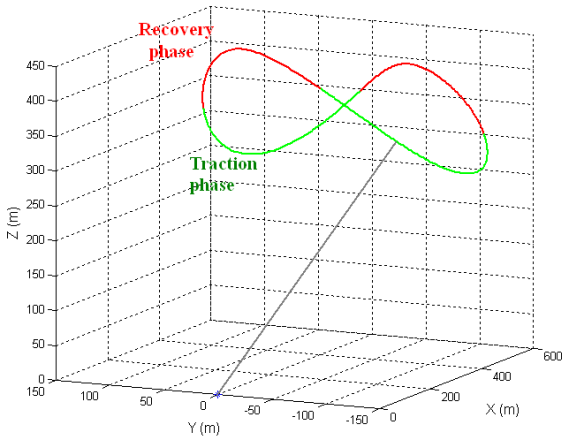

Figure I.19: Closed-orbit mode.

The closed-loop approach is principally used to tow boats and minivans [Bra10].

The Carousel System

This system, proposed by M.Ippolito [Ipp08], suggests placing several tethered-kites with their control units on vehicles moving along a circular rail path. Fig.I.20 shows a simplified presentation for the system.

Vehicles' speed is kept constant using electric machines on their wheels, while the kites tether's length might be fixed or have a rolling/unrolling motion [CFM10]. For the first case, when the kite is in its power zone, it pulls the vehicle which presents the traction phase, and when the kite is out of the power zone it is moved back into it by the vehicle and that is the recovery phase. According to [FMP11], this complex structure generates the same power that can be produced using a simple pumping kite.

Although by applying a rolling/unrolling (pumping) motion of the kite to compensate the consumed energy during the recovery phase, a highly efficient system can be obtained, it is still economically and technically very challenging. This proposed system is able to extract

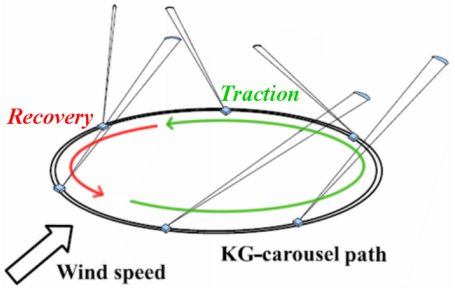

Figure I.20: Simplified presentation of the carousel of Kite-GEN

huge amounts of energy, but it does not satisfy that a kite-based system is supposed to be largely lighter and cheaper than a classic turbine.

I.3.c Kite-based System vs Classic Wind Turbine

An example to compare a kite-based system to a classic turbine from the generated power point of view, is given in [Fag09]: A $2MW$ wind turbine, the weight of the rotor and the tower is typically about 300 tons, while a pumping kite-based system of the same rated power is estimated to be obtained using a $500m^2$ airfoil and $1000m$ long tethers, with a total weight of about 2 tons only.

Practically, we mention here two examples of early trials in the field. In T.U.Delft, a one-tether kite control is tested in simulation; the kite surface is $25m^2$ with a mass of $50kg$ and the tether average length is $1000m$. An optimal control is used to command the roll angle, attack angle, and the tether length variations rate. It uses different random guesses because there is no guarantee that the obtained solution is a global one. The average power generated depends on the orbit period, for example, a 60 sec period orbit yields in 75 kW [WLO07b].

The KiteGEN team has chosen a two-tether kite for their prototype, with control of the tether length variations rate and the roll angle. For simulation, a kite of $10m^2$ and 4 kg of mass; and maximum $800m$ long tethers. A nonlinear predictive control, without a pre-computed trajectory, is applied. It maximizes the average generated power directly. Besides, a sampling time of 0.2 sec is obtained by applying a fast nonlinear model predictive control (NMPC), for the sake of real time control computations. With a wind-speed of about $7.7m/s$ at $300m$ altitude, the average generated power is 5 kW [Fag09].

Furthermore, the following comparison is proposed to compare the efficiency of a kite-based system adopted in the next chapters and named Kite Generator System (KGS) compared to a classic wind turbine.

Discussion A small Enercon wind turbine (E33) has the main characteristics of Table.I.2. Its rated power of $330kW$ can be obtained using the closed-orbit KGS described in Sec.IV.4.d but with a kite surface $A = 300m^2 = 30m \times 10m$. The flying part of such a system, including: the kite and the orientation mechanism will have a mass of less than $1t$ compared to about $18.7t$ for the E33 turbine's on-tower mass, eg: excluding the tower and the turbine foundation. This fact makes the KGS easier to be transferred and maintained. On the other hand, both wind system occupy theoretically the same ground area. But when it comes to aerial area, the KGS's power per unit area for this example seems to be about 60 times less than that of the E33, the same system can be used to produce more power by simply changing the kite's altitude. As well, working at high altitude ensures a constant high wind speed hence constant power generation.

Using a closed-orbit KGS is not suitable to compare the potential of using kites to produce electrical power to that of classical wind turbines, as its energy efficiency is small compared to the pumping KGS or a closed-orbit configuration with a variable aerodynamic efficiency G_e.

Table I.2: Enercon E33 main characteristics

Rated Power	300 kW
Hub height	50 m
Rotor diameter	33.4 m
Rated wind speed	11.7 m/s

I.4 Wave Energy

Oceans store a tremendous amount of energy and are close to many concentrated populations. This energy is stored in many forms. Most importantly in the form of flow, like tidal and marine currents, and waves and swells[8].

Wave power is receiving a particular attention lately due to its great potential, since waves are more constant and predictable than other types of renewable energy, as well as, their stored energy is very dense compared to that of wind and solar [BVJH09]. According to World Energy Council, wave energy technically available for extraction can satisfy 10% of the world electricity demand. In metropolitan France, this proportion is a little less, it is estimated to $40TWh$, that is 7.27% of the $550TWh$ consumed per year in France [LP08].

Figure I.21: Wave energy annual potential (kW/m) [Atl].

France is a pioneer in the wave energy field. Historically, in 1799, in Paris, Girard and his son filled the first known patent to use energy from ocean waves, and in 1910, Bochaux-Praceique built an oscillating water-colomn device to employ wave power to supply electricity to his house at Royan, in France.

Wind waves are caused by the wind blowing over the surface of the ocean. They range between small ripples with approximately $10Hz$ frequency, that disappear once the wind

[8]The only difference between waves and swells is the distance from the source that has generated them, either local wind for waves or non-local for swells . For this reason, the word wave is used here to describe both.

stops, and $3.3mHz$ swells which are gravity propagated from wind-generated waves. Wind waves are distinct from longer wavelength waves caused by storms, earthquakes, e.g. Tsunamis, and those result from the Sun and Moon gravity, e.g. Tides.

Since sea water density at the surface is about $1020kg.m^{-3}$ and that of air is $1.27kg.m^{-3}$, waves travel much slower than the wind that created them, and the energy they can provide is compacted about 800 times. In fact, a wave power available for exploitation, given per wave front length unit, reaches a few tens of kW/m. For instance, wave annual average power on the Atlantic coasts is between 15 and 80kW/m [Mul03] which explains the particular interest in wave energy in the western coast European countries.

Nevertheless, taking into account the difficulties facing wave energy development, including for example waves irregularity and weather conditions, a wave energy exploitation system will be a complex sophisticated one [CMF02].

I.4.a Wave Average Power

Sea level oscillations, just as wind, are stochastic space-time random phenomena. A sea wave can be approximated by a sine wave with both stochastic variable amplitude and period. Fig.I.22 presents the parameters of such a wave. Based on this wave definition,

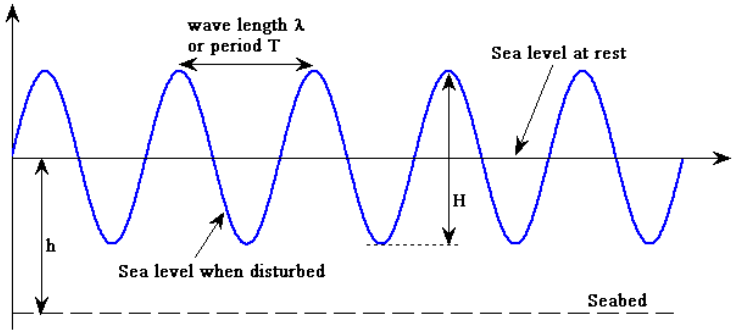

Figure I.22: Regular wave parameters.

one can find the wave front average power per meter [Fal07] in the case of deep water[9] (See Fig.I.23):

$$P_{dp} = \frac{\rho g^2}{16\pi} H^2 T \quad \text{(W/m)} \tag{I.4}$$

and in the case of shallow water:

$$P_{sh} = \frac{1}{\sqrt{(36\pi)}} \rho g^{3/2} H^2 h^{1/2} \quad \text{(W/m)} \tag{I.5}$$

where g is gravity acceleration, ρ is water density, H and T are the wave amplitude and period respectively, and h denotes the sea depth.

The previous wave definition considers a pure sinusoidal wave with no obstacles, while in fact, a wave is irregular and defined as a superposition of multiple waves with random

[9] Water depth exceeds a third of the wavelength.

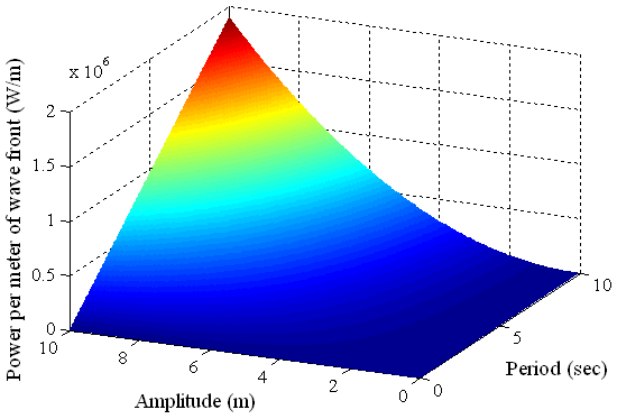

Figure I.23: Power per meter front for a regular wave.

amplitudes and periods, as explained later in section II.3.b-i. In [GHG10], sea behavior is defined as a group of sea states, where each state i has an average power given by:

$$P^i_{irr} = \int_0^\infty P^i(H,w)S^i(w)dw \quad \text{(W/m)} \tag{I.6}$$

where $S^i(w)$ is the power spectrum of the wave at the state i for the frequency w, and $P^i(H,w)$ is the average power of a regular wave with (H,w) as parameters.

The irregularity and the slowness of waves oscillations, make transforming their energy into an electrical form, that can be later commercialized, very challenging.

I.4.b Wave Energy Conversion Technologies

Several solutions are proposed to extract wave energy and convert it into electricity [Fal10] are proposed [AMCHB12] [BEBC07]. Wave energy conversion (WEC) systems can be categorized based on the location and the depth they are designed to work at, i.e. Near-shore and off-shore systems.

I.4.b-i Near-shore WEC Systems

They are mainly turbine-based structures; their operating principal is to employ waves oscillations to generate a current of water or air that turns a turbine coupled with an electric machine, thus generating electricity. As examples of these systems one can cite:

- WAVEGEN (4 MW)[10] In this system, an air turbine is turned by the air current generated by waves oscillations (Fig.I.24). It has been already installed and connected to the Spanish electric grid in 2009.
- TAPCHAN (Tapered Channel) Wave Energy (rated output about 350 kW) [Tju94]. Shown in Fig.I.25: This construction canalizes sea water to turn a turbine, then water flows from the basin back to the ocean by gravity. It was first constructed in 1985 and installed in Norway.

[10] http://www.unenergy.org

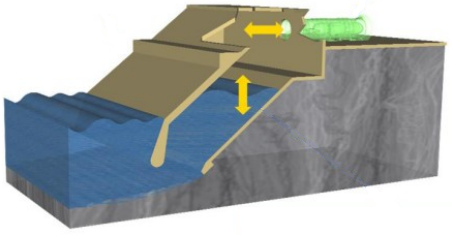

Figure I.24: WAVEGEN simplified structure [BWF02].

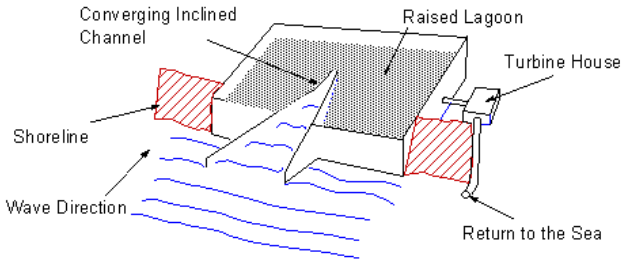

Figure I.25: TAPCHAN: Tapered Channel wave energy.

I.4.b-ii Off-shore WEC Systems

Here, floating systems emerged among others as the most important logic solution to capture waves. They capture waves oscillations and transform them into translational or rotational movements, that generate electricity via an electrical machine. Floating WECs are classified in three categories:

- ***Attenuators, or linear absorbers***: It is a large linear structure directed to be parallel to the wave propagation, and composed of jointed segments that rotates relative to each other harnessing the waves power as doing so. An example of attenuators is PELAMIS (up to 2.25 MW) [YHT00]. It is a series of semi-submerged cylindrical sections linked by hinged joints (Fig.I.26). The sections move relative to one another as waves pass. This motion is employed to generate electricity using hydraulic pumps. These systems are developed by a Scottish company (PELAMIS wave power), and was first connected to UK grid in 2004.

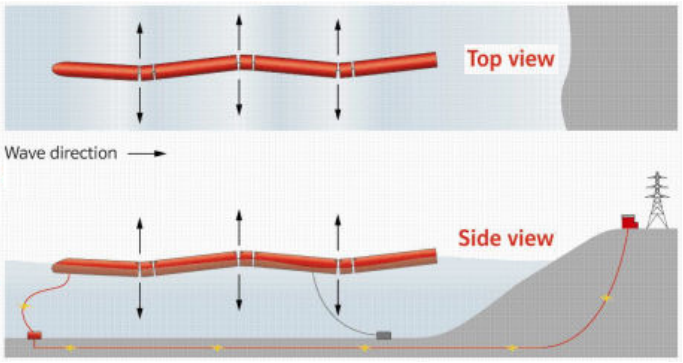

Figure I.26: PELAMIS wave energy system.

- ***Terminators***, It is a perpendicular-to-the-wave construction. An example of those is the Wave Dragon (7 MW), which is an overtopping terminator whose objective is to guide waves to form a vertical water current employed to turn a turbine. A 20 kW prototype was already tested in 2003 in Denmark [TKKFM06]. This project is now in its final stages to deploy a full-scale system connected it to the electric grid. Fig.I.27 shows its simplified structure.

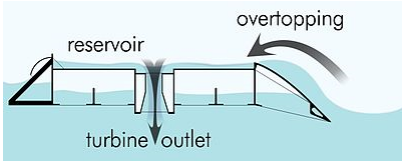

Figure I.27: Wave Dragon simplified structure [TPK09].

- ***Point Absorbers (PA)***: Contrary to former types, point-absorbers are small structures. They capture wave energy in all directions, and might be fully or partially submerged. Examples of PAs include:

  – SEAREV (Independent Electric Wave Energy Recovery System) (500 kW) [RBMJ10]: It is a project in France (Ecole centrale de Nantes). In this floating semi-submerged system a moving mass oscillates due to waves, and these oscillations are transformed into electrical power by means of hydraulic pumps or an electrical generator [AMBA09]. Fig.I.28 presents the basic principal of SEAREV.

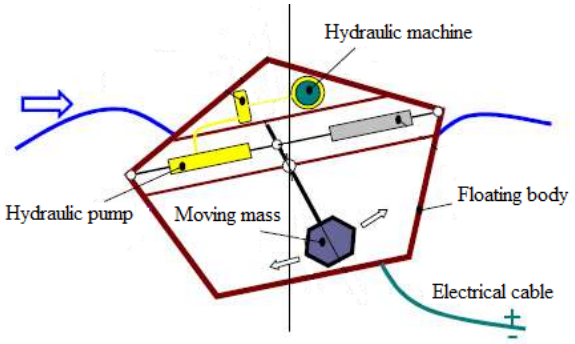

Figure I.28: SEAREV basic principal [CBG05].

  – CETO (5 MW)[Car] It is a pumping and desalination system. A small scale commercial demonstration project was constructed and tested in Garden Island in Western Australia. Fig.I.29 shows an imagined CETO farm.

I.4.b-iii Comparison between Different Technologies

Although near-shore WECs are easier to be installed and maintained, they are far from the powerful waves that lose most of their energy before reaching the coast, and they face public rejection as they damage the coastal rich underwater life and the scenery.

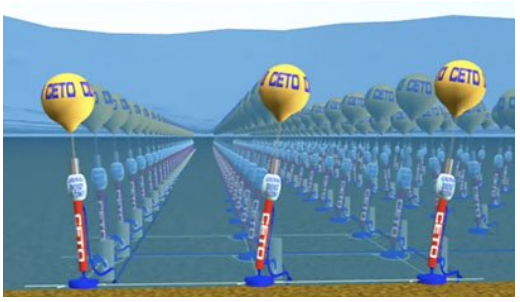

Figure I.29: Imagined CETO submerged farm[Car].

As will be explained later, in order to capture a maximum of the incident wave power, the floating body natural frequencies should contain that of the wave. Terminators and attenuators have a wide bandwidth which give them greater chance to harness most of the wave power, while the point-absorber which is a relatively small structure has a narrow bandwidth which applies that it should be controlled to enlarge it to contain the wave frequency. However, according to [BF75], smaller volume of the point-absorber increases the ratio potentially converted power to volume $\frac{P}{V}$.

One advantage of attenuators is their sensitivity to small amplitude wave oscillations.

As terminators employ turbines to harness wave energy, just like classic hydroelectric devices, they are easier to be modeled and controlled as the turbine-based technology is already well studied and researched. Still the means by which the terminator canalize water to traverse the turbine, makes the hydrodynamics very non-linear and not possible to be solved by the linear wave theory [Fal10].

Point-absorber systems are mostly designed so that their power transformation parts, mechanical, hydraulic or electrical, are enveloped and isolated from seawater, which yields longer lifespan and less maintenance.

I.4.c Vertically Oscillating Point Absorber Systems

A vertically oscillating point absorber system harness energy from the up and down waves motion. The device dimensions are small compared to the wave length. It is typically used to absorb energy from waves of 40 to 300m length. It can be partially or totally submerged. Fig.I.30 shows a point-absorber system anchored to sea bed.

An example of these systems is the Ocean Power Technology's Power-buoy. It is a floating buoy that has two rods attached to piston within a cylinder. As the vertical movement of the buoy causes these pistons to rise and fall as well, pumping ocean water through a turbine that generates electricity.

I.4.c-i Wave Energy Extraction

In order to capture the wave energy, basic energy conservation law apply that the point absorber should reduce the wave power. Hence, it should generate an opposing wave that interferes destructively with the original wave, which implies that in order to be a good point absorber, an object should be a good wave generator [Fal07].

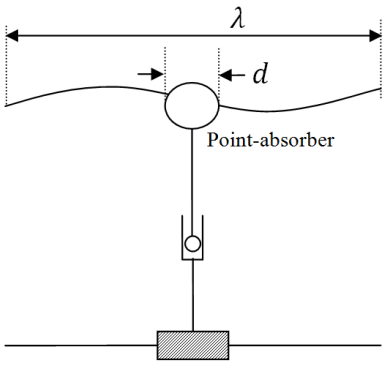

Figure I.30: A point-absorber system anchored to sea bed.

Nevertheless, there is always a maximum possible extracted power from the wave, because of the point absorber geometry. For example, in the case of a regular wave whose power E_w, a ring-shaped wave generator point absorber can absorb a maximum power of:

$$P_{max} = \frac{\lambda}{2\pi} E_w = \frac{\rho(g/\pi)^3}{128} H^2 T^3 \tag{I.7}$$

where λ is the wavelength.

I.4.c-ii Energy Generation Concept

A point-absorber energy generation concept depends whether its vertical displacement is controlled or not, and if it is, what the applied control method is. According to this we classify point-absorber systems in three categories[11].

Passive Point-Absorber

In the case of applying no control on the point-absorber, it exhibit slow oscillations following the wave and capture a part of its energy by means of its resistive inertia. The resulting performance is poor and depends on the geometry of the point-absorber.

In order for the point-absorber to generate an optimal destructive wave, its oscillations amplitude and phase should be optimized. A control is important to protect the system by respecting the functioning limits, such as the oscillations maximum amplitude.

Latched Point-Absorber

The point-absorber wave must be in phase with the original wave. This can be obtained by using a sufficiently large oscillating point-absorber whose bandwidth is wide enough to contain an approximate optimum phase for all frequencies within the wave spectrum, and, in the case of a reasonable-sized object, applying a control method to shift the bandwidth to contain the optimal phase.

This can be achieved by blocking the floating body for a suitable time interval, then let it

[11] Only the most common used techniques are chosen.

go when it arrives to the optimal phase position.

Reactive Point-Absorber

In a reactive point-absorber, both the phase and the amplitude of the oscillation are optimized, this requires returning some energy to the system.

I.5 Relaxation Cycle Systems

After addressing renewable energy history, importance and technologies to exploit it, this section is dedicated to a particular type of renewable energy systems, those of relaxation cycles. Some keywords that lead to the the definition of relaxation cycle systems are presented. Those are:

Nonlinear Systems

A nonlinear system is a system that does not satisfy the superposition property of linear ones:

$$f(\alpha x + \beta y) = \alpha f(x) + \beta f(y) \tag{I.8}$$

Which means that the effect of inputs is not additive neither changes in proportion to changes in the inputs. These systems are particularly important to physicians and engineers since most, if not all, physical systems are naturally nonlinear.

A dynamic nonlinear system is expressed by nonlinear differential equations that relate its outputs to its inputs. An example of nonlinear differential equations are the Navier-Stokes equations in fluid dynamics. The main significant difference between nonlinear and linear equations is that two solutions can not generally be combined to form a new one which is a result of the superposition property of eq.I.8.

A dynamic nonlinear system exhibits periodic oscillations when its differential equations have a nontrivial T-periodic solution:

$$x(t) = x(t+T) \quad \forall t \geqslant 0 \tag{I.9}$$

Limit Cycles

In the dynamic systems area of interest, a limit cycle is, as first introduced by Henri Poincaré in 1882 [KI98], an isolated closed trajectory in the phase space; in other words, its neighboring trajectories spiral either towards or away from it. In this context, limit cycles can only occur in nonlinear systems, since in a linear system exhibiting oscillations closed trajectories are neighbored by other closed trajectories.

That leads to the definition of a stable limit cycle, whose neighboring trajectories always spiral to it when time goes to infinity. Fig.I.32 illustrates this definition.

A system with a stable limit cycle can exhibit self-sustained oscillations, and the system goes always back to the limit cycle in the case of disturbance. Oscillations of this type are

called relaxation oscillations.

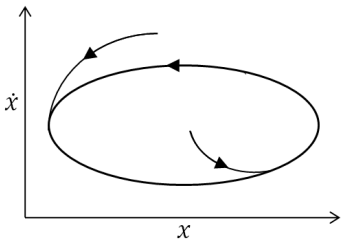

Figure I.31: A stable limit cycle

Relaxation Oscillations

They are nonlinear oscillations obtained by increasing a constraint continuously, then loosening it suddenly. When the constraint becomes very strong, the resistant part gives in abruptly and a part of the energy is evacuated. The constraint then re-increases and the cycle restarts.

To demonstrate, we consider few examples. A classical one is the Pythagorean cup experience, where the constraint is the water level which increases continuously thanks to the arriving water,then it drops sharply when the trap is triggered.

A second example is the Van-der-Pol oscillator expressed by eq.I.10.

$$\ddot{x} + \mu\dot{x}(x^2 - 1) + x = 0 \tag{I.10}$$

with $\mu >> 1$.

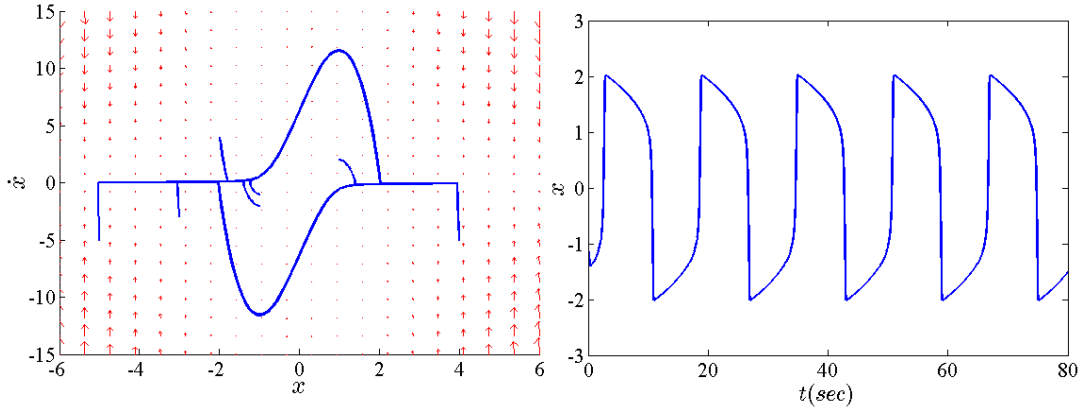

Figure I.32: The relaxation limit cycle solution of the Van-der-Pol equation with $\mu = 4$.

Many examples of such oscillations can be obtained by applying certain electronic configuration, as for instance, charging slowly a capacitor until it reaches a predefined value, then discharge it rapidly using a controlled switch.

Power Relaxation Cycle

Power relaxation cycle systems particularly concern power generation systems characterized by a cycle composed of two phases: a phase of slow recuperation of power followed by a fast phase of power release. The power release phase is needed to re-initiate the system state in order to start a production phase. Both phases are optimized and controlled to so that the cycle overall power is positive.

The power profile of a power relaxation cycle system can take the form shown in Fig.I.33.

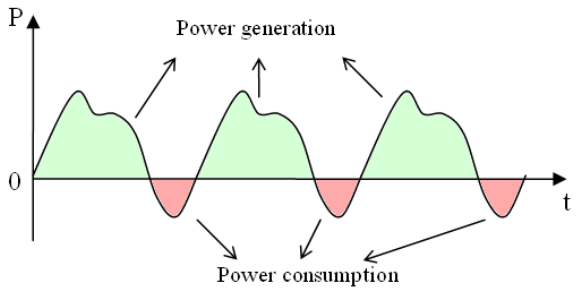

Figure I.33: Example of power profile of a limit-cycle system.

Examples of such systems include Kite-based traction systems, some wave power systems and renewable-based thermic systems. These systems pose a new scientific problem that is to control the generation/consumption limit cycle in order to maximize the generated power while respecting the various constraints on the system itself, the primary energy source, and the grid or the loads. Next, two examples of power relaxation cycle:

I.5.a Kite-based System's Relaxation Cycle

Depending on the kite-based system power generation concept and structure, the system can be a power generator all the time or a limit-cycle system that periodically generates/consumes power. An example of the former is the carousel configuration with variable tether length (see Sec.I.3.b-ii), and the dancing kites [KAB08] that involves connecting two kites to the same generator, and control them contrarily, in order to have a positive energy all the time (Fig.II.3-b).

Theoretically, when properly controlled, this type of systems does not present new challenges compared to classic renewable energy source (RES). Nevertheless, a simpler kite-based system has a periodic generation/consumption power profile.

This system uses a kite or an airborne wing to harness wind energy at high altitudes and transform its kinetic power into mechanical one by means of a tether coupled to a ground-based machine. The kite cannot pull infinitely as the tether length is limited, and should be periodically redrawn down to restart the pulling phase. Therefore, the kite or the wing control is designed to establish a relaxation cycle at the end of which, the system's flying part restores its initial position.

The relaxation cycle is chosen to be in the kite's power region, to respect the system's

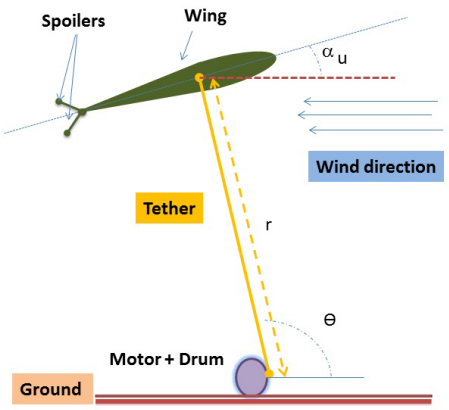

Figure I.34: The pumping wing [LJADH12].

physical limits (e.g. the maximum flight angle, the tether maximum traction and length; and the machine's maximum rotation velocity), and to maximize the average generated power.

The pumping wing of [LJADH12] serves as a simple example of such a performance. It is shown in Fig.I.34. The wing moves up and down while keeping a fixed inclination angle with the ground. While moving upwards the wing's attack angle is kept at a great value in order to produce a high lift force, and when moving downwards the angle of attack is reduced to a minimum value, so that the wing is almost parallel to the tether, and a small traction is needed to recover the wing's initial position.

I.5.b Heaving Point-Absorber's Relaxation Cycle

Another example of a relaxation-cycle renewable energy system is the vertical displacement wave energy one shown in Fig.I.35. It is composed of a floating part that has a single degree of freedom that is vertical displacement following z. This displacement is transformed into rotational movement using pulleys. The system displacement is controlled to maximize

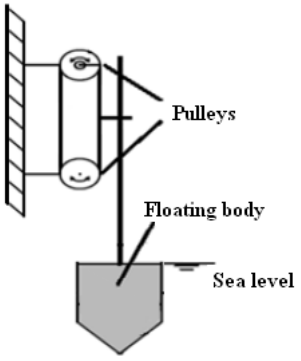

Figure I.35: A simplified vertical displacement wave energy system.

the harnessed wave energy by having a pattern chosen depending on the observed waves characteristics. That means, at some point the system consume a portion of energy to insure the optimal pattern. To clarify this point, let's consider the optimal phase control

proposed in [BDC04], [FJH09] and [Fal02]. It can be achieved by applying a latching control that blocks the floating body for a suitable time interval, then let it go when it arrives to the optimal phase position. Applying this latching create a relaxation cycle in the system.

I.6 Problem Statement and Objectives

Renewable energy systems with relaxation phases differ from those conventional systems in adding new challenges when considering their control and integration on the grid.

The system's cycle should be suitably chosen in order to maximize the average generated power, while keeping the system within its physical limits. This is a spacial-temporal optimization problem that needs to be solved.

Another criterion to optimize is to maximize the system performance; e.g. The ratio between the average power P_{av} and the maximum power P_{max}:

$$\mu = \frac{P_{av}}{P_{max}} \tag{I.11}$$

This avoids using over-sized system's components, as for instance electric machines, in order to obtain only a small portion of the power they are designed to pass.

In addition to the optimization problem, the systems dealt with are usually complex non-linear ones that require high level of modeling and advanced control techniques to stabilize and control them.

Another aspect to handle is the integration of relaxation-cycle systems on the electric grid. Those systems require a bidirectional interface with the electric grid, as well as, a storage unit in the case of a connection to a load or an isolated grid, which adds to the complexity of control and power management in the system. This may seem similar to wind turbine's with a storage to balance wind turbulence and an emergency stop mechanism, however, in the case of a relaxation cycle system, the system changes its status between generator and load periodically and relatively fast which requires the problem to be dealt with differently.

The above mentioned problems are discussed and solutions are proposed and tested throughout the rest of this thesis. Two systems are considered as case-studies: The kite generator system proposed in Section.I.5.a and the heaving point-absorber system of Section.I.5.b.

I.7 Conclusion

In brief, this chapter provided a mapping of current technologies proposed to exploit wind and wave energy, with a special attention to those employing relaxation-cycle systems.

A booming question is being asked a lot at present: What is today's energies' future?

Fossil fuels are not expected to answer the growing energy demand for a long time, and they are getting more and more expensive due to the technical difficulties accompanying exploiting newly explored fields. These reasons claim searching new solutions for energy production. Among proposed solutions, renewable energies offer a clean, safe and sustainable substitute to fossil fuels.

Here, renewable energy systems with relaxation cycles are considered. They are a newly explored class that emerged from the recent research in the field of high altitude wind energy, wave energy and thermal energy. They are characterized by a power cycle that has two phases: A generation and a recovery phase, and the difficulties arise when it comes to optimizing and controlling this cycle in order to maximize the generated average power, and when the system is used in an isolated grid.

Chapter II

Relaxation Cycle Systems: Structure and Modeling

Contents

Abstract

In the scope of relaxation-cycle systems and their contribution for electricity generation, the two examples presented in Chapter I are studied and modeled here. The kite-based wind system, named thereafter the kite generator system (KGS), and the floating point-absorber wave system named heaving point-absorber system (HPS) represent two emerged important classes of renewable energy systems whose early tests have shown promising open problems.

II.1 Introduction

The optimization and the control of relaxation cycles renewable energy resources require, as a first step, finding a model for the system in order to achieve better understanding of its behavior.

While the kite generator system (KGS) is chosen to be studied thoroughly in this thesis, an example of point-absorber wave systems, that is a heaving point-absorber system (HPS), is studied and modeled as well in order to show its similarity with the KGS and how it may be controlled in the same manner in order to maximize its cycle average generated power.

In this chapter, the structure of the proposed systems, as well as the model of each are developed. KGS found models will be used to design the control strategy and will be implemented on Matlab/Simulink in order to test this strategy (section III.3.a-iv). They are also used to emulate the system's behavior by a physical component, a torque controlled DC-machine, on the real-time experimental platform presented in Chapter.IV.5.

The chapter is divided into two main sections. The first part is devoted to the KGS. It starts with presenting the chosen structure and its main components. Next, it introduces the dynamics of the kite and how its traction is transferred to the ground to serve as a torque applied on an electric machine. The second part handles the HPS. It presents and models the system, and go over the techniques to maximize its average generated power.

II.2 Kite Generator System

As shown in Fig.II.1, a simplified kite-based system is composed of a kite connected to a drum by a tether. The drum changes the traction force generated by the kite into a resistant torque applied on an electric machine through a gearbox. The machine converts this mechanical traction to an electrical energy that can be later stored or injected in the electric grid.

In a closed-orbit scenario, energy is extracted from high altitudes by letting the kite fly on a closed lying-eight orbit with high crosswind speed [FMP09]. While tracking the orbit, two phases are distinguished: A traction phase, through which the KGS develops a large traction force that turns the electric machine, thus generating electricity, and a recovery phase, through which the kite is pulled by the machine, consuming energy as doing so. The objective is to improve the traction/recovery cycle through controlling the kite's position and movement around a predefined optimal trajectory that depends on wind's direction and speed.

This mode's efficiency is 16 times less than that of a pumping system presented in Sec.I.3.b-ii [AS10a]. But it can be improved 5 times by varying the aerodynamic efficiency [AS10a]. The closed orbit system is easier to be stabilized and controlled, as it only needs one controller, it also occupies a smaller space compared to an opened loop or a carousel configuration (sec.I.3.b-ii) [LW06].

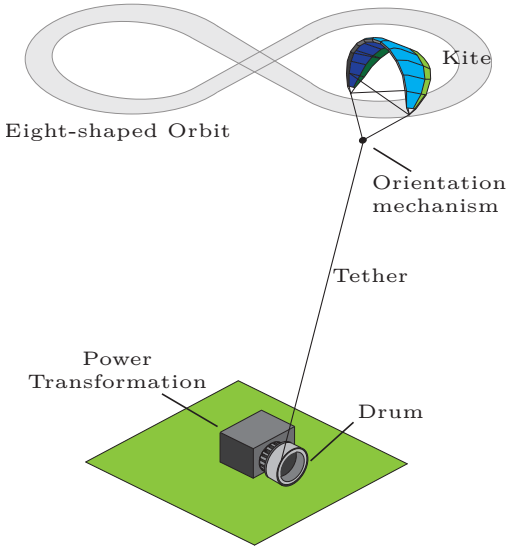

Figure II.1: Kite generator system structure.

II.2.a KGS Structure

Different research teams have adopted slightly modified structures from the basic one in Fig.II.1. They vary in the number of kites and tethers, the implemented orientation mechanism, as well as the used materials.

In the next paragraphs, each part of the KGS is presented in more details and different designs are overviewed.

II.2.a-i The Kite

In the KGS, the kite represents the effective wind power harnessing part of the system.

Kite's Parameters

Just like an airplane wing, a kite is characterized by two main parameters: its aspect ratio AR and its aerodynamic efficiency G_e. The aspect ratio is the ratio between the kite span w_s and chord c (see Fig.II.2-(a)), meanwhile, the kite efficiency is the ratio between its lift coefficient C_L and drag coefficient C_D. These coefficients are functions of the kite's attack angle α, that is the kite angle with the effective wind W_e (The difference between the wind speed and the kite's velocity.)

Kite's Forces

The forces acting on the kite can be summed up in (see Fig.II.2-(b)):

- $\vec{F}_{grav} = m\vec{g}$ the gravity force, where m is the kite mass and $\vec{g}$ is the gravity acceleration.
- $\vec{F}_{app}$ the apparent force which results from the kite's acceleration.

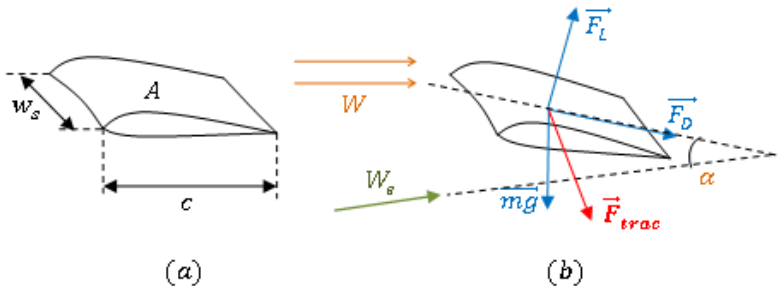

Figure II.2: Kite's main parameters and forces.

- $\vec{F}^{aer}$ the aerodynamic force which can be decomposed into: A lift force $\vec{F}_L$ that is perpendicular to the kite's surface A, and a drag force $\vec{F}_D$ which has the effective wind's direction $\vec{W}_e$. Eq.II.1 presents the amplitude of both forces, where ρ_a is air density.

$$F_L = \frac{1}{2}\rho_a A C_L \left|\vec{W}_e\right|^2, \quad F_D = \frac{1}{2}\rho_a A C_D \left|\vec{W}_e\right|^2 \tag{II.1}$$

- $\vec{F}_{trac}$ is the traction force of the tether.

Kite Choice

To maximize the system's generated instant power the traction force needs to be maximized, which means having a high aerodynamic force and a low weight. So in order to use a specific kite in a wind energy exploitation system, it should satisfy the following criteria: Most importantly, it should have a high aerodynamic efficiency, and secondly be light but still be strain, resistant; and easily maneuvered.

Being light and strain depends basically on the materials the kite is made up of. Meanwhile, a high aerodynamic efficiency and maneuverability, both depend on the kite design, but each has opposite requirements to the other [FMP10]. Hence, a kite designer should find a trade-off between these two.

Another important parameter is the kite surface. On one side, the kite's exploited power is a linear function of its surface [KAB08], and a bigger surface enables the kite to work at higher wind speed, and results in more stability. On the other side, the bigger the kite is, the more difficult it is to be oriented.

When first it was suggested, the Laddermill [Ock96] proposed using rigid wings as they are more efficient, but due to safety issues [Ock01], they were soon replaced with flexible light-weighted ones. Suggestions were made to improve flexible kites' efficiency by using multiple kites on the same tether (or set of tethers). Fig.II.3 shows two proposed structures; the first is to have a stack of kites, as in, for instance, the case of the Laddermill of Delft [LW06]. The second is to link two kites to the end of the same tether, which results in the reduction of the tether drag and the power needed in the recovery phase [HD06]. Both described structures will allow having the same traction force for a smaller space and less land requirements, but are more difficult to be modeled and controlled.

For early experiments, commercial kites were used, such as the Clark-y kite ($10m^2$) used

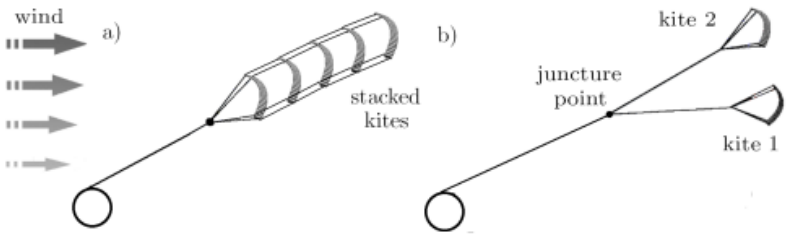

Figure II.3: Multiple-kite proposed structures [HD06].

in KiteGEN program [CFM07], the Peter Lynn Guerilla ($10m^2$) Kite used by Worcester Polytechnic Institute (WPI) team [KAB08], and the Peter Lynn Bomba ($8.5m^2$) surf-kite (shown in Fig.II.4) used by Delft team for their small-scale $2kW$ testing Laddermill [LRO05]. However, research has been going on to design and develop bigger and more specialized kites [Dun14].

Figure II.4: The peter Lynn Bomba kite.

II.2.a-ii Kite Orientation

While power generation is a direct result of pulling the tether out and turning the electrical machine, choosing a kite orbit is important to insure a maximum average power during the kite cycle, while respecting the structural limits of the system, as well as the limits on the controls and state values.

In order to operate, the kite must stay in its power zone, a zone where enough lift force is applied on it to keep it flying. The power zone is a half hemisphere, whose center is the point where the kite tether is parallel to wind direction. Fig.II.5 represents this power region.

Directing the kite to follow a certain optimal orbit is done through an orientation mechanism that controls the kite roll angle and/or attack angle, as well as the control of the tether traction.

The orientation mechanism may act on the kite tethers starting from the ground, and in this case there are usually 2 or 4 tethers; or it can be up close to the kite, as shown in Fig.II.1, and receiving the control signals from the ground station through wireless connection. In this case, the mechanism's weight is added to the kite's.

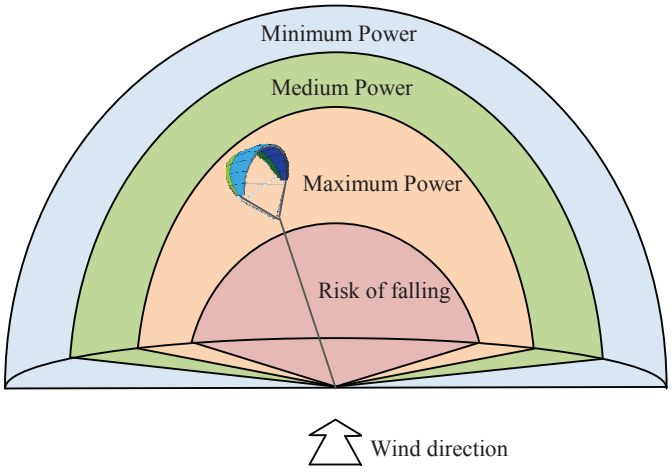

Figure II.5: The kite power region.

II.2.a-iii The Tethers

Tethers are needed to transmit the aerodynamic forces acting on the kite to the ground-based generator. Two aspects are important here, the number of tethers, and their design, including their diameter and composition.

The number varies usually between one and five tethers. The less the tethers, the more difficult it is to control the kite's orientation by earth-based controllers. On the contrary, according to [KAB08], using more than one-tether scenario decreases the system efficiency due to their weight and drag force. This has led Delf university team to adopt the one-tether configuration [Ock06] [FS12], but did not convince the KiteGEN and WPI team [Bal08]. Instead, they decided to use 2 and 4 tethers respectively, as this allows them to avoid using controllers installed on the kite, which will results in heavier kites, in addition to avoiding disturbances and failures associated with wireless communication between the controllers and the on-ground control unit.

Furthermore, tethers should be strong enough to bear high traction, but light and with a small diameter in order to neglect their weight and drag force $\vec{F_t}$. The KiteGen team used, for its small scale prototype, 1000m tethers made up of composite materials, Dyneema, that make it as light as similar steel tethers but 8 to 10 times more resistant [Fag09]. It is worth mentioning that Dyneema Company has been devoting an effort to developing tethers specially for the kite-based power systems.

II.2.b KGS Modeling

Many models for the kite and the tether were proposed. They vary in complexity and closeness to reality between the simple point mass model and the finite element implementation [WLRO08].

The point mass model is useful to estimate the possible generated power and is very light to be used in real-time control feedback loops [Die01][CFIM06]. A much more advanced model for the kite is the multi-body model shown in Fig.II.6. In addition to modeling

the distribution of the forces acting on the kite, the model takes into consideration the deformation of the kite resulted from these forces. This model, however, is quite computationally costly. A trade-off between the kite point mass model and the multi-body model is the rigid body model: It applies the already developed model equations for aircraft flight dynamics, with the addition of the tether's resulted forces and moments [GBS10]. The resulted model is simpler to be used in real time operation.

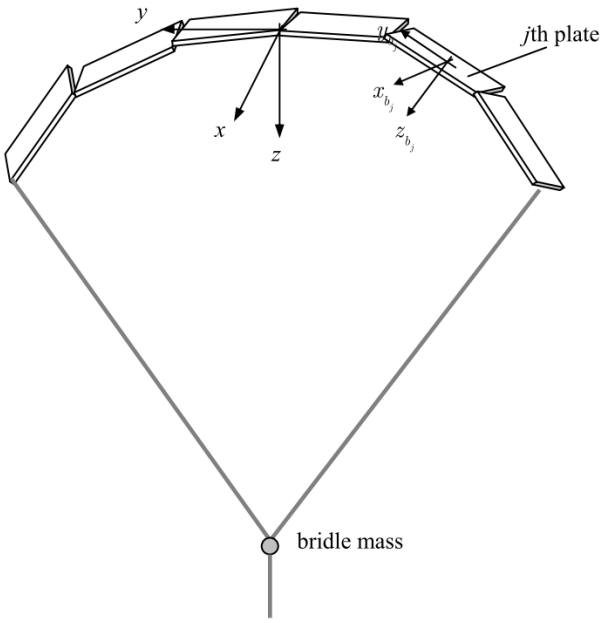

Figure II.6: Presentation of the kite's multi-body model [WLRO08].

For large scale kite-based systems, the tether model should be considered when controlling the system. A realistic model takes into account the tether weight and drag force and includes its elasticity [BO07][PO06].

In some studies [AHB11a][Die01][CFIM06], the tether's effect is totally neglected and the obtained model is useful as a base study to estimate the generated power. Rigid-body model for the tether is also used for feedback control and nominal trajectory design. In this model the tether is straight and rigid with a uniform mass and a distributed drag. More complex models discretize the tether into a series of point masses connected by hook joints [WLO07a][Bre11], and may add the effect of the tether elasticity by considering viscoelastic springs added to the hooks [WST08][Bre11]. The later model can be reduced to a simple spring-damper model [GBS10].

Usually two types of modeling are used, a simple model for the control feedback and a more close-to-reality complex one for simulations.

In this thesis, the following hypotheses are considered:

- A single-point model for the kite and the tether is adopted. Such a model is a rough one as it ignores the kite flexibility and deformations. It will, however, be used for control purpose and power estimation.

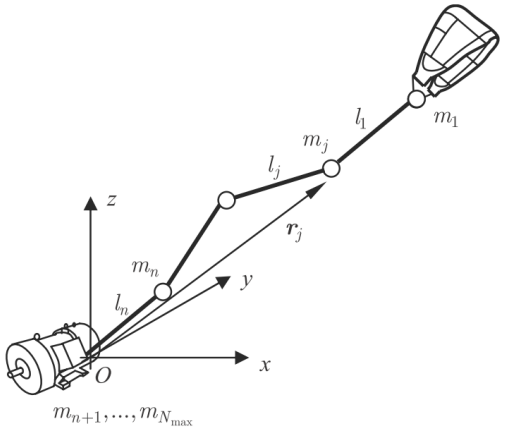

Figure II.7: Lumped mass tether model [WLO07a].

- The tether is inelastic and almost straight. This hypothesis is correct when the tether's length is less than $1000m$ and its inclination is less than 80 degrees [OG08].
- Wind is uniform with a non-varying direction, because wind speed at high altitudes is regular.
- The geometry of the tether allows neglecting its lift force, and considering only the drag C_{dt}.
- A high effective aerodynamic efficiency G_e of the kite and the tether. In this case, G_e is introduced in [HD06] by:

$$G_e = \frac{C_L}{C_D + \frac{A_c}{4A} C_{dt}} \tag{II.2}$$

  where A is the kite surface and A_c is the crosswind area of the tether.
- Kite's position and velocity as well as the traction force are known throughout the system's functioning using observers or sensors.

The previous assumptions cannot be applied if the goal is to study the control and the stability of the orientation system. Here, however, the main interest is to study the grid connection part and to estimate the power generated by such a system.

II.2.b-i Kite Dynamics

The kite dynamic model originally developed in [Die01] and used in [CFIM06] is adopted here. As illustrated in Fig.II.8, forces acting on the kite include the gravity force $\vec{F}_{grav}$, the aerodynamic force $\vec{F}^{aer}$ and the tether traction force $\vec{F}_{trac}$. The dynamics can be expressed in the spherical coordinates $\vec{e}_r, \vec{e}_\theta, \vec{e}_\phi$ as follows:

$$m\vec{\gamma} = \vec{F}_{grav} + \vec{F}^{aer} + \vec{F}_{trac} \tag{II.3}$$

where m is the kite mass, and $\vec{\gamma}$ is the kite acceleration expressed in eq.II.4.

$$\vec{\gamma} = \begin{bmatrix} r\ddot{\theta} + 2\dot{r}\dot{\theta} - r\dot{\phi}^2 \sin\theta\cos\theta \\ r\sin\theta\ddot{\phi} + 2\dot{\phi}(\dot{r}\sin\theta + r\dot{\theta}\cos\theta) \\ \ddot{r} - r(\dot{\theta}^2 + \dot{\phi}^2\sin^2\theta) \end{bmatrix} \tag{II.4}$$

The gravity force is expressed in eq.II.5.

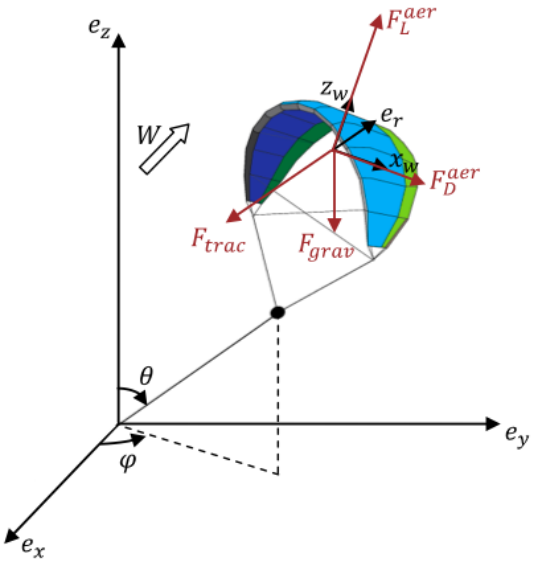

Figure II.8: Kite's main forces.

$$\vec{F}_{grav} = mg \begin{bmatrix} \sin\theta \\ 0 \\ -\cos\theta \end{bmatrix} \tag{II.5}$$

The aerodynamic force $\vec{F}_{aer}$ is related directly to the effective wind W_e, that is the difference between the wind speed and the Kite's velocity. Assuming the wind speed V_v is in the direction of x-axis, W_e is given by eq.II.6.

$$\vec{W}_e = \begin{bmatrix} W_{e\theta} \\ W_{e\phi} \\ W_{er} \end{bmatrix} = \begin{bmatrix} V_v \cos\theta\cos\phi - \dot{\theta}r \\ -V_v \sin\phi - \dot{\phi}r\sin\theta \\ V_v \sin\theta\cos\phi - \dot{r} \end{bmatrix} \tag{II.6}$$

The aerodynamic force has two components, a drag and a lift. In order to express both, a kite related coordinates $(\vec{x}_w, \vec{y}_w, \vec{z}_w)$ are defined as follows:

- $\vec{x}_w = -\frac{\vec{W}_e}{|W_e|}$ is carried on the longitudinal axis of the kite
- $\vec{y}_w$ is carried on the line connecting the kite's tips
- $\vec{z}_w = \vec{x}_w \times \vec{y}_w$ is perpendicular on the kite surface and directed upwards.

With these definitions, the drag and the lift components of $\vec{F}_{aer}$ are:

$$\begin{array}{rcl} \vec{F}_D^{aer} & = & -\frac{1}{2}\rho_a A C_D |W_e|^2 \vec{x}_w \\ \vec{F}_L^{aer} & = & -\frac{1}{2}\rho_a A C_L |W_e|^2 \vec{z}_w \end{array} \tag{II.7}$$

The kite related coordinates $(\vec{x}_w, \vec{y}_w, \vec{z}_w)$ are transferred to the spherical ones through

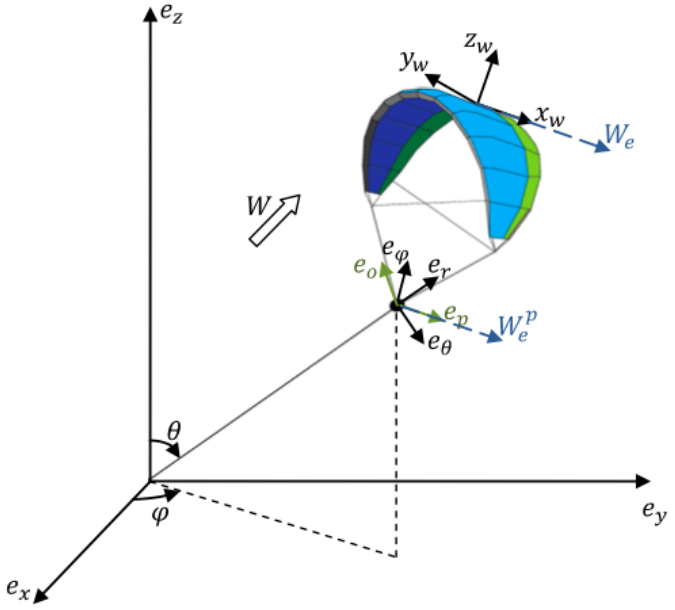

Figure II.9: Kite's attached coordinates.

the intermediate coordinates $(\vec{e}_r, \vec{e}_p, \vec{e}_o)$. $\vec{e}_p$ is the unit vector defined on $\vec{W}_e^p$, which is the projection of the effective wind on the plane specified by $\vec{e}_\theta, \vec{e}_\phi$:

$$\vec{e}_p = \frac{\vec{W}_e^p}{||\vec{W}_e^p||} = \frac{\vec{W}_e - (\vec{e}_r.\vec{W}_e).\vec{e}_r}{||\vec{W}_e^p||} = \begin{bmatrix} W_{e\theta} \\ W_{e\phi} \\ 0 \end{bmatrix} \tag{II.8}$$

while:

$$\vec{e}_o = \vec{e}_r \times \vec{e}_p = \begin{bmatrix} -W_{e\phi} \\ W_{e\theta} \\ 0 \end{bmatrix} \tag{II.9}$$

Taking into account eq.II.8 and the fact that the roll angle ψ, shown in Fig.II.10, is the control input, the kite-related coordinate $(\vec{y}_w)$ is written in the defined intermediate coordinates $(\vec{e}_r, \vec{e}_p, \vec{e}_o)$ as follows:

$$\vec{y}_w = \sin\psi.\vec{e}_r - \frac{W_{er}.\sin\psi}{||\vec{W}_e^p||}.\vec{e}_p + \sqrt{\sin^2\psi - \left(\frac{W_{er}.\cos\psi}{||\vec{W}_e^p||}\right)^2}.\vec{e}_o \tag{II.10}$$

Considering the notations: $L = ||\vec{W}_e^p|| = \sqrt{W_{e\theta}^2 + W_{e\phi}^2}$, $\eta = \arcsin\frac{W_{er}\tan\psi}{L}$, $vecy_w$ can be expressed as:

$$\vec{y}_w = \sin\psi.\vec{e}_r - \sin\eta\cos\psi.\vec{e}_p + \cos\eta\cos\psi.\vec{e}_o \tag{II.11}$$

Now that the kite-related coordinates $(\vec{x}_w, \vec{y}_w, \vec{z}_w)$ are expressed in $(\vec{e}_r, \vec{e}_\theta, \vec{e}_\phi)$, the drag and lift can be written in eq.II.12 and eq.II.13,

$$\vec{F}_D^{aer} = \frac{1}{2}\rho_a A C_D |W_e| \vec{W}_e \tag{II.12}$$

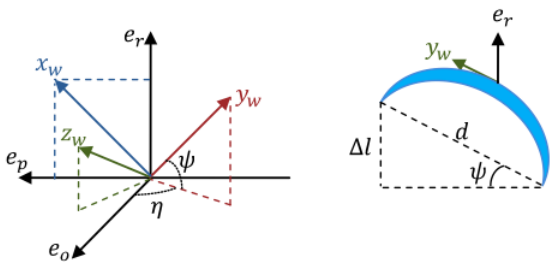

Figure II.10: Definition of ψ and η angles.

$$\vec{F}_L^{aer} = \frac{1}{2}\rho_a A C_L |W_e| \sin\psi \begin{bmatrix} W_{e\phi} \\ -W_{e\theta} \\ 0 \end{bmatrix} + \frac{1}{2}\rho_a A C_L |W_e| \cos\psi \begin{bmatrix} \frac{W_{er}}{L}[W_{e\phi}\sin\eta - W_{e\theta}\cos\eta] \\ \frac{-W_{er}}{L}[W_{e\theta}\sin\eta + W_{e\phi}\cos\eta] \\ L\cos\eta \end{bmatrix} \tag{II.13}$$

With $\vec{F}_{trac} = f_{trac}\vec{e}_r$ and by developing eq.II.3, the resulted system dynamics can be written as follows:

$$\begin{aligned} \ddot{\theta} &= f_1(\theta, \phi, r, \dot{\theta}, \dot{\phi}, \dot{r}, \psi) \\ \ddot{\phi} &= f_2(\theta, \phi, r, \dot{\theta}, \dot{\phi}, \dot{r}, \psi) \\ \ddot{r} &= f_3(\theta, \phi, r, \dot{\theta}, \dot{\phi}, \dot{r}, \psi, f_{trac}) \end{aligned} \tag{II.14}$$

The coefficients C_L, C_D are functions of the attack angle α. So the later can be controlled to have a constant coefficients or to increase the system's efficiency.

II.2.b-ii Machine Applied Traction

The tether traction in the kite $\vec{F}_{trac}$ is reduced when transferred to the ground machine. This is due to the tether's weight $\vec{F}^t_{grav}$ and aerodynamic force $\vec{F}^t_{aer}$. The forces balance in the kite gives:

$$F_{trac} = mr(\dot{\theta}^2 + \dot{\phi}^2 \sin^2\theta) - mg\cos\theta + \frac{1}{2}\rho_a A |W_e| \left(C_D W_{er} + C_L L \cos\psi \cos\eta\right) \tag{II.15}$$

The forces acting on a segment dl of the tether are the gravity force and the aerodynamic force. Their projections on the tether direction $\vec{e}_r$ are expressed in eq.II.16.

$$\begin{aligned} dF^t_{grav} &= \mu g \cos\theta dl \\ dF^t_{aer} &= \tfrac{1}{2}\rho_a d C_{dt} (V_{||} - V_L)^2 dl \end{aligned} \tag{II.16}$$

where μ is the mass per length unit.

Applying Newton second law on dr gives:

$$dF^t_{trac} = -\mu dr r(\dot{\theta}^2 + \dot{\phi}^2 \sin^2\theta) + \mu g \cos\theta dr - \frac{1}{2}\rho_a d_t C_{||} (V_{||} - V_L)^2 dr \tag{II.17}$$

By integrating II.17 between 0 and r, the reduction in the tether traction F_{trac} is calculated;

$$\Delta F^t_{trac} = -\frac{1}{2}\mu r^2(\dot{\theta}^2 + \dot{\phi}^2 \sin^2\theta) + \mu r g \cos\theta - \frac{1}{2}\rho_a d_t r C_{||} W_{er}^2 \tag{II.18}$$

hence the traction applied on the on-ground machine is the kite traction of eq.II.15 decreased by ΔF_{trac}.

$$\begin{aligned} F^M_{trac} &= \left(mr - \tfrac{1}{2}\mu r^2\right)(\dot{\theta}^2 + \dot{\phi}^2 \sin^2\theta) - (m + \mu r) g \cos\theta \\ &+ \tfrac{1}{2}\rho_a A |W_e| \left[\left(C_D + \tfrac{A_c}{A}\tfrac{W_{er}}{|W_e|} C_{||}\right) W_{er} + C_L L \cos\psi \cos\eta\right] \end{aligned} \tag{II.19}$$

Finally, the system average mechanical energy over one period T is the product of the traction force applied on the machine and tether length variation rate: the radial velocity V_L.

$$\bar{P}_M = \frac{1}{T}\int_0^T F_{trac}^M(t)V_L(t)dt \tag{II.20}$$

As noticed in the average KGS power equation II.20 and the traction force equation II.19, the power $\bar{P}_M$ can be written as a function to the radial velocity V_L, hence, in order to maximize $\bar{P}_M$, the optimal radial velocity profile should be found.

II.2.c Wind Speed Estimation

When it comes to an HAWE system, it is necessary to estimate the wind speed because of its importance in the optimization and control of the system. This can be measured by having on-board observers, or, since the wind is supposed to be stable at high altitudes, it can be estimated using a wind speed model.

Many models are listed in [AJ05], but two are mainly used in the literature [Hus02]. They are expressed in eq.II.21 and eq.II.22.

$$V(z) = v_0(\frac{z}{z_0})^\gamma \tag{II.21}$$

$$V(z) = v_0\frac{ln(\frac{z}{z_r})}{ln(\frac{z_0}{z_r})} \tag{II.22}$$

$V(z)$ is the wind speed at a certain altitude z, v_0 is the measured wind speed at an altitude z_0, and γ is a friction coefficient that characterizes the surface above which the measurement is done, and can be also described by the roughness factor z_r.

Using such models, however, is followed by an extremum seeking phase to improve the wind velocity estimation.

II.3 Heaving Point-Absorber System

Among the proposed solutions to extract offshore wave energy is the heaving point-absorber. It captures the up-down wave oscillations and transforms them into a translation movement employed later to generate electricity. In order to harness a maximum of wave energy, the point-absorber oscillations must be controlled to synchronize with the incident wave. This control creates consumption phases that needs to be minimized in order to maximize the overall generated power.

The power transformation unit usually rest on seabed, meaning that the captured oscillations should travel a long distance between the floating part and the power transformation unit. A solution to overcome this difficulty is the IPS-OWEC Buoy: A multi-body structure invented by Noren in 1981 and developed by the Swedish company Interproject Service (IPS).

In the following paragraphs, the structure and the modeling of a HPS system are considered. The goal of this section is to show the similarity between the HPS and the detailed earlier KGS from a power cycle and a control point of view.

II.3.a HPS Structure

A simplified structure of the proposed heaving point-absorber system is shown in Fig.V.1. It consists of a floating object, a buoy, connected rigidly with a tube that transfers its oscillations down to a power transformation unit. A linear gearbox changes the translation of the tube into a rotation motion captured by a synchronous machine. A control of the machine's rotation velocity insures average power maximization.

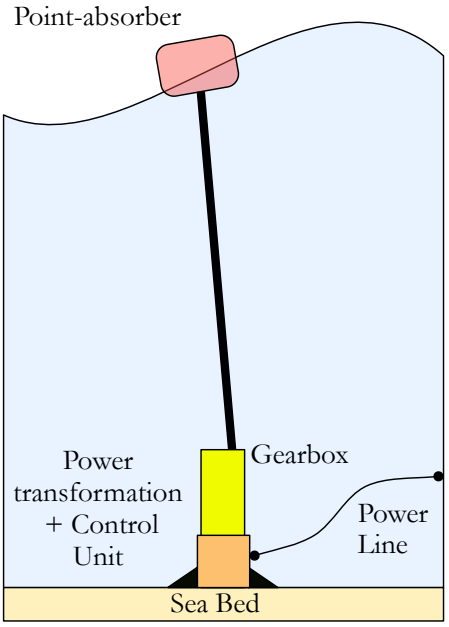

Figure II.11: The HPS simplified structure.

In order to extract a wave's energy, the PA should generate an opposite wave that interact destructively with the incident one. For this purpose, the PA oscillations and the incident wave must be in phase, and have the same amplitude.

According to [McC74], an optimal phase is obtained if the PA frequency spectrum contains the incident wave frequency, hence there is a resonance between the PA and the incident wave. As a conclusion, a bigger PA has a wider frequency spectrum, hence, it will make a better wave generator. Otherwise, the PA should be controlled to expand its spectrum beyond the wave frequencies. The oscillations amplitude can be controlled by modifying a load added to the PA.

However, the power that can be absorbed by the point-absorber is limited by two bounds: The optimum destructive interference power defined earlier by eq.I.7:

$$P_A = \frac{\lambda}{2\pi} E_w = \frac{\rho (g/\pi)^3}{128} H^2 T^3$$

and the Budal's upper limit [Fal07] for point-absorber in open sea:

$$P_B = \frac{\pi \rho g}{4} \frac{V H}{T} \tag{II.23}$$

where V is the heaving buoy submerged volume. These bounds define a region of the can-be-extracted wave energy, it is shown in Fig.II.12. As can be noticed from eq.II.23,

in order to increase Budal limit, the point-absorber dimensions should be bigger. On the other hand, they must be much smaller than the incident wavelength in order to neglect the reflection and the refraction phenomena that will be explained in the next section.

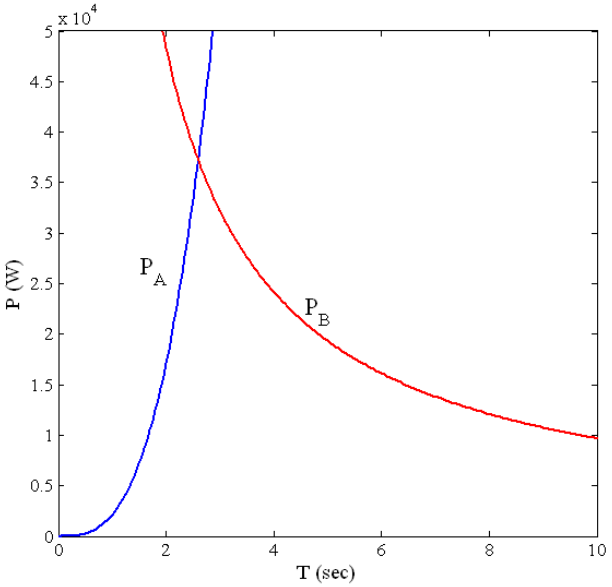

Figure II.12: The upper bound of the possible absorbed energy from a sinusoidal wave.

II.3.b HPS Modeling

When considering a body floating in a fluid, waves experience the following phenomena:

- Interference: is the superposition of waves traveling in the same fluid. It can be constructive or destructive.
- Reflection: It happens when waves bounce back from an obstacle.
- Refraction: It is the deflection of a wave when it passes between two environments.
- Diffraction: It considers the obstacle itself as a source of waves during the propagation of the incident wave.
- Radiation: It is creating waves in the fluid due to the floating body motion.

The interference is not taken into account as it does not affect the movement of the body. The reflection and the refraction phenomena are negligible if the floating body dimensions are small compared to the incident wavelength. The remaining phenomena, the radiation and the diffraction, are the ones allowing the PA to absorb the incident wave energy.

II.3.b-i Hydrodynamics Study

As a first step into modeling the HPS, a general case of a floating body with six degrees of freedom is considered (Fig.II.13). It is then simplified to obtain the model in the case of a system with only one degree of freedom.

In the fluid mechanics, Navier-Stokes equations (II.24,II.25) are employed to find the average extracted power from waves [Bel90].

$$\frac{\partial(\rho)}{\partial t} + \bigtriangledown(\rho V) = 0 \tag{II.24}$$

$$\rho\frac{dV}{dt} = -\bigtriangledown P + \mu \bigtriangledown^2 V + \rho B \tag{II.25}$$

where ρ is water's density, P is the pressure, B is the fluid external acceleration, μ is the fluid viscosity coefficient, and V is the fluid velocity field. Eq.II.24 represents the fluid continuity, and eq.II.25 is the momentum balance equation. Noticeably, these equations are nonlinear, as they contain the total derivative of the fluid velocity field V.

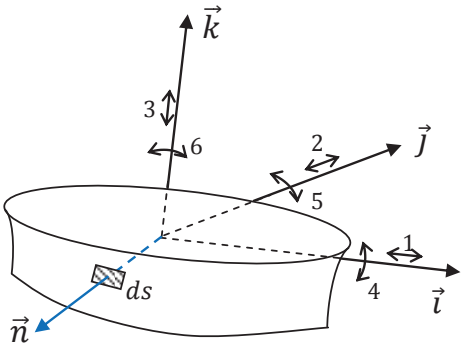

Figure II.13: Cartesian coordinates linked to a floating body with 6 degrees of freedom.

For the sake of simplicity, the following hypotheses are considered:

- Incompressible fluid: the fluid density is constant, thus the fluid mass is conserved.
- Irrotational flow $\bigtriangledown_x V = 0$: This allows to write V as a scalar potential $\bigtriangledown\phi = V$.
- Non viscous fluid: Which allows to neglect the forces related to fluid viscosity ($\mu = 0$).
- $\frac{H}{h} << 1$: In this case, the nonlinear terms of the total derivative are negligible.
- Sinusoidal-nature waves: the wave (A) is written as the multiplication of two terms: a function of position, and another of time.

  $$A = a(x, y, z)e^{jwt} \tag{II.26}$$

  where $a(x, y, z)$ describes the position in a Cartesian coordinate (Fig.II.13), and $w = \frac{1}{2\pi T}$ is the wave pulsation.

By considering these simplifying hypotheses, eqs.II.24, II.25, are written as follows:

$$\bigtriangledown^2(\phi) = 0 \tag{II.27}$$

$$P = \rho(\frac{\partial V}{\partial t} + gz) \tag{II.28}$$

The potential ϕ that satisfies eqs.II.27,II.28 needs to be found in order to calculate the forces and the moments acting on the floating part of the system, thus to find the extracted

power. For a sinusoidal-nature wave the diffraction and the radiation phenomena are decoupled, and the total potential ϕ can be written as a superposition of each phenomenon's potential added to the wave proper potential ϕ_I:

$$\phi = \phi_I + \phi_D + \phi_R \tag{II.29}$$

Where ϕ_D is the diffraction scalar potential and ϕ_R is the radiation scalar potential.

In addition to the continuity equation (eq.II.27), the potentials have to satisfy boundary conditions. Once found, ϕ is used to calculate the pressure in eq.II.28, thus the forces F_{ex} and the moments M acting on the system as in eq.II.30.

$$\begin{array}{rcl} F_{ex} & = & \iint_S \vec{n}\, P ds \\ M & = & \iint_S (\vec{r} \times \vec{n}) P ds \end{array} \tag{II.30}$$

where $\vec{n}$ is the unit normal vector on the floating body surface, S is the body's surface; and $\vec{r}$ is the unit rotational vectors around (x, y, z)(see Fig.II.13).

In the search of a solution for eq.II.27 and eq.II.30 in the case of one degree of freedom, that is a translation z, two cases are distinguished: Regular and irregular waves.

Regular Waves

As mentioned earlier, a regular wave is purely sinusoidal with a specific amplitude H and period T. In this case, from eq.II.30, the hydrodynamic excitation force is:

$$F_{ex} = (m + m_r)\ddot{z}(t) + R_r\dot{z}(t) + Cz(t) \tag{II.31}$$

where m is the floating body mass, m_r is the added mass, R_r is the radiation damping coefficient; and $C = \rho * g * S$ with S being the sectional surface.

Eq.II.31 can be represented using an electrical approach, in which $(m + m_r)$ is an inductance, R_r is a resistor, C is a capacitor, $\dot{z}(t)$ is the current; and F_{ex} represents the voltage. Accordingly, the average power extracted from the system is:

$$P_{av,reg} = \frac{1}{2} R_r \hat{v}^2 \tag{II.32}$$

with $\dot{z}(t) := v(t) = \hat{v}cos(wt + \psi)$

Irregular Waves

An irregular wave is, as shown in Fig.II.14, the superposition of regular waves with random amplitudes and periods. The sea surface elevation in the case of irregular waves is:

$$Z(t) = \sum_{n=1}^{\infty} \hat{A}_n e^{jw_n t} \tag{II.33}$$

The magnitude $\hat{A}_n$ and the period $T_n = \frac{2\pi}{w_n}$ are random variables with Normal distribution.

When a linear system has a sum of independent random variables as an input, its output

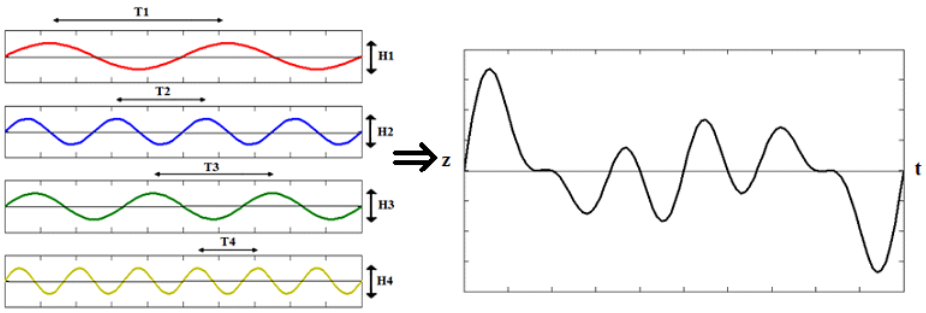

Figure II.14: An irregular wave is the superposition of regular waves with random amplitudes and periods.

is calculated using the inputs' power spectrum [Fal02]. From eq.II.31, the system velocity power spectrum for the case of irregular waves and a sea state (i), is given by:

$$S_{vi}(w) = |G(w)|^2 \, S_{Zi}(w) \tag{II.34}$$

where $G(w)$ is the relation between the velocity and the position depending on w. Again, from [Fal02], the amplitude of the system velocity can be found by applying the inverse Fourier transformation:

$$\hat{v} = \sqrt{TF^{-1}[S_{vi}(w)]} \tag{II.35}$$

and the average power in the case of irregular waves is:

$$P_{av,irr} = \frac{1}{2} R_r TF^{-1}[|G(w)|^2 \, S_{Zi}(w)] \tag{II.36}$$

II.3.c Power Maximization Techniques

Now that the average power expression is found for both, regular and irregular waves, techniques to maximize it are discussed. Among the various used methods, three are presented here. The optimal amplitude control, which acts on the parameter R_r, the optimal phase control that controls the phase between the floating body and the wave; and finally a combination of both previous methods, called the reactive control.

II.3.c-i Optimal Amplitude Control

From an electric point of view, this method aims at finding a tuning value R_{PTO} (Power Take Off) that can be added to R_r in eq.II.31, in order to maximize the extracted power expressed in eq.II.32. In the frequency domain, eq.II.31 is written as:

$$\frac{wZ(w)}{F_{ex}(v)} = \frac{1}{\frac{C}{w} - (m + m_r)w + j(R_r + R_{PTO})} \tag{II.37}$$

Thus,

$$P_{av} = \frac{1}{2} \frac{R_{PTO}}{(\frac{C}{w} - (m + m_r)w)^2 + (R_r + R_{PTO})^2} \hat{F}_{ex}(w) \tag{II.38}$$

The optimal value of R_{PTO} verifies the condition,

$$\begin{aligned} \tfrac{\partial}{\partial R_{PTO}}(P_{av}) = 0 \quad &\Rightarrow \\ \hat{R}_{PTO} &= \sqrt{R_r^2 + [(m + m_r)w - \tfrac{C}{w}]^2} \end{aligned} \tag{II.39}$$

and the corresponding obtained power is

$$P_{av} = \frac{1}{4} \frac{\hat{F}_{ex}(w)}{R_r + \sqrt{R_r^2 + [(m+m_r)w - \frac{C}{w}]^2}} \tag{II.40}$$

II.3.c-ii Optimal Phase Control

Corresponding to the same electric analysis, extracted power can also be maximized by synchronizing the force (voltage) F_{ex} and the velocity (current) v, which means:

$$(m+m_r)w - \frac{C}{w} = 0 \tag{II.41}$$

This condition is independent from the type of the wave energy system. It can be achieved by applying a latching control, as proposed in [BDC04], [FJH09] and [Fal02]. The control blocks the floating body for a suitable time interval, then let it go when it arrives to the optimal phase position. Another proposed method, though too complicated to be used, is adding a controllable mass m_{sup} to the floating object in order to have:

$$(m+m_r+m_{sup})w - \frac{C}{w} = 0 \Rightarrow \hat{m}_{sup} = \frac{C}{w^2} - (m+m_r) \tag{II.42}$$

The corresponding average power is:

$$P_{av} = \frac{1}{2} \frac{R_{PTO}\hat{F}_{ex}^2}{(R_r + R_{PTO})^2} \tag{II.43}$$

II.3.c-iii Reactive Control

A combination of the two previous methods is the so-called reactive control. It is called reactive because the system reacts to each sea state by applying the suitable controls that maximize the extracted power. For the case of regular waves, the extracted power using a reactive control is the result of combining eq.II.40 and eq.II.43, which is

$$P_{av} = \frac{1}{8} \frac{\hat{F}_{ex}^2}{R_r} \tag{II.44}$$

For irregular waves it is impossible to define power maximization conditions for each frequency in the spectrum. A proposed solution is to optimize the parameters for the frequency where the power spectrum is at its maximum.

II.3.c-iv Comparison

The explained control methods are compared using Matlab for both regular and irregular waves. The testing floating body is a cylindrical one with a radius $r = 2m$ and a height $L = 1m$. It is assumed to be completely submerged and balanced.

The body's mass is $m = \rho(\pi r^2)L = 1.291 \times 10^4$ kg. The parameters F_{ex}, m_r, R_r, C of this object are calculated using WAMIT software. They are functions of the wave period. Fig.II.15 shows the variations ofthe radiation parameter R_r and the added mass m_r as a function of wave's period. C's variations with frequency are neglected:

$$C = 1.264 \times 10^5$$

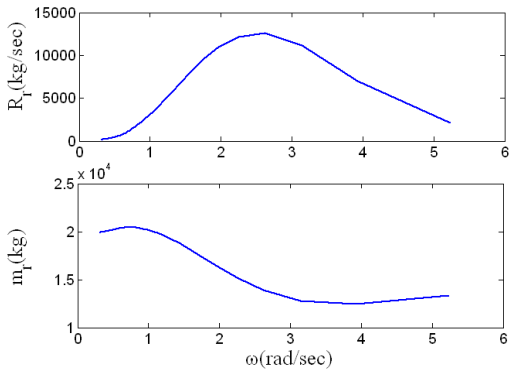

Figure II.15: Floating body parameters, added mass m_r and radiation parameter R_r.

In addition to the wave frequency, the excitation force F_{ex} is a function of the wave amplitude H. Its variations are shown in Fig.II.16.

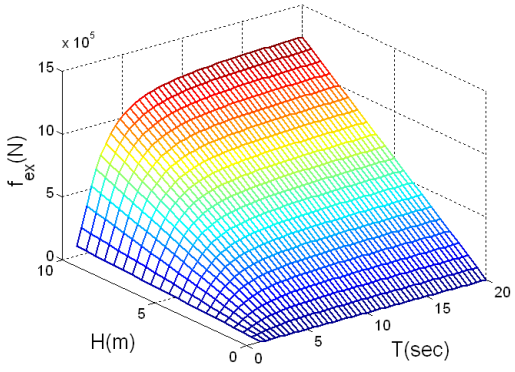

Figure II.16: The resulted excitation force as a function of the wave parameters.

At first, the waves are considered to be regular. For a wave ($H = 1.25m, T = 6.5sec$), the profiles of power generated using each power maximization methods are compared.

As noticed in Fig.II.17, the power generated using an optimal phase control is as high as that generated when applying a reactive control, and both generate almost 16 times the power generated using an optimal amplitude control.

In the case of irregular waves, waves are considered as a superposition of regular waves with random amplitudes and periods (eq.II.33). As seen earlier, in the case of irregular waves, the power spectrum is used to choose the suitable controls. Jonswap spectrum is adopted here [BTDB10]. It is the (Joint North Sea Wave Project) spectra that is an empirical approximation of the power distribution with respect to waves frequency:

$$S_{Zi} = \alpha H_{si}^2 f_{pi}^4 f^{-5} \gamma^{\beta} e^{[\frac{-5}{4}(\frac{f_{pi}}{f})^4]} (m^2 s) \tag{II.45}$$

where $T_{pi} = 1/f_{pi}$ and H_{si} are the wave period and amplitude respectively for a certain sea state, $\gamma = 3.33$ is the scaling factor, and α, β are given by

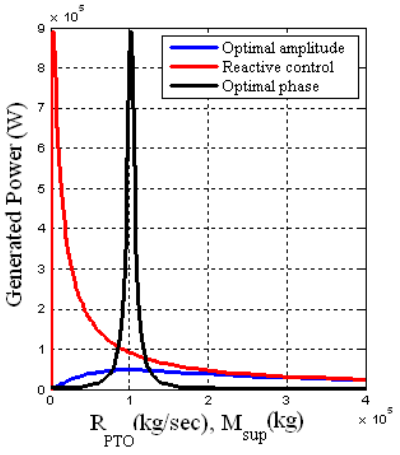

Figure II.17: Comparing generated Power in the case of a regular wave ($H = 1.25m, T = 6.5sec$).

$$\alpha = \frac{0.0624}{0.23+0.336\gamma-\frac{0.185}{1.9+\gamma}}, \quad \beta = e^{[-\frac{f-f_{pi}}{2\sigma^2 f_{pi}^2}]}$$

with

$$\sigma = \begin{cases} 0.07f < f_{pi} \\ 0.09f \geq f_{pi} \end{cases}$$

The average power in this case is written by:

$$P_{av,irr} = \int_0^\infty R_{PTO} \left|H(w)\right|^2 S_{Zi}(w)dw \tag{II.46}$$

For example, the empirical approximation for the sea state of Fig.II.14 is given by the curve in Fig.II.18.

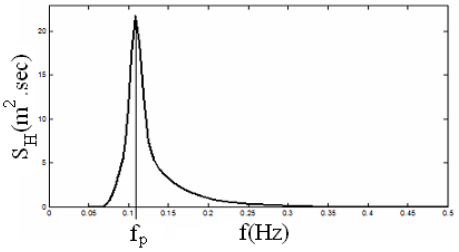

Figure II.18: Jonswap spectrum of wave in Fig.II.14.

Considering the set of sea states in Table II.1, the average power is calculated for each state using eq.II.46 and maximized via optimal amplitude control and reactive control. Fig.II.19 compares the resulted average power in the case of regular and irregular waves.

Using reactive control certainly increases the power efficiency. The increment is more significant in the case of regular waves.

As shown in Fig.II.20, comparing the produced energy without control, using a latching control and applying an optimal reactive control shows that even though in the case of

Table II.1: Test sea states

State	$H_s(m)$	$T_p(sec)$
1	0.25	4.8
2	0.5	4.8
3	0.1	4.8
4	1.5	6.4
5	2.0	6.4
6	2.5	8.4
7	3.5	8.4
8	3.5	9.2

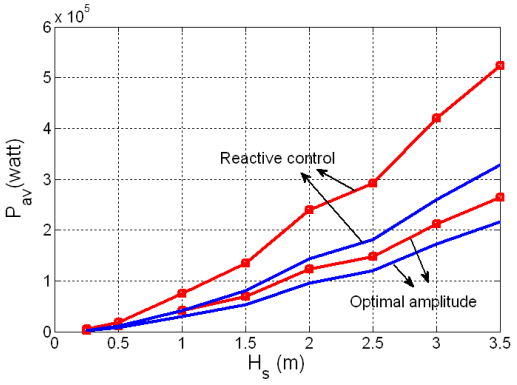

Figure II.19: Average power for regular (marked line) and irregular waves by applying reactive and optimal amplitude control.

optimal control the system has consumption phases periodically, the overall generated energy is greater than that obtained without using a control or using a latching control. The output power profile of the system in this case is similar to that of the KGS system discussed earlier in sec.II.2. Hence, from a grid integration point of view, both systems can be handled in the same way.

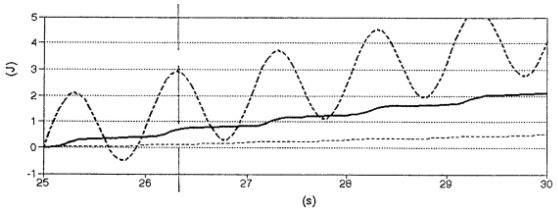

Figure II.20: Absorbed energy without phase control (lower broken curve), with latching phase control (fully drawn curve) and with theoretically ideal optimum control (broken wavy curve). The curves show the wave energy (in joule) accumulated during 5 seconds.

II.4 Conclusion

In this chapter, two relaxation-cycle renewable energy systems were presented and modeled. Those are the kite generator system (KGS) which is a kite-based traction system that

aims to harness high altitude wind energy, and the heaving point-absorber system (HPS) which is basically a floating body that captures sea waves oscillations and transforms them to a rotary movement employed to produce electricity.

We have to make a choice to conduct research on the maximization of harvested power. The kite generator system is more complex due to its multidimensional behavior: 3D in space for the kite and a torque/speed couple for the ground electric machine.

The obtained KGS models will be used to build and test controllers to control the kite's orientation and estimate its traction force and radial velocity.

Chapter III

Kite Generator System: Supervision

Contents

Abstract

The KGS control can be divided into two coupled parts, the kite orientation and the ground-based electric machine control. Simply stated, the kite orientation mechanism controls the roll angle of the kite, while driving the machine controls the tether radial velocity.

This chapter is dedicated to presenting the KGS orbit optimization and tracking. Two control methods are investigated: A nonlinear model predictive controller (NMPC) and a virtual constraints-based control (VCC).

The NMPC was already applied and tested, and it showed good results. It underwent a lot of research as well to improve its efficiency for real-time application. The second method, the VCC, is a novel application of virtual constraints used in robotics control and the primer study presented here shows its potential to achieve orbit tracking via a simplified approach.

The control strategy based on these controllers is built and tested through simulations.

III.1 Introduction

Generally, a kite-based system control should, on one hand, ensure the kite's (or kites set) tracking of certain orbits that respect the systems constraints and maximize the generated average power, and, on the other hand, manage the power generated/consumed by the system.

The reference trajectory generation is usually done either by choosing an eight-shaped orbit and optimizing its period and velocity to have a maximum power generation, as suggested by Argatov [AS10a], and used in [IHD07] and [WLO07a]; or by maximizing the generated power directly while following an imposed eight-shaped path that respects the state constraints as KiteGEN team has done [FMP10].

A general model of the system has the form,

$$\dot{x}(t) = f(x(t), u(t), P(t)) \tag{III.1}$$

with constraints on the state $x(t)$ and the control vector $u(t)$,

$$x_{min} \leq x(t) \leq x_{max}, \quad u_{min} \leq u(t) \leq u_{max} \tag{III.2}$$

The state vector $x(t)$ contains information on the kite's position and velocity, usually presented in the spherical coordinates (r, θ, ϕ). Meanwhile, the control vector $u(t)$ may contain controls of the kite's different angles: roll, yaw and attack, in addition to control of the tether length variation rate. As for $P(t)$, it contains all the external effects that influence the system behavior, e.g. wind perturbations and grid voltage dips. Depending on the system design and the measurement sensors, the control strategy is built.

Measuring the state vector can be done through use of observers or sensors such as GPS receivers, Gyro sensors connected to the ground control unit through wireless communication, and on-ground traction force and inclination angle measurements. The mentioned constraints include:

- The kite flying in a limited area and avoiding being crashed.
- Not exceeding a certain velocity or lift force that is specified by the kite's and tether's properties and respects the ground-based electric machine limits.
- Constraints on the control variables and their changing rates.

As the kite-based system is nonlinear, constrained, and unstable in the open-loop, an equally complex sophisticated autonomous control strategy should be applied, with a sufficiently small sampling time to insure the tracking of any possible disturbance.

A simple linear control [WLO07a] is not suitable to control such a system as it cannot handle disturbances and is only efficient around the linearizing point. A nonlinear model predictive control (NMPC) was proved to be convenient to generate the needed controls for trajectory tracking, though [BO11] doubted the performance of this method because it leads the solution to converge to different local optima depending on the initial conditions and consumes a lot of memory when it comes to application. Still NMPC was used in [IHD07], [AHB11b], and for real time application a Fast NMPC was proposed and tested

by KiteGen team [CFM10].

Neural network control [FH07] has demonstrated promising results in applying a robust tracking of the kite trajectory facing severe wind disturbances. Meanwhile, J. Baayen and W. Ockels have suggested a one-dimensional representation of the trajectory that allows the transformation of the trajectory tracking problem to single-input single-output (SISO) problem and used a nonlinear adaptive control to achieve the trajectory tracking [BO11]. Other suggested trajectory tracking methods include direct-inverse control [NFM11] and robust control [PO07b].

In this chapter, two methods to control the system are proposed. The first uses a nonlinear model predictive controller (NMPC), a method that was already applied and tested and it showed good results in this domain. The second approach is a novel one investigated and proposed in this thesis. It is called: Virtual constraints-based control (VCC). The methodology of using both controllers and their application via simulations is presented in the following sections.

III.2 Nonlinear Model Predictive Controller

Model predictive control (MPC), also called receding horizon control, is a multi-variable control based on iterative finite horizon optimization.

As shown in Fig.III.1, at an instance t, the current control action u_i is obtained by solving numerically an optimal control problem on a finite time horizon $[t, t+T]$. The control problem is constrained by limits $\{p\}_i$ on the system, the control and the state measurement. It uses the current state x_i as the initial state and yields an optimal control sequence $\{u_{i+1}(t), u_{i+1}(t+t_s), ..., u_{i+1}(t+T)\}$ in which t_s is the calculation step. The first control $u_{i+1}(t)$ is applied to reach the next state x_{i+1}. The calculations are repeated starting from the new state to find the next control action and a new prediction path under the new constraints set $\{p\}_{i+1}$.

To sum up, the principle elements of the MPC method are:

- An internal dynamic model of the controlled system.
- A history of past control moves.
- An optimization cost function J over the prediction horizon.
- A set of constraints on the optimization algorithm.

MPC strategies were successfully employed in thousands of industrial applications, such as petrochemical industry and aerospace and car industry. MPC takes into account actuators limitations, and operates close to constraints, as well as it has the possibility to adapt easily to changes in the system and its constraints.

A nonlinear model predictive control (NMPC) considers a nonlinear model for the prediction function and nonlinear constraints. It adds to linear MPC a new complexity which is the non-convexity of the optimal control problem, which poses challenges for NMPC's stability and numerical solution.

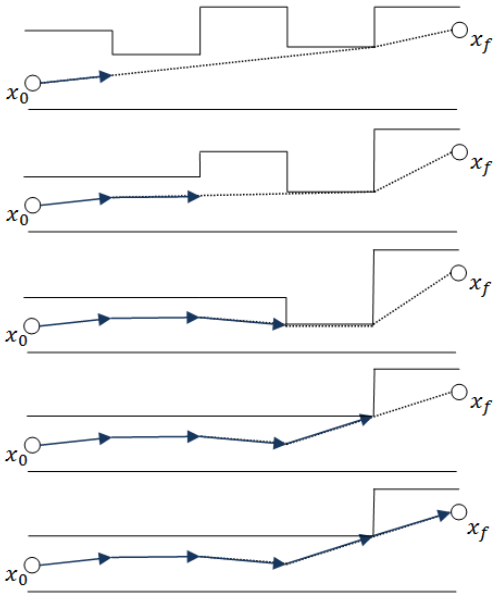

Figure III.1: Illustration of model predictive control output.

The numerical solution of the NMPC optimal control problems is typically based on direct optimal control methods, using Newton-type optimization schemes. They can make use of the fact that consecutive optimal control problems are similar to each other, hence initialize the Newton-type solution procedure efficiently by a suitably shifted guess from the previously computed optimal solution, saving considerable amounts of computation time, and permitting real time iterations.

III.2.a Methodology

In the next paragraphs, an NMPC-based control strategy is proposed to control the KGS system. It can be summarized by the following steps:

- Choosing primary eight-shaped orbit parameters.
- Optimizing the parametric orbit by maximizing its generated power.
- Finding the 3D time dependent trajectory.
- Applying an NMPC to insure trajectory tracking

Those steps are detailed in the following sections.

III.2.a-i Primary Orbit Choice

The initial kite orbit to be optimized is characterized by the tether's initial length r_0, and the parameters defining θ's and ϕ's variations space: $\Delta\theta, \Delta\phi, \theta_0, \phi_0$ and Rot (see Fig.III.2). The trajectory is expressed by the parametric equations:

$$\begin{aligned} \theta(\tau) &= \theta_0 + \cos(Rot)\Delta\theta\sin(2\tau) - \sin(Rot)\Delta\phi\sin(\tau) \\ \phi(\tau) &= \phi_0 + \sin(Rot)\Delta\theta\sin(2\tau) + \cos(Rot)\Delta\phi\sin(\tau) \end{aligned} \tag{III.3}$$

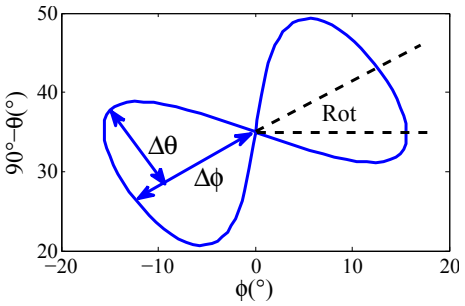

Figure III.2: Initial orbit parameters.

The primary trajectory parameters determine the maximum wind power that can be exploited by the KGS. The bigger the values of $\Delta\theta, \Delta\phi$ are, the bigger the orbit and the more average generated power is. Further more, the generated power increases with the orbits rotation angle *Rot*. The choice of the other parameters θ_0, ϕ_0 is dependent on the wind direction. These dependencies will be illustrated later in the discussion presented in sec.IV.4.d.

III.2.a-ii Orbit Optimization

The optimization phase aims at finding the radial velocity profile and the orbit's period that maximizes the produced average power during one cycle of the system, hence finds the maximum power cycle.

In order to do so, both the produced power and the closed orbit condition are expressed as functions of the dimensionless variable τ.

Remember that the system average mechanical power over one period T is:

$$\bar{P}_M = \frac{1}{T}\int_0^T F^{c,trc}(t)V_L(t)dt \tag{III.4}$$

where $F^{c,trc}$ is the traction force acting on the tether, and V_L is the tether radial velocity. According to [AS10a], by changing the integral time variable $t \in [0, T]$ to the dimensionless parameter $\tau \in [0, 2\pi]$, and making use of the substitution $V_L(t) = Vv(\tau)$, eq.III.4 can be expressed as follows:

$$\bar{P}_M(v) = \frac{1}{2}\rho_a A C_L G_e^2 V^3 J_0(v) \tag{III.5}$$

where V is the wind speed amplitude and J_0 represents the normalized average power $\bar{P}_M$ [ARS09], with the normalizing coefficient being: $\rho_a A C_L G_e^2 V^3$. J_0 is expressed by eq.III.6.

$$J_0(v) = \frac{\int_0^{2\pi}(w_{||} - v)vh(\tau)d\tau}{\int_0^{2\pi}\frac{h(\tau)}{w_{||}-v}d\tau} \tag{III.6}$$

with $h(\tau) = \sqrt{d\theta^2 + d\phi^2 sin^2(\theta)}$ and $w_{||} = sin(\theta)cos(\phi)$. When the attack angle α is constant, the aerodynamic coefficients are constant.

The aerodynamic efficiency G_e can however be controlled in order to improve the performance of the system. Eq.III.7 represents a possible functionality of this coefficient to the attack angle.

$$\begin{aligned} C_L &= C_{L0} + C_{L\alpha}\alpha \\ C_D &= C_{D0} + K * C_L^2(\alpha) \\ G_e &= \frac{C_L}{C_D} \end{aligned} \tag{III.7}$$

where α is written as a linear function of the $w_{||}$ and its variations can be optimized when joined to the average mechanical power expression of Eq.III.5.

$$\alpha(\tau) = a_0 * w_{||}(\tau) - a_1 \tag{III.8}$$

$$a_0 = \frac{\alpha_{max} - \alpha_{min}}{w_{||max} - w_{||min}}$$

$$a_1 = \frac{\alpha_{max} w_{||min} - \alpha_{min} w_{||max}}{w_{||max} - w_{||min}}$$

Orbit optimization aims at having a high crosswind speed, in order to develop a high traction force and thus higher power production. The crosswind speed is expressed by:

$$|W_e^p| = G_e V (w_{||} - v) \tag{III.9}$$

This means the optimal tether radial velocity $\hat{v}(\tau)$ should be found. This velocity maximizes the produced power that was presented earlier by eq.III.6, and satisfies the closed loop orbit condition $\int_0^T V_L(t)dt = 0$, which is expressed by: [ARS09]

$$\int_0^{2\pi} \frac{v h(\tau)}{w_{||} - v} d\tau = 0 \tag{III.10}$$

Once found, $\hat{v}(\tau)$ is used to derive the traction force given by: [AS10a]

$$f_{trac} = \frac{1}{2}\rho_a A C_L G_e^2 V_v^2 (w_{||} - \hat{v})^2 - (m + m_t) g \cos\theta \tag{III.11}$$

III.2.a-iii Orbit Period

All done calculations and variables are functions of the dimensionless parameter $\tau \in [0, 2\pi]$. The orbit's time period T and the relation between the time variable $t \in [0, T]$ and τ need to be defined. The period equals the orbit length divided by the kite's speed:

$$T = \oint \frac{dl}{|\dot{r}|} \tag{III.12}$$

With dl a differential length along the orbit:

$$\vec{dl} = dr\vec{e}_r + rd\theta\vec{e}_\theta + r\sin\theta d\phi\vec{e}_\phi = (r'\vec{e}_r + r\theta'\vec{e}_\theta + r\sin\theta\phi'\vec{e}_\phi)d\tau = \vec{r}d\tau$$

The velocity vector $\vec{r}$ at a certain point of the orbit is carried on its tangent:

$$\vec{t}(\tau) = \frac{\vec{dl}}{\|dl\|} = \frac{r'\vec{e}_r + r\theta'\vec{e}_\theta + r\sin\theta\phi'\vec{e}_\phi}{\sqrt{r'^2 + r^2\left(\theta'^2 + \phi'^2\sin^2\theta\right)}}$$

It can be decomposed into two components:

$$\vec{\dot{r}} = r'\vec{e}_r + r\sqrt{\theta'^2 + \phi'^2\sin^2\theta}\,\frac{\theta'\vec{e}_\theta + \sin\theta\phi'\vec{e}_\phi}{\sqrt{\theta'^2 + \phi'^2\sin^2\theta}} = r'\vec{e}_r + |\vec{\dot{r}}_\perp|\vec{t_\perp}$$

and this can be written as:

$$\vec{\dot{r}} = |\vec{\dot{r}}_\perp|\frac{r'\vec{e}_r + r(\theta'\vec{e}_\theta + \sin\theta\phi'\vec{e}_\phi)}{r\sqrt{\theta'^2 + \phi'^2\sin^2\theta}}$$

the effective wind tangent component is:

$$|W_e^p|^2 = |\vec{W}_\perp - \vec{\dot{r}}_\perp|^2 = |\vec{W}_\perp|^2 + |\vec{\dot{r}}_\perp|^2 - 2|\vec{\dot{r}}_\perp|(\vec{W}_\perp.\vec{t}_\perp)$$

By adding and subtracting $(\vec{W}_\perp.\vec{t}_\perp)^2$,

$$|\vec{\dot{r}}_\perp| = \vec{W}_\perp.\vec{t}_\perp + \sqrt{(\vec{W}_\perp.\vec{t}_\perp)^2 + |W_e^p|^2 - |\vec{W}_\perp|^2} \tag{III.13}$$

Due to the crosswind motion law $|W_e^p| = G_e(V_{||} - \dot{r})$ and putting $\Omega_\perp = \vec{W}_\perp.\vec{t}_\perp$, eq.III.14 is written as:

$$|\vec{\dot{r}}_\perp| = \vec{W}_\perp.\vec{t}_\perp + \sqrt{\Omega_\perp^2 + G_e^2(V_{||} - \dot{r})^2 - |\vec{W}_\perp|^2} \tag{III.14}$$

Eq.III.12 gives: [AS10a]

$$T = \oint \frac{r\sqrt{\theta'^2 + \sin\theta\phi'^2}}{|\vec{\dot{r}}_\perp|}d\tau \tag{III.15}$$

The quantity G_e has a high value; therefore, the mathematical model of wind energy generation can be further simplified to:

$$\frac{|\vec{\dot{r}}_\perp|}{V} = \omega_\perp + \sqrt{\omega_\perp^2 + G_e^2(w_{||} - v)^2 - |\vec{w}_\perp|^2} = G_e(w_{||} - v)$$

Hence, the period can be finally expressed in eq.III.16.

$$T = \int_0^{2\pi} \frac{r(\tau)h(\tau)}{G_e(w_{||}(\tau) - v(\tau))}d\tau \tag{III.16}$$

and the time vector is given by:

$$t = \int_0^{\tau} \frac{r(\sigma)h(\sigma)}{G_e(w_{||}(\sigma) - v(\sigma))}d\sigma \tag{III.17}$$

III.2.a-iv NMPC Design

Now that the optimal tether's radial velocity and the period corresponding to a given eight-figured orbit are found, the nonlinear model predictive control is applied to achieve tracking of the generated orbit while respecting the system's constraints. This is done via control of the kite roll angle and the tether's traction force, in addition to the attack angle if the aerodynamic efficiency is optimized as well.

The resulted kite orbit is a three-dimensional orbit described in the spherical coordinates by $r(t), \theta(t), \phi(t)$. Orbit tracking is divided into:

- Kite orientation via the control of its roll angle to follow the reference $(x, \dot{x}) : x = (\theta, \phi)$
- Tether's radial velocity control by driving of the PMSM rotation velocity ($V_L = \Omega_s / K$).

At every time step, $\ddot{x}$ that minimizes the cost function of eq.III.18 is calculated and controlled by the roll angle ψ. The chosen cost function reflects the distance from the reference orbit.

$$f = \|(\ddot{x}_{ref} - \ddot{x}) + \lambda_1(x_{ref} - x) + \lambda_2(\dot{x}_{ref} - \dot{x})\|^2 \tag{III.18}$$

where λ_1, λ_2 determine how quickly the state converges to the reference orbit.

Fig.III.3 summarizes the KGS proposed NMPC-control strategy. It starts from the parametric initial orbit and generates an optimal time-dependent orbit. An NMPC is applied to find the roll angle that achieves tracking of $(\theta(t), \phi(t))$, while the radial velocity control is insured by controlling the ground machine rotation velocity.

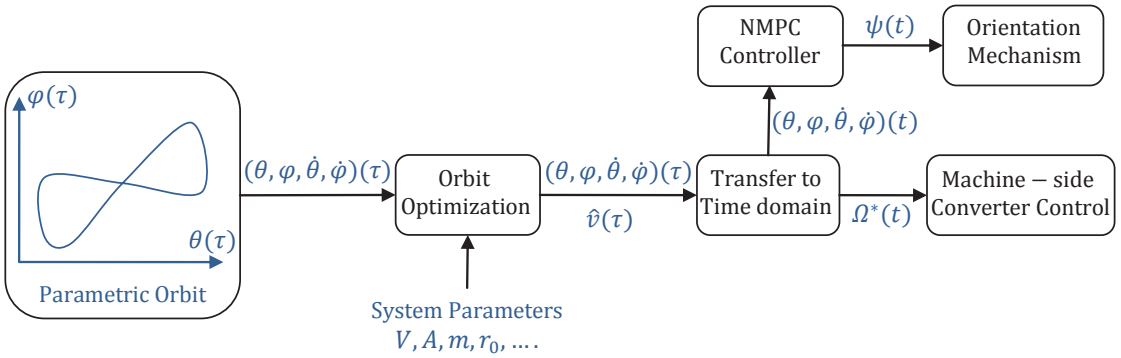

Figure III.3: NMPC-based control strategy.

III.2.b Application

As mentioned earlier, choosing the primary orbit to be optimized is an essential step in determining the maximum possible extracted average power, and the ratio between the average and the maximum power, or what we choose to call "Performance". Table.III.1 shows the KGS parameters. The wind velocity is assumed to be constant and regular with a speed $V = 4m/s$. Fig.III.4 shows the test orbits. Test orbits 2 and 3 result from amplifying the reference test orbit 1, while orbits 4 and 5 result from rotating the reference orbit 30 and 90 degrees respectively.

Table.III.2 shows the characteristics of the five chosen test orbits with $\theta_0 = 55^o$ and $\phi_0 = 0^o$, as well as the estimated corresponding mean power, performance, and the orbits' period.

In [AS10b], it was demonstrated that a bigger trajectory corresponds to greater average power; furthermore, a bigger rotation of the orbit leads to more average power which agree with the results obtained and displayed in Table.III.2. As noticed, the performance gets better as well, because a bigger orbit allows the kite recovery phase to occur further from

Table III.1: Kite generator system parameters

R	0.3	Rotor Diameter (m)
Ω_{max}	25	Maximum rotor rotation velocity (rd/sec)
Γ_{max}	22	Motor maximum torque $(N.m)$
m	2.5	Kite mass (kg)
A	5	Kite area (m^2)
ρ_a	1.2	Air density (kg/m^3)
C_L	1.5	Lift coefficient
C_D	0.15	Drag coefficient
T_s	0.1	Sampling time (sec)

the center of the power region; hence, consumes less energy. The size, however, is a parameter to be optimized according to the system's location.

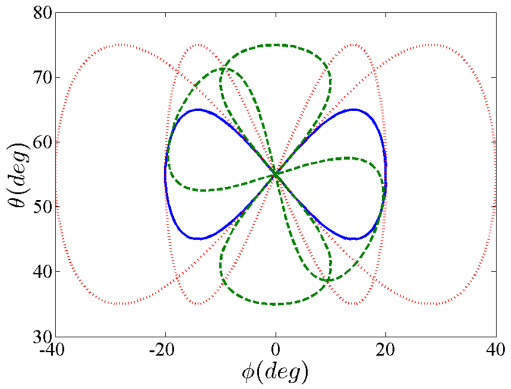

Figure III.4: Test orbits: Reference orbit (1) in continuous line, amplified orbits (2,3) in dotted line, and rotated orbits (4,5) in dashed line.

The orbits optimization results in the normalized parametric radial velocity $\hat{v}$ which depends on the wind direction and the parametric orbit. The time dependent radial velocity profile is found after calculating the orbit period and time vector (eq.III.16,eq.III.17). The resulted profiles in the case of orbits $1, 2$ and 3 are shown in Fig.III.5. Notice that the optimal velocity has double the calculated period, so during one orbit two traction and two recovery phases occur. This means doubling the resulted power profile and decreases its continuity. The upper plot of Fig.III.7 shows the KGS energy profile for the orbits $1, 2$ and 3.

Fig.III.6 shows the radial velocity profiles for orbits 4 and 5 compared to the reference orbit 1. Rotating the orbit results in more average generated power and increases the performance without the need to increase the orbit size or changing the system parameters. Contrary to the case of 0^o rotation, a 90^o rotated orbit preserves the orbit period, which means only one traction and one recovery phase during the orbit. This can be also observed by the energy profiles shown on the lower plot of Fig.III.7.

As noticed, the KGS will offer a very high adaptivity, as its rated power can be modified

Table III.2: Testing orbits parameters and optimized orbits' period, mean mechanical power and performance

Orbit	1	2	3	4	5
$\Delta\theta$	10^o	20^o	20^o	10^o	10^o
$\Delta\phi$	20^o	20^o	40^o	20^o	20^o
Rot	0^o	0^o	0^o	30^o	90^o
Period (sec)	35.4	59.0	78.4	35.4	35.0
Mean power (W)	240	732	844	398	840
Performance	0.058	0.094	0.108	0.058	0.100

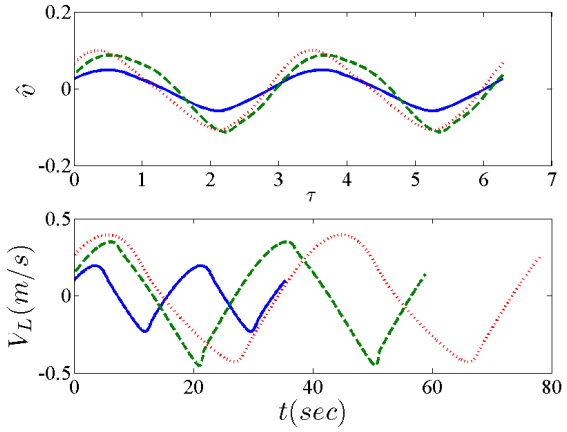

Figure III.5: Normalized and time dependent radial velocity in upper and lower figure respectively. Reference orbit (1): continuous, orbit (2): dotted, orbit (3): dashed.

by changing the kite orbit size and/or rotation. It can also be modified by changing the orbit inclination θ_0, or the altitude at which the kite is flying for example. Fig.III.8 shows how the KGS generated average power changes as a function of the kite surface A, the orbit rotation angle Rot, and the orbit inclination θ_0.

The NMPC controls the kite to follow the generated reference orbit while respecting the state and control constraints. Those are usually imposed by the area the system is flying in and the flight angle's limits. Assuming the kite flight is limited only by the ground and the tether length, the following constraints are applied:

$$\begin{aligned}
\theta_{min} = 30^o &\leq \theta &&\leq \theta_{max} = 90^o \\
\phi_{min} = -90^o &\leq \phi &&\leq \phi_{max} = 90^o \\
r_{min} = 90\ m &\leq r &&\leq r_{max} = 110\ m \\
\dot{r}_{min} = -83.3\ m/sec &\leq \dot{r} &&\leq \dot{r}_{max} = 83.3\ m/sec \\
\psi_{min} = -20^o &\leq \psi &&\leq \psi_{max} = 20^o \\
\dot{\psi}_{min} = -4^o/sec &\leq \dot{\psi} &&\leq \dot{\psi}_{max} = 4^o/sec
\end{aligned}$$

Fig.III.9 shows the orbit tracking by applying the already explained optimal predictive

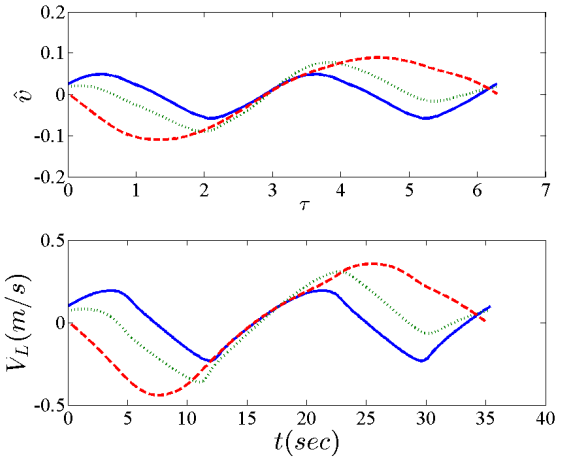

Figure III.6: Normalized and time dependent radial velocity in upper and lower figure respectively. Reference orbit (1): continuous, orbit (4): dotted, orbit (5): dashed.

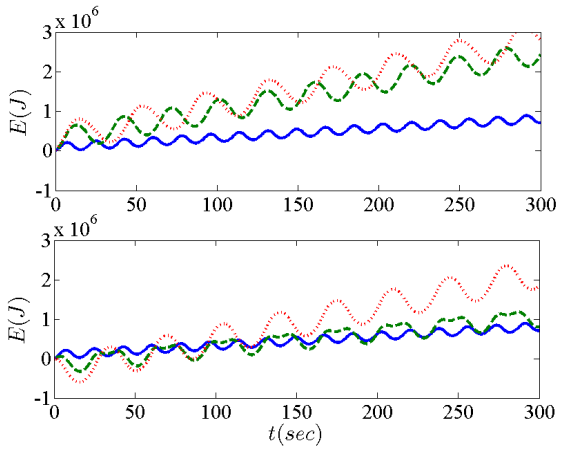

Figure III.7: KGS energy generation. Reference orbit (1): continuous. Upper plot: orbit (2) energy profile in dotted line, orbit (3): dashed. Lower plot: orbit (4) energy profile in dotted line, orbit (5): dashed.

control in the case of the first orbit. Here the radial velocity, hence the tether length, is assumed to be controlled by the ground machine as will be shown in the next chapter.

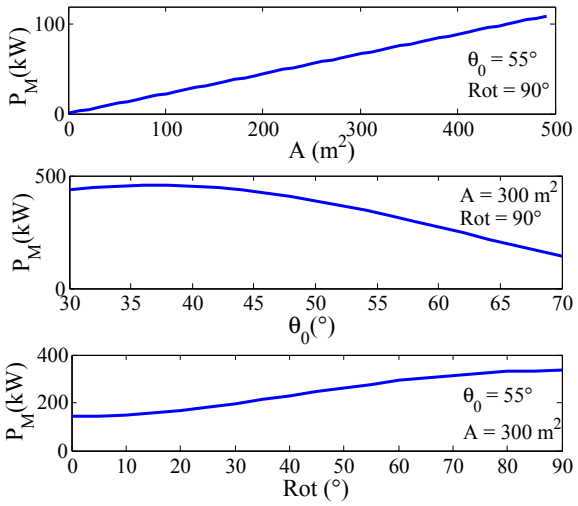

Figure III.8: Starting from upper plot: The average mechanic power as a function of the kite surface A, the inclination angle θ_0; and the orbit rotation Rot.

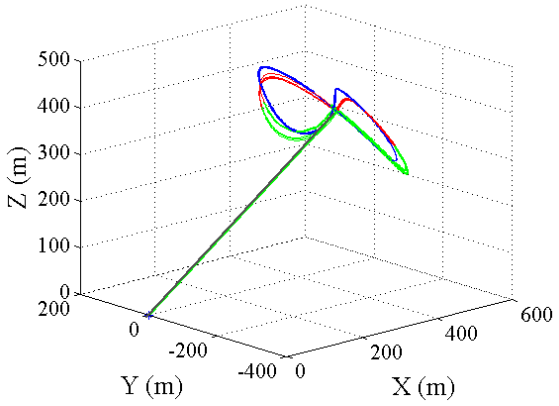

Figure III.9: Tracking orbit 1 using optimal predictive control

III.3 Virtual Constraints-based Controller

In this section, the KGS periodic target motion is ensured by a state feedback control law based on virtual constraints approach. The proposed motion planning strategy is a fast in-loop control method that is robust against disturbances and guarantees an exponential orbital stabilization. Virtual constraints (VC) are dynamically enforced relations between a mechanism's links in order to decrease its degrees of freedom. They coordinate the movement of all links by controlling a single variable.

Virtual constraints have emerged recently as a valuable tool to solve motion control problems. This notion has been useful to design controllers for biped robots, as well as, control of underactuated 3DOF helicopter movement [WMS10], pendubot [FRSJ08], and cart-pendulum system [SPCdW05]. Fig.III.10 presents some control problems that were solved using VC.

For an under-actuated Euler-Lagrange system, VC are defined as relations among the sys-

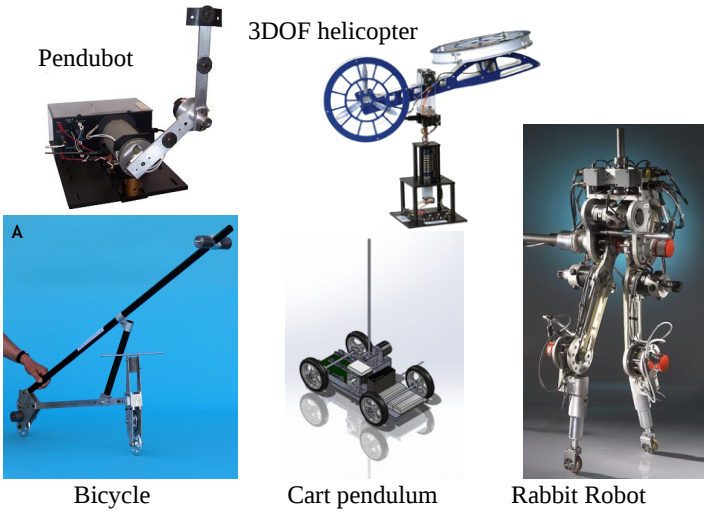

Figure III.10: Some motion and balance control problems solved using VC.

tem's variables and are enforced by feedback. The goal of the feedback design is either to render an existing periodic motion orbitally stable or to force the system dynamics to generate a new periodic motion and ensure its orbital stability [SCdW03][CdW04].

Considering the non-linear Euler-Lagrange system :

$$\frac{d}{dt}(\frac{\partial L}{\partial \dot{q}}) - \frac{\partial L}{\partial q} = B(q)u \tag{III.19}$$

Where:

- q is the generalized coordinates vector.
- $\dot{q}$ is q's velocity vector.
- u is the independent control inputs vector.
- B is the control matrix.
- $L(q, \dot{q}) = T(q, \dot{q}) - V(q)$ is the Lagrangian, that is the difference between the kinetic energy $T = \frac{1}{2}\dot{q}^T M(q)\dot{q}$, where M is a positive definite matrix of inertia, and the potential energy of the system V.

Suppose that this system has n degrees of freedom controlled via $n-1$ inputs; it is then under-actuated.

$$dim(u) < dim(q)$$

In this case, $n-1$ virtual constraints can be imposed on the system's generalized coordinates as follows:

$$\begin{cases} q_1 &= \Phi_1(q_n) \\ q_2 &= \Phi_2(q_n) \\ \vdots & \\ q_{n-1} &= \Phi_{n-1}(q_n) \end{cases} \tag{III.20}$$

and the system III.19 can be reduced to an auxiliary input-free system with a limit cycle:

$$\alpha(\theta)\ddot{\theta} + \beta(\theta)\dot{\theta}^2 + \gamma(\theta) = 0 \tag{III.21}$$

where $\theta \stackrel{\text{def}}{=} q_n$ and $\alpha(\theta), \beta(\theta), \gamma(\theta)$ are scalar functions of θ. This equation represents also the zero or the reduced dynamics of the system.

The next example clarifies the virtual constraints approach.

Example: *A two-joint robot arm has two DOF: two rotations q_1, q_2. Controlling the arm's free end to move along a vertical axis implies forcing the virtual constraint of eq.III.22 that couples both rotations.*

$$q_2 = \Phi(q_1) = q_1 - \arcsin\left(\frac{l_1}{l_2}\sin(q_1)\right) \tag{III.22}$$

and can be expressed as well in the form:

$$y = q_2 - \Phi(q_1) = 0 \tag{III.23}$$

Since we are seeking a periodic motion stabilization of the kite generator system, the

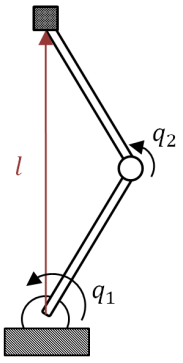

Figure III.11: Example of a virtually constrained Two joint arm.

VC approach seems a suitable one. In the following paragraphs, the constructive tool proposed by [SPCdW05] for orbital stabilization of under-actuated nonlinear systems will be employed.

The section starts by defining an Euler-Lagrange system, and listing the conditions a chosen virtual constraint must satisfy. Afterwards, the VC-based control methodology is proposed in section.III.3.a, and applied on the KGS in section.III.3.b.

Euler-Lagrange System

They are mechanical systems whose dynamics can be expressed by the Euler-Lagrange differential equation (eq.III.19). It can be also rewritten, as in [CM10], in the form:

$$D(q)\ddot{q} + C(q,\dot{q}) + \nabla P(q) = B(q)u \tag{III.24}$$

Where:

- $D(q)$ is the inertia matrix.
- $C(q, \dot{q})$ is the coriolis matrix.
- $\nabla P(q)$ is the potential energy Matrix.

The system eq.III.24 is under-actuated if its control inputs are less than its degree of freedom (DOF).

Feasible Virtual Constraints

The choice of the virtual constraint is determined by the system's desired orbit; thus, its functionality. The virtual constraint should be regular and stabilizable [CM10]. In order to be regular, it should satisfy one of the three conditions of [CM10]-proposition 3.2. One of those is:

$$B^{\perp}.D(\hat{\phi}(\theta)).\hat{\phi}'(\theta) \neq 0 \tag{III.25}$$

with $\hat{\phi}(\theta) = [\theta \ \phi(\theta)]$

It is necessary as well that the virtual constraint is stabilizable; which means that, there exists a smooth feedback $u(\theta, \dot{\theta})$ to enforce it. According to [CM10] parametric VCs are stabilizable.

Existence of Periodic Solution

As shown earlier, applying the VCs yields the reduced system of eq.III.21. Assume that:

- There exists an equilibrium θ_0 of the system in eq.III.21.
- $\alpha(\theta), \beta(\theta), \gamma(\theta)$ are continuous on a vicinity $O(\theta_0)$.
- There exists a continuous derivative of $\frac{\gamma(\theta)}{\alpha(\theta)}$ at $\theta = \theta_0$.
- $\forall \theta_0 \in O, \dot{\theta}_0$ with $|\dot{\theta}_0| < \delta, \delta > 0$, the solution of the nonlinear system III.21 that originates in this point is well-defined and unique.

According to [SRPS06]-Theorem 3, if an auxiliary linear system:

$$\frac{d^2 z}{dt^2} + \left[\frac{d}{d\theta}\frac{\gamma(\theta)}{\alpha(\theta)}\right]_{\theta=\theta_0}.z = 0 \tag{III.26}$$

has a center at $z = 0$, then the nonlinear system III.21 also has a center at the equilibrium θ_0.

Furthermore, if the reduced system has at least one periodic solution then the same feedback strategy, which is used to enforce the virtual constraints, results in generating a periodic motion for all the system's degrees of freedom.

III.3.a Methodology

The application of the VC-based control method can be summarized by the following steps:

- Finding the Euler-Lagrange model of the system.
- Choosing of a suitable virtual constraint.
- Applying of a partial feedback linearization, where the remaining nonlinear part is integrable.
- Constructing of an auxiliary linear periodic control system of reduced order.
- Designing of a LQR-based control for the auxiliary system.
- Modifying of the control developed in the previous item to be applied to the original nonlinear system.

These steps will be developed in detail in the following sections with a special attention to the studied KGS.

III.3.a-i KGS Under-actuated Model

For investigating the application of virtual constraints concept on the KGS, a simplified model of the later is considered. The chosen simplification matches the indoors tethered-wing prototype built and tested in GIPSA-Lab [HLAD13]. Here the KGS has two degrees of freedom, a translation along the tether r, and an angle θ. To have an under-actuated system, it is only controlled by one input that is the attack angle, α, while considering the tether tension constant. Fig.III.12 shows the reduced KGS and the GIPSA-Lab tethered-wing prototype.

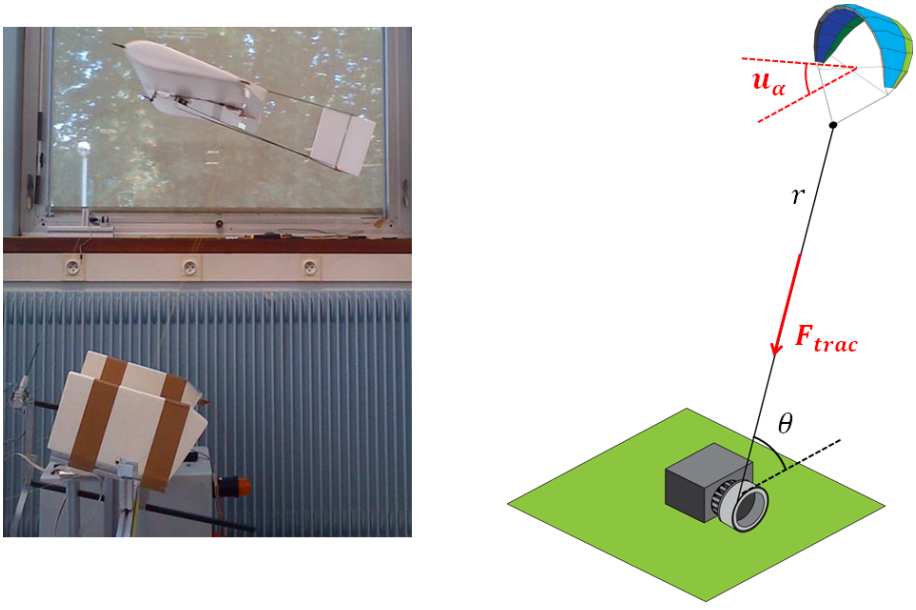

Figure III.12: From the left: The indoors tethered-wing prototype of GIPSA-Lab and its representation.

The following notations are used hereafter:

$$\begin{aligned} a &= \tfrac{1}{2}\rho_a S \\ b &= a(\tfrac{C_L^2}{\pi\lambda e} + C_{D_0}) \end{aligned}$$

where ρ_a is the air density, A is the kite surface, λ is the kite's aspect ratio, e is the Oswald efficiency factor, and C_L, C_D are the lift and drag coefficients as explained in Chapter.II.

The effective wind velocity's norm and angle, written in the polar coordinates r, θ, are expressed in eq.III.27.

$$\begin{aligned} W_e^2 &= (r\dot{\theta}\cos\theta + \dot{r}\sin\theta)^2 + (V + r\dot{\theta}\sin\theta + \dot{r}\cos\theta)^2 \\ \alpha_w &= -\arctan\left(\tfrac{r\dot{\theta}\cos\theta + \dot{r}\sin\theta}{V + r\dot{\theta}\sin\theta + \dot{r}\cos\theta}\right) \end{aligned} \tag{III.27}$$

with V being the wind speed. Taking the previously defined notations, the KGS dynamic model is given in eqs.III.28 and III.29.

$$\begin{cases} \ddot{\theta} + \frac{2\dot{r}\dot{\theta}}{r} + \frac{1}{rM}(bv_r^2\sin(\theta-\alpha_w) - av_r^2(\frac{\partial C_L}{\partial\alpha}\alpha_w + C_{L0})\cos(\theta-\alpha_w) + W\cos\theta) \\ = \frac{av_r^2}{rM}\frac{\partial C_L}{\partial\alpha}\cos(\theta-\alpha_w)\alpha_u \end{cases} \tag{III.28}$$

and

$$\begin{cases} \ddot{r} - \frac{M}{M+M_{IM}}r\dot{\theta}^2 + \frac{1}{M+M_{IM}}(bv_r^2\cos(\theta-\alpha_w) + av_r^2(\frac{\partial C_L}{\partial\alpha}\alpha_w + C_{L0})\sin(\theta-\alpha_w) - W\cos\theta - T) \\ = \frac{av_r^2}{M+M_{IM}}\frac{\partial C_L}{\partial\alpha}\sin(\theta-\alpha_w)\alpha_u \end{cases} \tag{III.29}$$

where M is the flying part mass and W is its weight, M_{IM} is the rotor's mass, α_u the attack angle control, and T is the tension in the tether. As noticed, the dynamics can be reduced to a single equation with no input.

III.3.a-ii Reduced Dynamics system

As mentioned above, the objective of the VC approach is to find a reduced dynamics system by applying a partial feedback linearization. The KGS dynamics of eq.(III.28,III.29) can be equally expressed by eq.V.12.

$$D(\theta,r)\begin{bmatrix}\ddot{\theta}\\ \ddot{r}\end{bmatrix} + C(\theta,r,\dot{\theta},\dot{r})\begin{bmatrix}\dot{\theta}\\ \dot{r}\end{bmatrix} + \nabla P(\theta,r) = B(\theta,r)\alpha_u \tag{III.30}$$

where:

- The Inertia matrix is:

$$D(\theta,r) = \begin{bmatrix} Mr & 0 \\ 0 & (M+M_{IM}) \end{bmatrix} \tag{III.31}$$

- The Coriolis matrix is:

$$C(\theta,r,\dot{\theta},\dot{r}) = \begin{bmatrix} 2M\dot{r} & 0 \\ -Mr\dot{\theta} & 0 \end{bmatrix} \tag{III.32}$$

- The Potential energy function is:

$$\nabla P(\theta,r) = \begin{bmatrix} bv_r^2\sin(\theta-\alpha_w) \\ -bv_r^2\cos(\theta-\alpha_w) \end{bmatrix} - \begin{bmatrix} av_r^2(\frac{\partial C_l}{\partial\alpha}\alpha_w + C_{L0})\cos(\theta-\alpha_w) \\ av_r^2(\frac{\partial C_l}{\partial\alpha}\alpha_w + C_{L0})\sin(\theta-\alpha_w) \end{bmatrix} + \begin{bmatrix} W\cos\theta \\ W\sin\theta + T \end{bmatrix} \tag{III.33}$$

- and the control matrix is:

$$B = av_r^2 \frac{\partial C_l}{\partial \alpha} \begin{bmatrix} \cos(\theta - \alpha_w) \\ \sin(\theta - \alpha_w) \end{bmatrix} \tag{III.34}$$

Suppose that there exists a control law of the under-actuated system (eq.III.30) that makes the constraint presented in (eq.III.22) invariant then the overall closed-loop system results in an input-free reduced system of the form of eq.III.35.

$$\alpha(\theta)\ddot{\theta} + \beta(\theta)\dot{\theta}^2 + \gamma(\theta) = 0 \tag{III.35}$$

with

$$\begin{aligned} \alpha(\theta) &= M\phi(\theta)\sin(\theta - \alpha_w) - (M + M_{IM})\phi'(\theta)\cos(\theta - \alpha_w) \\ \beta(\theta) &= (M\phi(\theta) - (M + M_{IM})\phi''(\theta))\cos(\theta - \alpha_w) \\ &\quad +2M\phi'(\theta)\sin(\theta - \alpha_w) \\ \gamma(\theta) &= bv_r^2 - W\sin(\alpha_w) - \cos(\theta - \alpha_w)T \end{aligned}$$

where $\phi'(.)$ and $\phi''(.)$ are respectively the first and second derivatives of the virtual constraint with respect to θ.

The chosen virtual constraint is stabilizable [CM10], because it is a parametric one. It must be regular as well, which implies that the system's variables should respect the condition in eq.III.25; hence, satisfy the inequality:

$$-M\phi(\theta)sin(\theta - \alpha_w) + (M + M_{IM})\phi'(\theta)cos(\theta - \alpha_w) \neq 0$$

Moreover, the resulted reduced system is a periodic Euler-Lagrange system [CM10] (Fig.III.13), which means that the same feedback strategy, used to enforce the VC, results in generating a periodic motion for all the system's degrees of freedom [SRPS06].

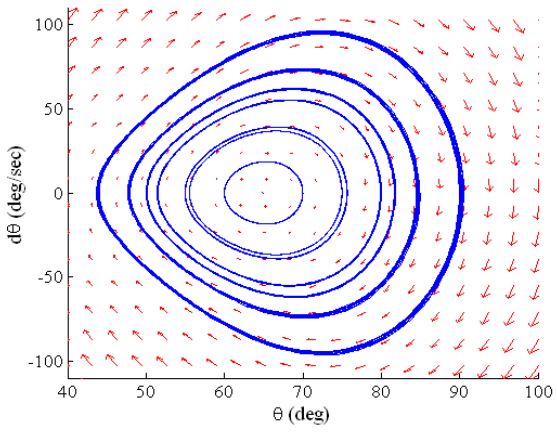

Figure III.13: The reduced system periodic orbits.

The objective is to design the feedback controller that guarantees the invariance of the chosen virtual constraints and an orbital asymptotic stability of the chosen periodic solution. This control problem can be expressed in eq.III.36

$$y = r - \phi(\theta) = 0, \ \theta(t) = \theta(t + T) \tag{III.36}$$

III.3.a-iii Partial feedback linearization

By introducing:

$$\begin{array}{rcl} r & = & y+\phi(\theta) \\ \dot{r} & = & \dot{y}+\phi'(\theta)\dot{\theta} \\ \ddot{r} & = & \ddot{y}+\phi''(\theta)\dot{\theta}^2+\phi'(\theta)\ddot{\theta} \end{array} \tag{III.37}$$

The Euler-Lagrange system of eq.III.30, can be written in the coordinates (θ, y) as follows:

$$L(\theta,y)\begin{bmatrix}\ddot{\theta}\\ \ddot{y}\end{bmatrix}+N(\theta,y,\dot{\theta},\dot{y})=[B(\theta,r)\alpha_u-C(\theta,r,\dot{\theta},\dot{r})\begin{bmatrix}\dot{\theta}\\ \dot{r}\end{bmatrix}-\nabla P(\theta,r)]_{r=y+\phi(\theta)} \tag{III.38}$$

with $L(\theta,y)=\begin{bmatrix}1 & 0\\ \phi'(\theta) & 1\end{bmatrix}$ and $N(\theta,y,\dot{\theta},\dot{y})=\begin{bmatrix}0\\ \phi''(\theta)\dot{\theta}^2\end{bmatrix}$.

The dynamics of the variable y are given by:

$$\ddot{y}=K(\theta,y)u+R(\theta,y,\dot{\theta},\dot{y}) \tag{III.39}$$

where $K(.), R(.)$ are given in eq.III.40.

$$\begin{array}{rcl} K(\theta,y) & = & \frac{\partial C_L}{\partial\alpha}\frac{av_r^2}{M(M+M_{IM})(y+\phi)}(-(M+M_{IM})\phi'\cos(\theta-\alpha_w)+M(y+\phi)\sin(\theta-\alpha_w)) \\ R(\theta,y,\dot{\theta},\dot{y}) & = & \frac{\phi'}{M(y+\phi)}(2M(\dot{y}+\phi'\dot{\theta})\dot{\theta}+bv_r^2 sin(\theta-\alpha_w)-av_r^2(\frac{\partial C_L}{\partial\alpha}\alpha_w+C_{L0})cos(\theta-\alpha_w)+Wcos\theta)-\phi''\dot{\theta}^2 \\ & & +\frac{1}{M+M_{IM}}(M(y+\phi)\dot{\theta}^2+bv_r^2 cos(\theta-\alpha_w)+av_r^2(\frac{\partial C_L}{\partial\alpha}\alpha_w+C_{L0})sin(\theta-\alpha_w)-Wcos\theta-T) \end{array} \tag{III.40}$$

According to eq.III.39, using the feedback transformation

$$u=K^{-1}(y,\theta)[v-R(\theta,y,\dot{\theta},\dot{y})] \tag{III.41}$$

results in a Partially linear system:

$$\begin{cases} \alpha(\theta)\ddot{\theta}+\beta(\theta)\dot{\theta}^2+\gamma(\theta)=g_y(\theta,\dot{\theta},\ddot{\theta})y+g_{\dot{y}}(\theta,\dot{\theta})\dot{y}+g_v(\theta)v \\ \ddot{y}=v \end{cases} \tag{III.42}$$

with

$$\begin{array}{rcl} g_y & = & -(M\sin(\theta-\alpha_w)\ddot{\theta}+M\cos(\theta-\alpha_w)\dot{\theta}^2) \\ g_{\dot{y}} & = & 2M\sin(\theta-\alpha_w)\dot{\theta} \\ g_v & = & (M+M_{IM})\cos(\theta-\alpha_w) \end{array}$$

As presented in [SFG10], if $\alpha(\theta_*(t))\neq 0, \forall t\in[0,T_p]$, then the integration I defined in eq.III.43 conserves a constant value on the reference orbit $(\theta_*,\dot{\theta}_*)$.

$$I(\theta_*,\dot{\theta}_*)=\frac{\dot{\theta}_*^2}{2}-\exp(-\int_{x_0}^{\theta_*}\frac{2\beta(\tau)}{\alpha(\tau)}d\tau)\left\{\frac{y_0^2}{2}-\int_{x_0}^{\theta_*}\exp(-\int_s^{\theta_*}\frac{2\beta(\tau)}{\alpha(\tau)}d\tau)\frac{2\gamma(s)}{\alpha(s)}ds\right\} \tag{III.43}$$

Introducing the new coordinates $\xi=[I,y,\dot{y}]^T$, the system of eq.V.18 can be also represented by eq.III.44.

$$\begin{cases} \dot{I}=\frac{2\dot{\theta}}{\alpha(\theta)}\left[g_y(t)y+g_{\dot{y}}(t)\dot{y}+g_v(t)v-\beta(\theta)I\right] \\ \ddot{y}=v \end{cases} \tag{III.44}$$

III.3.a-iv Controller Design

The resulted incomplete nonlinear system of eq.III.44 plays an important role in developing a stabilizing controller. Its state-space representation is:

$$\dot{\xi} = A(t)\xi + b(t)v \tag{III.45}$$

with $\xi = [I, y, \dot{y}]^T$, and:

$$A(t) = \begin{bmatrix} -\beta(\theta)\frac{2\dot{\theta}}{\alpha(\theta)} & g_y(t)\frac{2\dot{\theta}}{\alpha(\theta)} & g_{\dot{y}}(t)\frac{2\dot{\theta}}{\alpha(\theta)} \\ 0 & 0 & 1 \\ 0 & 0 & 0 \end{bmatrix}$$
$$b(t) = \begin{bmatrix} g_v(t)\frac{2\dot{\theta}}{\alpha(\theta)} & 0 & 1 \end{bmatrix}^T$$

One choice of the feedback controller v to exponentially stabilize the linear periodic system (eq.III.45) can be inspired from [SRPS05] where an LQR control is applied. The feedback controller can take the following form:

$$v = -\Gamma^{-1}b(t)R(t)\xi \tag{III.46}$$

where $R(t)$ is a symmetric matrix $R(t) = R(t)^T$ for all $t \in [0, T_p]$, periodic $R(t) = R(t + T_p)$, and satisfies the Riccati equation:

$$\dot{R}(t) + A(t)^T R(t) + R(t)A(t) + G = R(t)b(t)\Gamma^{-1}b(t)^T R(t)$$

Γ is a positive scalar and G is a (3×3) positive symmetric matrix.

The final obtained control diagram is shown in Fig.III.14. First, the KGS input is linearized through feedback. Then, the KGS model is reduced via insertion of the VCs. The introduction of the full integral I yields a partially linear system for which the stabilizer is designed.

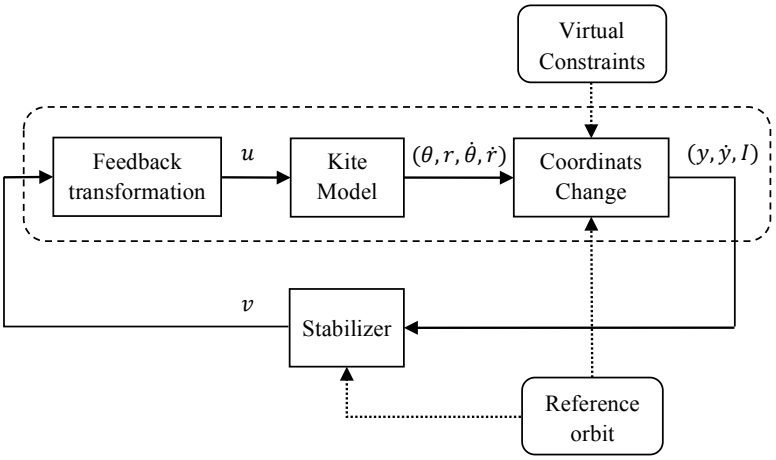

Figure III.14: Control block diagram.

To end, the obtained solution for the reduced system of eq.III.35 is a solution of the closed-loop KGS system, which is expressed by Theorem.1.

Theorem 1. *Given the under-actuated Euler-Lagrange KGS (eq.III.30) with 2 degrees of freedom (the tether's inclination and length (θ, r)) and one control input (the attack angle α), and applying the virtual constraint results in the reduced system (eq.III.35) which has a time-periodic solution. Writing the dynamics of y and introducing the integral I (eq.III.43,III.39), results in the linear*

periodic in time system eq.III.45 completely controllable over the system's period. Then the control solution eq.III.46 for the resulted system is exponentially orbitally stable solution for the closed-loop system (III.28), (III.29), (III.41), and (III.46).

The construction of the obtained solution implies that it is one of the solutions for the closed-loop system (Theorem 3 - [SPCdW05]).

III.3.b Application

To show the effectiveness of the proposed feedback control, a simulation study was performed using the coefficients of the experimental set-up of GIPSA-Lab [HLAD13]. They are given in Table.III.3.b.

symbol	name	value
M	mass	0.1 Kg
M_{IM}	rotor's mass	0.0481 Kg
ρ	air density	1.225 Kg/m^3
S	wing area	0.1375 m^2
e	Oswald's factor	0.7
λ	aspect ratio	2.5
$\partial C_L/\partial\alpha$	lift derivative w.r.t. α	0.05 deg^{-1}
C_{D0}	zero lift drag	0.07
V	mean air speed	6 m/s
T	The tether's tension	3 N.m

Table III.3: Coefficients for the simulation study.

Our objective is to stabilize the system around a periodic orbit while controlling the attack angle only.
Starting from an arbitrary point $(\theta, r, \dot{\theta}, \dot{r})$ within the power region of the kite, the application of proposed virtual constraints-based control developed here gives the closed loop behavior of Fig.III.15. One can clearly see the effectiveness of the proposed feedback control. Several initial conditions have been tested and for all of them, the trajectories have stabilized on a periodic orbit in a short time. The speed of convergence depends on the gain of the feedback v control.

In figure III.16, the evolution of ξ, which is the state of the partial linear system (III.45), is presented. One can see the convergence of the integral I of equation (III.43). This means that system in closed loop is converging to the reference orbit.

In Fig.III.17 and Fig.III.18, respectively, the temporal evolution of the tether's length r and angle θ of the KGS and the applied controls are shown. Although these results may be improved through suitable choice of Γ and G, one can still see the effectiveness of the proposed control for this first approach.

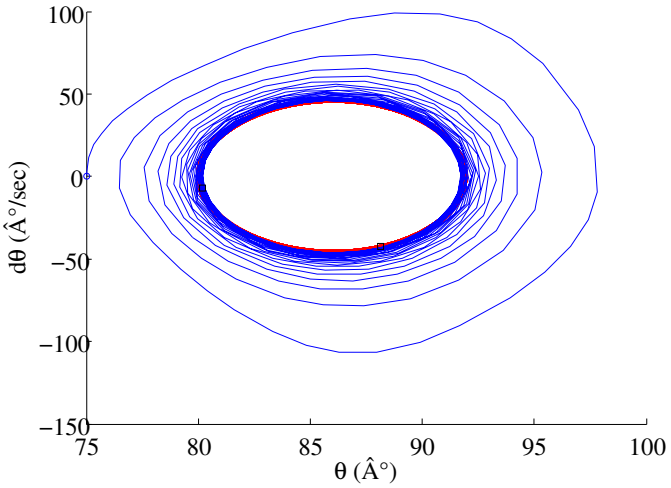

Figure III.15: The closed loop system's portrait.

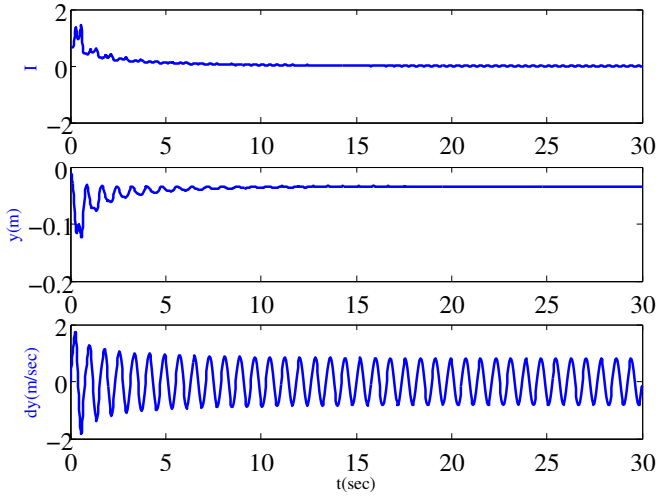

Figure III.16: The partial linear system closed loop evolution.

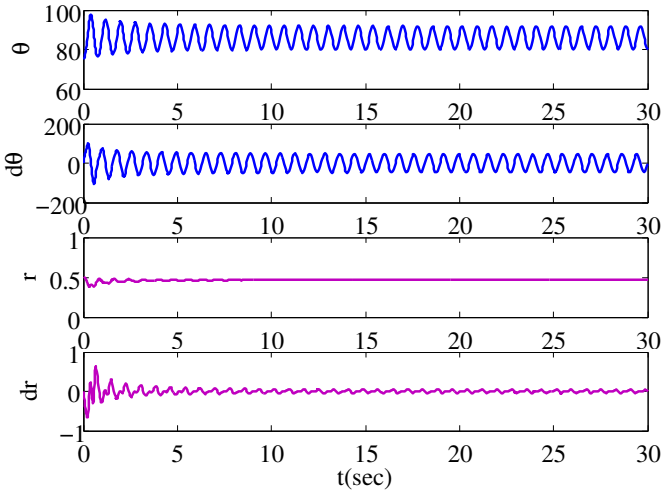

Figure III.17: Evolution of state variables $(\theta, \dot{\theta}, r, \dot{r})$ of the KGS.

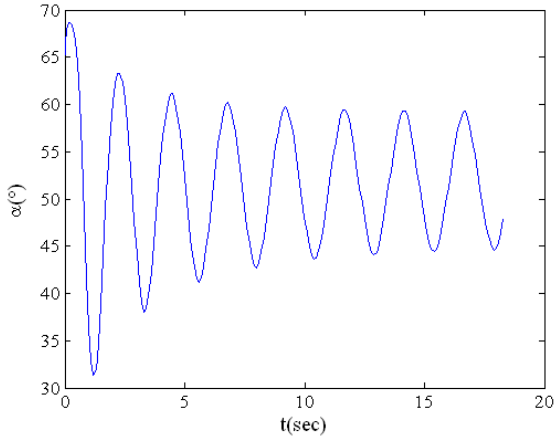

Figure III.18: The applied control for the studied KGS.

III.4 Conclusion

In this chapter, two methods to optimize and control the KGS were proposed and applied. The first strategy starts by defining a parametric orbit. The expression of the average generated power obtained following that orbit is written as a function of the radial velocity, and then maximized to find the optimal radial velocity and the orbit's period. Once the orbit is found, a nonlinear model predictive control is applied to insure the orbit tracking by controlling the kite's roll angle.

The second strategy used a novel method in the field: Virtual constraints (VC). The method aims at reducing the system's degrees of freedom by forcing virtual constraints between them. VC-based strategy was introduced and applied to a KGS moving in a pumping motion in 2D plane. The KGS has two degrees of freedom: A translation following the tether (r) and a rotation (inclination angle (θ)). It is controlled by the attack angle while the traction force determines the phase: Generation or recovery. By having one control input, the resulted system is an under-actuated Lagrangian system, and relations among the system's variables (virtual constraints) are enforced by feedback to get an overall closed-loop periodic system that converges fast to the pre-planned motion. This first study on applying virtual constraints on a kite-based system has shown promising results that worth being explored more.

Chapter IV

Kite Generator System: Grid Integration and Validation

Contents

Abstract

The KGS is built to be grid integrated or to supply an isolated load. The mechanical power generated by the kite's traction is translated into an electrical one via a permanent magnet synchronous machine (PMSM). This power is then injected in the grid or used to supply an isolated load after passing a power electronics interface that consists of two back to back three-phase voltage source converters: AC/DC and DC/AC.

Two control schemes are developed for the both of operation modes: grid connected or stand-alone. The first case consists in active and reactive currents injection, while the second case consists in voltage/frequency control in order to supply a given isolated load.

After assessing the proposed control strategy through simulations, experimental validation is addressed. It is decidedly important to take into account the dynamic behavior of the system which cannot be well observed through mere simulations, as well as to monitor the impact of the neglected amounts in simulation. This is achieved via testing on a Power Hardware-In-the-Loop simulator which is a real-time hybrid simulation system.

IV.1 Introduction

In the ongoing research to decarbonize the electric grid as soon as possible without losing its reliability, grid integration of renewable energy resources is an important issue. Energy resources can be generating a DC power as in the case of a photovoltaic cell or an AC one as in wind turbines and hydroelectric generators. It may, as well, require a bi-directional grid interface or an energy storage as in relaxation-cycle systems. On the other hand, the resource may be used to supply a strong infinite grid, an isolated micro grid, or a given isolated load. Therefore, different topologies are proposed and developed depending on the nature of the energy resource and the usage.

Both relaxation-cycle KGS and HPS, focused on in this thesis use a permanent magnet synchronous machine (PMSM) to translate the mechanic generated power to an electric one, then they require an AC/AC power electronics interface that insures a bi-directional power flow from/to the grid. In a stand-alone operation, this topology is reinforced by a storage unit because the system is not capable to supply the requested level of energy constantly, in addition to being a load itself during its recovery phase. The storage unit can be withdrawn by integrating more than one KGS or HPS to supply the same load. Herein, many solutions are proposed.

In the case of an infinite grid connection mode, the system is required to harness the maximum possible power from the primary source (the wind or the waves in our application) and inject it into the grid. For this purpose a maximum power point tracking algorithm is necessary, except here, there is not a maximum power *point* but a maximum power *cycle*.

In the case of a stand-alone operation, the goal is to achieve a certain level of power requested by the load, and the system's cycle is chosen and controlled according to this demand.

The proposed control strategies are tested through simulations and on a Power Hardware-In-the-Loop (PHIL) simulator.

The current chapter is divided into three main parts. Firstly, section.IV.2 is dealing with the power transformation unit, ie. the PMSM and the power electronics interface. Secondly, section.IV.3 proposes the control scheme used to drive the power transformation unit for each connection mode: Infinite grid-connected and stand-alone operation.

The third part of the chapter starts by introducing different real-time simulators briefly, then deals in more detail with the PHIL simulator in section.IV.4.b. In section.IV.4.c, the problem of implementing the KGS on the PHIL simulator is addressed and the experimental set up is presented. Finally, section.IV.4.d presents the simulations and the experimental results for the obtained models and control schemes.

IV.2 Power Transformation System

While a lot of research is being done to optimize the kite orientation control [NFM11] [BO11] [AHB12], the grid connection part is yet to be treated.

The kinetic power, captured from high altitude wind by the KGS, needs to be transformed into an electric one that can be injected in the electric grid or used to supply a certain load. For this purpose, a power transformation unit is needed.

Among the proposed power transformation systems associated to renewable energy grid integration, the one shown in Fig.IV.1 offers a suitable solution for the relaxation-cycle nature of the studied systems.

In the case of the KGS, the traction force of the kite is transformed into a torque applied on a permanent-magnets synchronous machine (PMSM) situated on the ground. This leads to producing

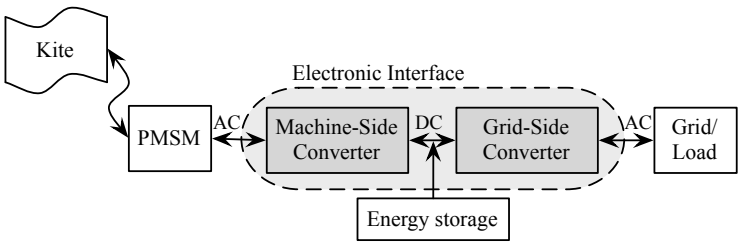

Figure IV.1: Kite Generator System Block diagram.

an alternative electrical energy with variable frequency. The machine is coupled with the grid/load, through a power electronics interface that consists of two bidirectional AC/DC converters. An energy storage should be integrated in the case of a load or an isolated grid connection, in order to provide the necessary energy during the system's recovery phase. It is installed on the DC-bus level relating the converters. The power transformation system is presented and modeled in the coming paragraphs.

IV.2.a Torque Transmission between the Kite and the PMSM

The translation movement of the tether is transformed to a rotation by means of a drum coupled to the PMSM through a gearbox. Thus, the traction force F_{trac} is translated to a torque C_R applied on the machine. Torque transmission is expressed by the fundamental mechanical equation of eq.IV.1 and Fig.IV.2.

$$C_G - C_R - D\Omega_S = J\frac{d\Omega_S}{dt} \tag{IV.1}$$

where:

- $\Omega_S = \frac{V_L}{K}$ is the rotation velocity, with K combining the gearbox factor and the drum diameter R.
- J is the total inertia of the kite, the drum; and the machine's rotor.
- C_G is the generator torque.
- D is the damping factor estimation.

and the transmission chain elasticity is neglected. Eq.IV.1 shows that in order to control the rotation velocity, a generator torque control should be applied, and vice-versa.

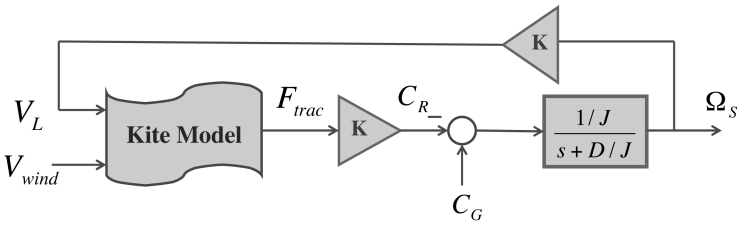

Figure IV.2: Modeling of the mechanic connection between the kite and the electrical machine.

IV.2.b The PMSM's Vector Model

Each machine's phase can be presented by the Behn-Eschenburg equivalent electric model of Fig.IV.3, which consists of a resistance R_s, inductance L_s and an electromagnetic force e_{sk} : $k = a, b, c$. The model supposes the existence of a regular air gap, linear characteristics of the

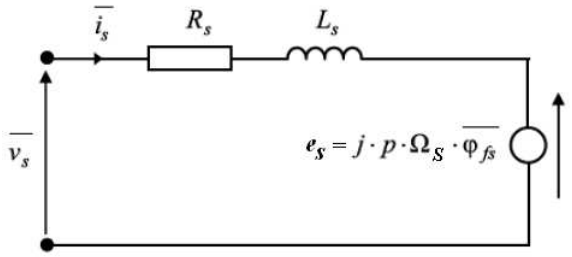

Figure IV.3: PMSM's Behn-Eschenburg equivalent electrical model.

magnetic circuit (no saturation), and a balanced sinusoidal three-phase current behavior.

To visualize the three phases at the same time, variables' vector presentation is used, and is expressed in Park frame (p, q) by

$$\begin{array}{lcl} v_{sd} & = & R_s i_{sd} + L_s \frac{di_{sd}}{dt} - \omega L_s i_{sq} \\ v_{sq} & = & R_s i_{sq} + L_s \frac{di_{sq}}{dt} + \omega L_s i_{sd} + \omega \phi_{fsd} \\ \phi_{sd} & = & L_s i_{sd} + \phi_{fsd} \\ \phi_{sq} & = & L_s i_{sq} \\ C_G & = & p \phi_{fsd} i_{sq} \end{array} \tag{IV.2}$$

where

- $\bar{v_s} = v_{sd} + j.v_{sq}$ is stator voltages' vector.
- $\bar{i_s} = i_{sd} + j.i_{sq}$ is stator currents' vector.
- $\bar{\phi_{fs}} = \phi_{fsd} + j.\phi_{fsq}$ is the induced flow vector.
- p is the number of poles' pairs.
- $\omega = p\Omega_s$ is the electric pulsation.

IV.2.c Power Electronics Interface

The power electronics interface ensures frequency and voltage isolation between the PMSM and the electric grid or the connected loads, and at the same time it offers the possibility of power flow from/to the PMSM. This interface is made up of two converters AC/DC & DC/AC (Fig.IV.4,Fig.IV.5) [MBB10] that convert the variable frequency/voltage electric power generated by the PMSM, into a standard frequency/voltage electric power that agrees with the grid codes. A filtering stage precede the the connection and depends on its type. In Fig.IV.5, a filter L is used to connect the system to an infinite electric grid.

The converters are controlled using vector pulse width modulation (PWM). Both converters function as a rectifier and an inverter depending on the system's phase (Generation or recovery), insuring a bi-directional transfer of energy.

For the machine-side converter, supposing that the switches and voltage sources are perfect and the passive elements are linear and constant, Park representation of the converter's average model is written in eq.IV.3:

$$\begin{array}{lcl} L_s \frac{di_{sd}}{dt} & = & \beta_{sd} \frac{U_{DC}}{2} + \omega L_q i_{sq} - R_s i_{sd} \\ L_s \frac{di_{sq}}{dt} & = & \beta_{sq} \frac{U_{DC}}{2} - \omega L_d i_{sd} - R_s i_{sq} - e_{sq} \\ C_{DC} \frac{dU_{DC}}{dt} & = & -I_{DC} + (\beta_{sd} \frac{i_{sd}}{2} + \beta_{sq} \frac{i_{sq}}{2}) \end{array} \tag{IV.3}$$

where U_{DC} and I_{DC} are the DC bus voltage and current respectively.

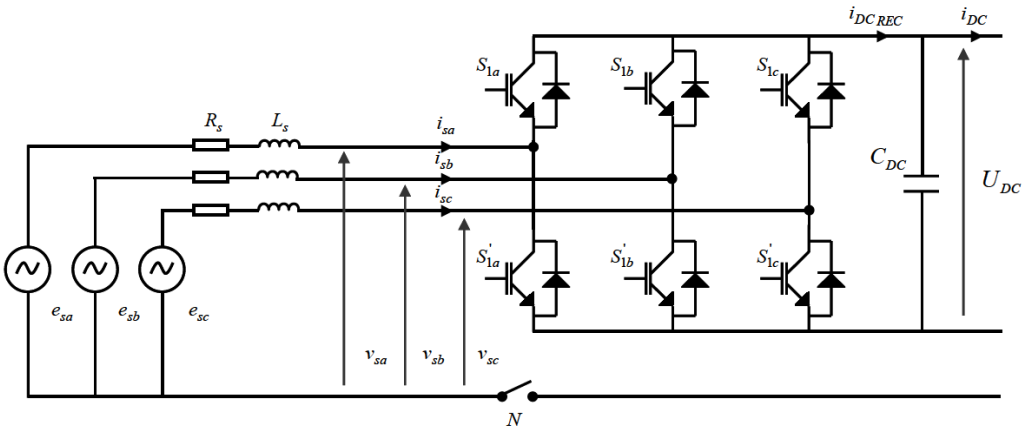

Figure IV.4: Electric representation of the PMSM-side converter. PMSM is presented by Behn-Eschenburg model. C_{dc} is DC-bus filtering capacitor.

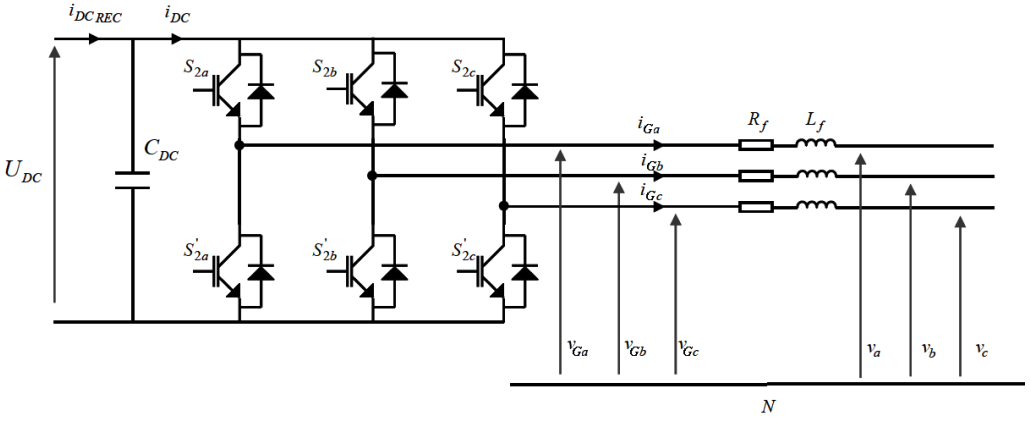

Figure IV.5: Electric representation of the Grid-side converter. R_f and L_f represent loss and filtering components.

The same modeling approach is applied for the grid-side converter (Fig.IV.5):

$$\begin{array}{lcl} L_f \frac{di_{Gd}}{dt} & = & -\beta_{Gd}\frac{U_{DC}}{2} + \omega_G L_f i_{Gq} - R_f i_{Gd} + \sqrt{3}V_G \\ L_f \frac{di_{Gq}}{dt} & = & -\beta_{Gq}\frac{U_{DC}}{2} + \omega_G L_f i_{Gd} - R_f i_{Gq} \\ C_{DC}\frac{dU_{DC}}{dt} & = & I_{DC_{REC}} - (\beta_{Gd}\frac{i_{Gd}}{2} + \beta_{Gq}\frac{i_{Gq}}{2}) \end{array} \quad \text{(IV.4)}$$

where:

- ω_G is the electric grid pulsation.
- V_G is the grid RMS voltage.
- $\bar{i_G} = i_{Gd} + i_{Gq}$ is the grid currents' vector.
- $I_{DC_{REC}}$ is the machine converter output current.
- β_{Gd}, β_{Gq} are the average vector PWM duty cycles.

As noticed, an average model is adapted in order to have a continuous time model without switching, which allows the usage of relatively large sampling time in simulations.

IV.3 Control Scheme

The control scheme is designed to insure:

- the tether radial velocity control to generate the desired average power taking into account wind speed variations,
- and the electronics power interface electrical variables control.

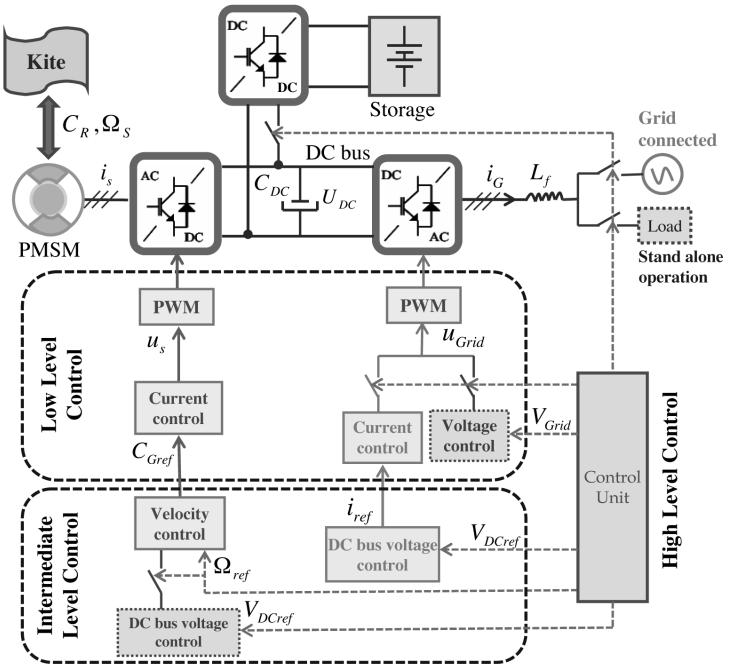

Figure IV.6: General control scheme of the KGS power transformation system. Two control tracks applied depending whether the system is grid connected or in a stand-alone operation.

Fig.IV.6 shows the general control scheme of the power transformation system. The control scheme is divided into three levels: Low, intermediate and high. Each level functions in accordance with the system operation status: Grid-connected or stand-alone operation. Both are presented and discussed in the following paragraphs.

IV.3.a Grid-connected operation

When the KGS is connected to an infinite electric grid, the control strategy aims at harnessing the maximum available energy and injects it in the grid. Meanwhile the grid is responsible of supplying the necessary energy during the system's recovery phase.

For this purpose the machine-side converter is driven to control the machine rotation velocity, and the grid-side converter controls the DC-bus voltage and maintains the injected currents in phase with the grid voltages in order to preserve grid reliability.

IV.3.a-i Low Level Control

The low level control concerns the converters switches control. It translates higher level control laws into pulse width modulation PWM commutation rates that command the converter's switches. This conversion is done via control of the converters' output currents or voltages according to the converter operation. In the case of infinite grid connection, both are current controlled.

The **machine-side converter** controls the generator torque C_G via its current. Considering a PMSM and taking into account that the machine and its converter are working within their nominal limits; controlling C_G is equivalent to controlling the current i_{sq} with asserting $i_{sd} = 0$ (See eq.IV.2). This allows having a maximum torque per ampere (MTPA).

To control the currents, a PI controller acting in the $p-q$ rotating frame is used. It is simple yet efficient for this control problem [BBM13][MBBR10]. The transfer function of such a controller takes the form:

$$H_{c-im}(p) = K_p + \frac{K_i}{p} = K_p(1 + \frac{1}{T_i p}) \tag{IV.5}$$

with $T_i = K_p/K_i$, where: K_p, K_i are, respectively, the corrector proportional and integral gains. These parameters are chosen to let the current loop response time much faster than that of higher control loops, as well as, a limited overshoot that does not exceed the converters maximum currents.

Fig.IV.7 shows the proposed control scheme in this case based on the converter's model given by eq.IV.3, and with: $E = p\Omega\Phi_{fsd}$. The control is done numerically in the $p-q$ space and a vector PWM is built and transmitted to the $a-b-c$ space to drive the switch.

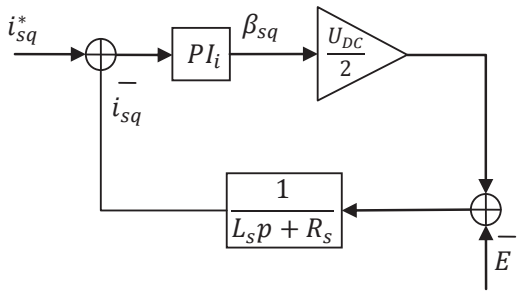

Figure IV.7: Low level control scheme for the machine-side converter.

The **grid-side converter**'s currents must be in phase with the grid voltages and have a low harmonic distortion (THD). They are controlled in the fixed coordinates $a-b-c$ via a resonant PI controller that acts on the current harmonies desired to be eliminated [dHAEO06].

Such a controller take the following form:

$$H_{c-ig}(p) = K_p + \sum_{n=1}^{h} \frac{2K_i p}{p^2 + \omega_n^2} \tag{IV.6}$$

where the proportional gain K_p which affects all the current harmonies equally, and the integral part K_i affects the h harmonies specified by their resonant pulse ω_n.

From Fig.IV.5, the grid-side converter current control scheme is shown in Fig.IV.8.

IV.3.a-ii Intermediate Level Control

The intermediate level control loops generate the reference signals needed for the currents control in the lower level via control of the PMSM rotation velocity and the DC-bus voltage.

The rotation velocity is controlled by the **Machine-side Converter** using a classic PI controller of the same form as that of eq.IV.5. It generates, according to the mechanical equation (eq.IV.1), the generator torque reference, hence i^*_{sq}.

Considering the current inner loop is much faster than that of the velocity, the resulted transfer

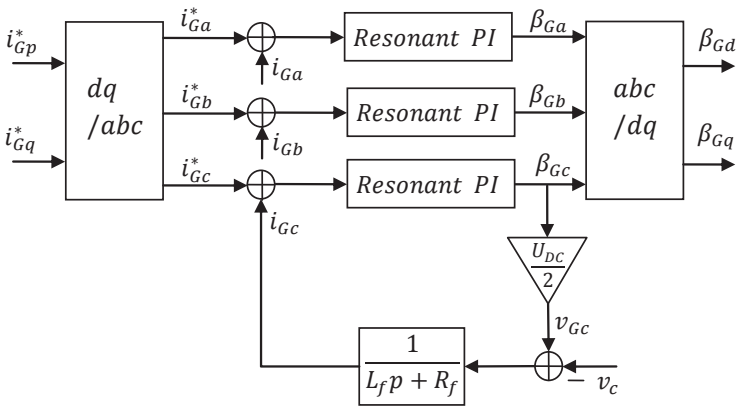

Figure IV.8: Low level control scheme for the grid-side converter.

function is a second degree one from which the parameters of the PI corrector are determined. This is done by choosing a suitable time response that is much smaller than the KGS cycle period, and a suitable overshoot. Fig.IV.9 shows the rotation velocity control loop, where $K_E = K_G = p\Phi_{fsd}$

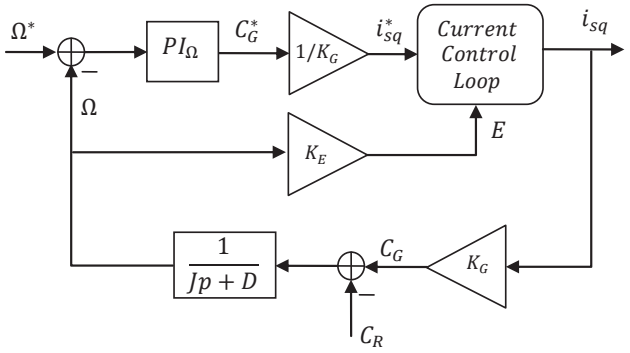

Figure IV.9: Intermediate level control scheme for the machine-side converter: Machine velocity control.

The **grid-side converter** converts the direct power to a fixed-frequency alternative power, or vice versa, according to the KGS phase (Traction/Recovery), hence, it is driven to control the DC-bus voltage.

The DC-bus is assumed to have a resistance R_{DC} and a capacitor C_{DC}, and once again a vector PI controller is used to generate the i^*_{Gq}. Fig.IV.10 shows the DC-bus voltage resulted loop.

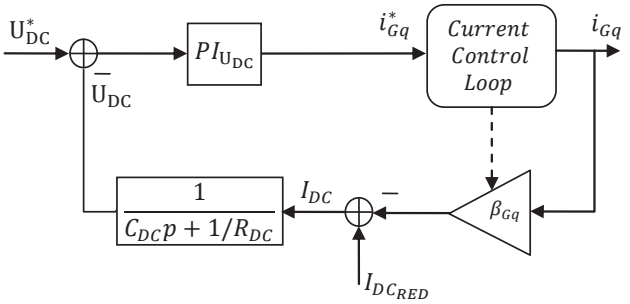

Figure IV.10: Intermediate level control scheme for the grid-side converter: DC-bus voltage control.

IV.3.a-iii High Level Control

In addition to generating the needed reference signals of the lower control levels, the high level control supervises the functioning of the system by controlling the switches that determine the power flow through it.

As observed in lower control layers, the PMSM's rotational velocity control and the generator torque control are guaranteed by the PMSM-side converter. The kite applies a resistive torque C_R that gives, when inserted in the mechanical equation, the rotation velocity Ω_S. The velocity is corrected using a PI controller that yields a reference generator torque C_{Gref}. The reference rotation velocity is obtained by applying a maximum power "cycle" tracking (MPCT) algorithm that seeks the kite trajectory that guarantees a maximum average generated power.

IV.3.a-iv Maximum Power Cycle Tracking

In the KGS, the optimal trajectory of the kite is a function of the wind speed and direction. In a certain direction, the optimal radial velocity changes its amplitude and period depending on the wind speed. Fig.IV.11 exhibits this dependence.

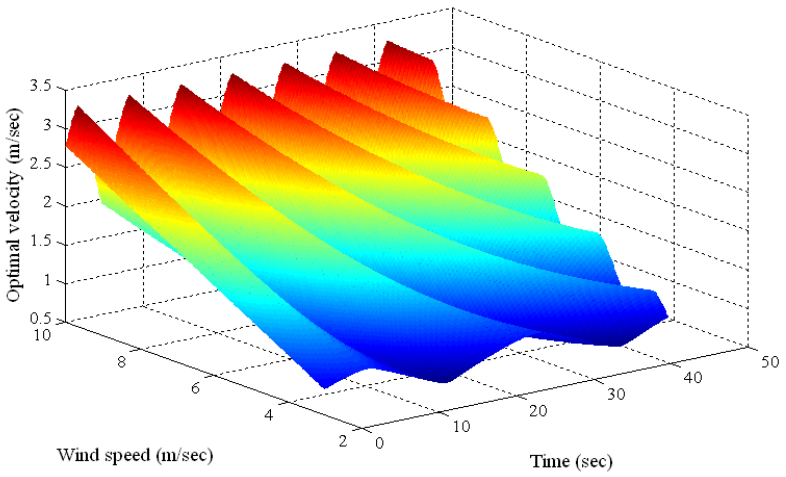

Figure IV.11: Optimal radial velocity as a function to time and wind speed.

In fact, the optimization algorithm proposed in sec.III.2.a-ii starts from a parametric orbit and finds the profile of the optimized normalized radial velocity, that is $\hat{v}(t)$, whose period T_n is also normalized. This result depends on the direction of wind only and the radial velocity profile is next found by:

$$\hat{V}_L = \hat{v} * V \tag{IV.7}$$

$$T = T_n/V \tag{IV.8}$$

with V being the wind speed.

The proposed algorithm is a simple "Disturb & Observe" algorithm, whose objective is to find the multiplier V that should be applied on the normalized radial velocity profile $\hat{v}(t)$ to find the optimal radial velocity$\hat{V}_L(t)$.

In the case of absence of wind speed measurement, the optimal radial velocity can be calculated according to standard wind-altitude curves, while the MPCT algorithm acts on the rotation velocity amplitude and period to find the optimal profile. The algorithm begins by applying one period of the optimal radial corresponding to wind speed estimation. Then it calculates the average power

during this period, and compares it later with the average power obtained after changing the multiplier V during the next period.

Choosing to maximize the power on the whole cycle aims at ignoring fast short changes in wind speed The algorithm is effective to deal with slow changes in wind speed compared to the orbit's period, which is usually valid for high altitude winds. Finally, the KGS complete proposed control scheme can be summarized in Fig.IV.12.

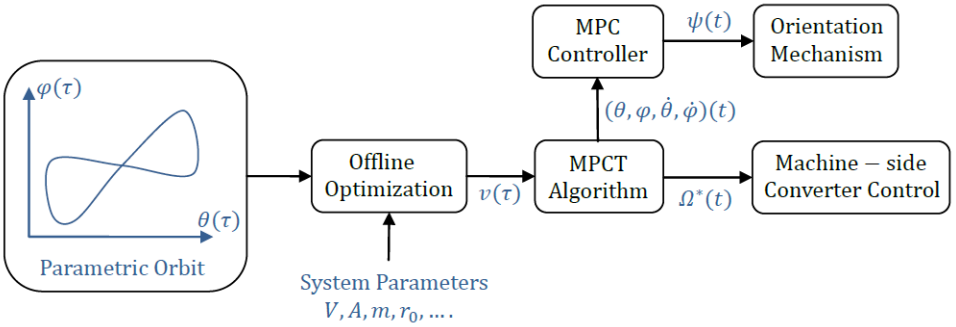

Figure IV.12: Inserting the MPCT algorithm in the NMPC-based proposed control strategy.

IV.3.b Stand-alone Operation

In a stand-alone operation, the KGS cannot insure a continuous deliverance of power to the connected load or isolated grid without the support of a storage unit or other energy resources.

The second option can be achieved by supplying the load by more than one KGS whose orbits are suitably chosen in order to smooth the output power. For instance, Fig.IV.13 shows the output power profile resulting from using 4 kites flying in $T/4$ delay one from another and with a rotation 90°.

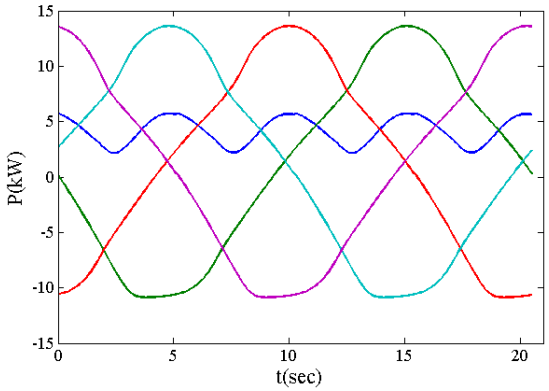

Figure IV.13: Average output power of a 4-kite-based system.

Different kite generator systems are connected on the DC-bus level and share the same DC/AC inverter to connect the load or the micro grid. In fact, this is equivalent to considering a single KGS supported by a storage unit presented by other KGSs.

The control levels vary slightly since the goal becomes generating the needed power for the load. The load-connected converter's output voltages are controlled to have a constant amplitude and

frequency. As a result, the machine-side converter(s) is (are) driven to control the DC-bus voltage, while the grid-side converter controls the AC output voltage.

On the low control level, the machine-side converter is driven by currents as in the grid-connected operation case. Meanwhile, the load-side converter is controlled by voltages.

By adding an LC filter on the load-connected inverter, the converter and the load can be presented by the transfer function:

$$G(p) = \frac{1}{p^2 + (\frac{1}{RC_f} + \frac{R_f}{L_f})p + \frac{1}{L_f C_f}(1 + \frac{R_f}{R})} \tag{IV.9}$$

where the load is supposed to be resistive only R and R_f, L_f, C_f are the filter components.

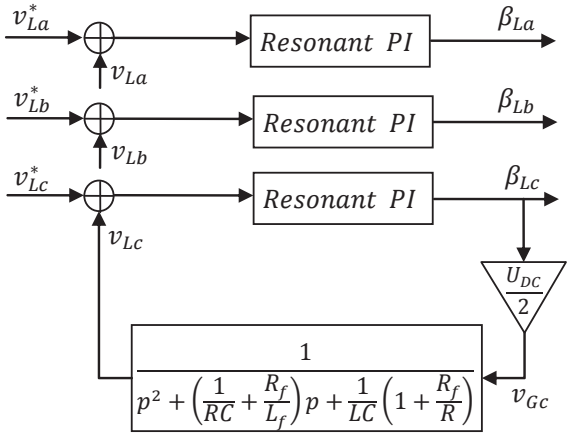

Figure IV.14: Load-connected converter low level control scheme.

In the intermediate control level, as in the case of grid connection, the machine-side converter controls the machine velocity, but via the DC-bus voltage control layer. The control scheme, shown in Fig.IV.15, results from eq.IV.2 and uses a PI corrector to regulate the DC-bus.

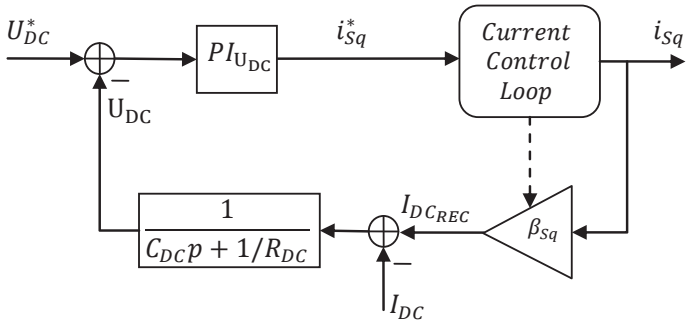

Figure IV.15: Machine-connected converter Intermediate level control scheme.

The high level control determines the sinusoidal $50Hz$-frequency voltage reference for the load voltage loop and the DC-bus reference voltage.

IV.4 KGS Control Validation

The KGS model and control strategies will be tested through non-real time simulations. A following step will be to validate those experimentally. This is done usually via prototyping. Nevertheless,

another direction is taken here, that is Power Hard-Ware-In-the-Loop (PHIL) simulation.

For this purpose, an experimental bench built in G2Elab is put to service. It is a real-time hybrid simulator that consists the following main parts:

- A direct current machine (DCM).
- A permanent magnets synchronous machine (PMSM).
- A power electronics interface consisting of two converters (DC/AC, AC/DC) connected to a grid emulator.
- A real-time digital simulators: RT-lab and dSPACE that support and drive the previous parts.

In this simulator, the tethered kite behavior and its associated drum and gearbox are emulated by a direct current machine (DCM), while the rest of the system is physically present. The hardware is interfaced with the real-time simulator on which the optimization and the control strategy in addition to the kite model are implemented.

Employing the PHIL-simulator instead of building a prototype is justified because the tests carried on here focuses on the grid integration aspect, and produced power maximization via control of the power conversion chain, and not on the kite orientation control. Furthermore, PHIL simulator has many advantages over the usage of a complete hardware prototype, it requires less material and human investments, it can be modified easily to test different control strategies, and allows experimenting different test conditions in the laboratory environment.

IV.4.a Real-time Hybrid Simulation Systems

A simulator is described to be real-time if its subsystems are able to communicate with each other efficiently. Real-time simulators are classified in three main groups: Analog, digital and hybrid. An analog simulator is composed of physically reproduced models or a reduction of the simulated system's components. A real-time digital simulator is similar to a non-real-time one, except for its calculation step, which is fixed and sufficiently long to allow the systems components to perform required operations or calculations within it.

The real-time analog simulator can be described as a reduced prototype, and it is specially useful to predict the dynamic behavior of the system and to test its regulators and sensors. On the other hand, it is costly and complex to reconfigured. These negative points are completely overcome in a real-time digital simulator, but still an analog simulator is superior when simulating complex-model components with high cut-off frequencies.

A compromise or a combination of both is the hybrid real-time simulator. Such a simulator consists of two parts, a hardware containing the complex components of the system, usually the power ones, and a software part containing other components models and the control algorithms. Both parts are communicating with each other efficiently, meaning the software of the system is running on a fixed time step bigger the response time of the hardware.

An example of the hybrid simulator is the hardware-in-the-loop presented in the next section and used later to validate the KGS.

IV.4.b Power Hardware In the Loop Simulator

The PHIL simulator is a semi-hardware semi-software system, in which measurements and control signals are exchanged between the hardware and the software. This technique of testing allows studying and validating energy management strategies while preserving the flexibility to modify

the control and the test conditions. It is widely employed in aviation and automobile industries due to its important advantages:

- The possibility to simulate as many energy management strategies and architectures of control as desired with minimal intervention.
- Reduced cost compared to the tests on actual system.
- Facility and safety of application.
- Nondestructive test.

A PHIL simulator was built in G2Elab. It was conceived during a few PhDs' and masters' projects [GEOBR06] [MBAB10] [ABR08]. Originally built to test the control strategies of wind and water turbines [BBM13] [OGBR08] [MBBR10] [MBBG07] [ABR08], it was later implemented to test Photovoltaics [CFBM10] [GRBB11], electric vehicle traction chain [FTBV11] [FBMB12], and others [AMCR14].

The hardware or physical part of the invested HIL-based simulator, presented in Fig.IV.16, is composed of a direct current machine (DCM) controlled to emulate the behavior of the primary energy source or load; and a PMSM coupled mechanically to the DCM and connected through two transistor-based converters with either an emulated infinite electric grid, or with a load. The software part contains the controllers and the model of the energy source.

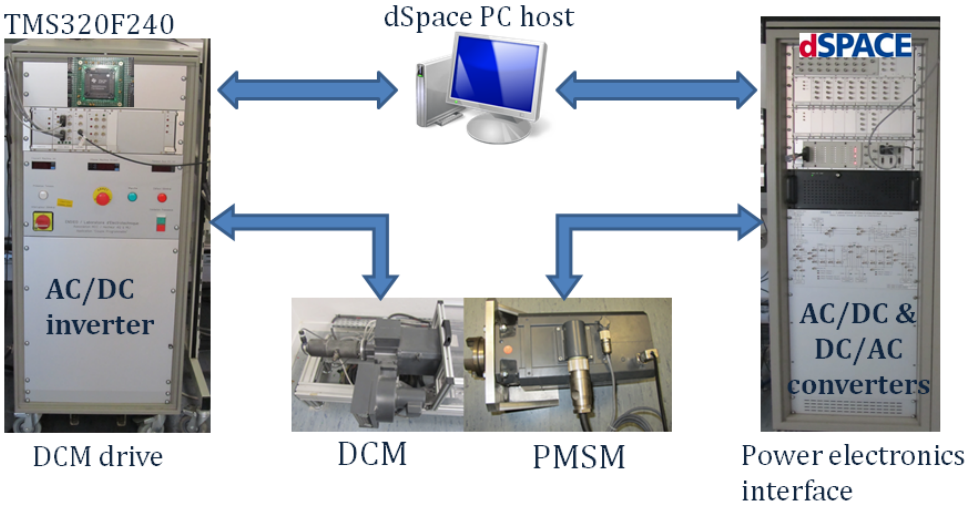

Figure IV.16: PHIL Simulator

IV.4.c KGS Implementation on the PHIL Simulator

Simulation of the KGS using a software simulator is an important step to initially verify the performance of the proposed control strategy. An intermediate step before testing on a real prototype, is the test on the PHIL simulator. The simulator allows replication of the dynamic behavior of the real system with the possibility of controlling the working conditions in the laboratory [MBAB10] [And09].

The KGS power transformation unit is physically presented in the PHIL-simulator while the DC-machine replicate the behavior of the tethered kite.

IV.4.c-i KGS Scaling

The real-time PHIL experimental bench in G2ELAB was not built for a single test set-up. Therefor, in order to employ the bench to test the dynamics of the KGS, a scaling stage is needed.

The bench is characterized by:

- Maximum power $P_{bmax} = 3kW$
- Maximum rotation velocity $\Omega_{bmax} = 314rad/s$
- Maximum torque $C_{bmax} = 20Nm$

The KGS parameters need to be chosen to adapt to these values, and a scaling factor is needed to be applied before inserting those in the experimental bench. Scaling the rotation velocity and the torque is expressed by:

$$\begin{array}{rcl} C_{bmax} & = & nC_{max} \\ \Omega_{bmax} & = & \frac{\Omega_{max}}{m} \end{array} \tag{IV.10}$$

Accordingly, the power scaling equation:

$$P_{bmax} = C_{bmax}\Omega_{bmax} = \frac{n}{m}C_{max}\Omega_{max} = \frac{n}{m}P_{max} \tag{IV.11}$$

Notice that $n \neq m$ necessarily since the objective of the proposed real-time simulation is to test the dynamic behavior of the system and insure the functioning of the control strategy. However, the scaling factors are chosen to be the same in order to observe the delivered power losses.

IV.4.c-ii KGS Torque Emulation

The experimental bench direct current machine is controlled to follow the dynamics of the KGS. As seen in section.IV.2.a, the mechanic connection between the tethered kite and the PMSM is expressed by the equation:

$$C_G - C_R - D\Omega_s = J\frac{d\Omega_s}{dt} \tag{IV.12}$$

with C_R being the kite torque and Ω_s the machine rotation velocity. Replacing the kite by the DCM results in the mechanic equation eq.IV.13

$$C_G - C_{DCM} - D_E\Omega_E = J_E\frac{d\Omega_E}{dt} \tag{IV.13}$$

where:

- C_{DCM} is the DCM torque.
- D_E is the damping factor estimation between the DCM and the PMSM and it is a function of the rotation velocity Ω_E.
- J_E is the total inertia of the DCM and the PMSM.

Fig.IV.17 represents the mechanic connection for both mentioned cases.

Comparing eq.IV.12 and eq.IV.13 yields that: in order to replicate the KGS behavior by the DCM, the Ω_E's dynamics have to follow that of Ω_s and the DCM torque needs to be controlled to follow the reference in eq.IV.14. The resulted mechanic connection is represented in Fig.IV.18

$$C^*_{DCM} = C_R + (J - J_E)\frac{d\Omega_s}{dt} + (D_E - D)\Omega_s \tag{IV.14}$$

Hence, the DCM torque reference consists of two parts, the tethered kite traction torque and a correction torque:

$$C_{cor} = (J - J_E)\frac{d\Omega_s}{dt} + (D_E - D)\Omega_s$$

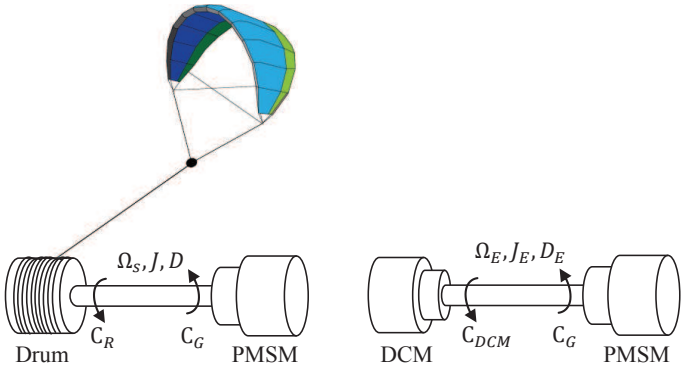

Figure IV.17: Representation of the Mechanic connection in the case of the KGS and the DCM.

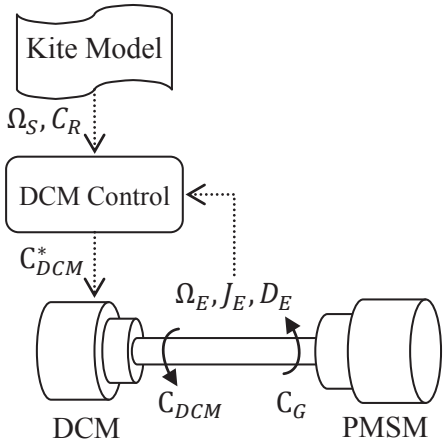

Figure IV.18: KGS replication using the DCM.

However, computing C_{cor} is an issue in real-time applications since the rotation velocity gradient calculation induces noise, and determining the damping friction values is very difficult since they are functions of the rotation velocity [MBAB10].

In order to overcome these negative points, in [MBAB10] the authors modify the mentioned method by using the correction component C_{cor} to control the DCM rotation velocity to track that of the KGS drum. Applying that to the KGS results in the control block diagram presented in Fig.IV.19.

Notice that, once velocity tracking is insured, C_{cor} becomes constant which leaves the dynamics of C_R only.

A PI controller is used to insure tracking of the KGS rotation velocity [mun]. The controller has the general form:

$$H_{PI} = K_P + \frac{K_I}{p}$$

The open-loop transfer function of the DCM rotation velocity according to the reference velocity is expressed as follows:

$$\frac{\Omega_E(p)}{\Omega_S(p)} = \frac{J_E(K_P p + K_I)}{(J_E p + D_E)p}$$

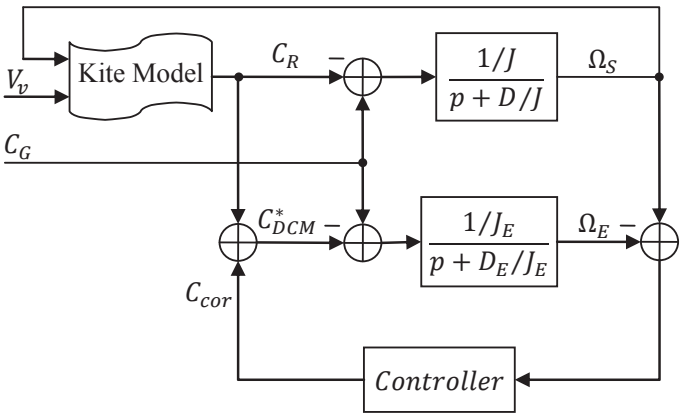

Figure IV.19: KGS replication using the DCM.

Thus, the resulting closed-loop function is given in eq.IV.15.

$$H_{cl} = \frac{\tau_{PI}p + 1}{\frac{p^2}{\omega_n^2} + \frac{2\xi}{\omega_n}p + 1} \tag{IV.15}$$

Where:

$$\begin{aligned} \tau_{PI} &= \frac{K_P}{K_I} \\ \omega_n &= \sqrt{K_I} \\ \xi &= \frac{1}{2\sqrt{K_I}}\left(\frac{D_E}{J_E} + K_P\right) \end{aligned}$$

The corrector parameters are calculated according to the desired response, e.g. response time and overshoot, determined by ξ, ω_n. The weak point of this corrector is that its parameters are dependent of the friction coefficient D_E which is a function of the rotation velocity.

IV.4.c-iii Experimental Set-up

As mentioned earlier, the PHIL simulator is a hybrid semi-hardware semi-software one, in which the hardware part contains the electrical machines and the converters, while the software includes the control of those as well as tethered kite model. The KGS test bench control scheme is shown in Fig.IV.21. The KGS parameters, the KGS orbit optimization (section.III.2.a-ii), the kite model (section.II.2.b) as well as the MPCT algorithm (section.IV.3.a-iv) are implemented on Matlab/Simulink. The simulink model has two outputs: The traction torque and the rotation velocity reference; and two inputs: The measured velocity and power.

The simulink model communicate with RT-lab via a TCP/IP protocol functioning under Labview environment who play the role of a server for both. Here, the digital real-time simulator RT-lab provide a transparent interface with dSPACE.

Using Labview to communicate data between Matlab/Simulink and RT-lab, avoids the necessity to modify the structures of already built and tested functionality on Simulink[1].

On dSPACE, the torque emulator controller (section.IV.4.c-ii) generates the DCM torque reference and send it to the digital signal processor $DSPTMS320F240$ card that controls the DCM chopper. Meanwhile the control of the PMSM and the power electronics interface is performed on dSPACE. Fig.IV.21 shows an abstract scheme of the test bench control. Measurements of the rotation velocity, the generator torque and the DCM torque feed back the controllers.

[1] RT-lab may show errors related to using .m functions and some other Matlab/Simulink blocks

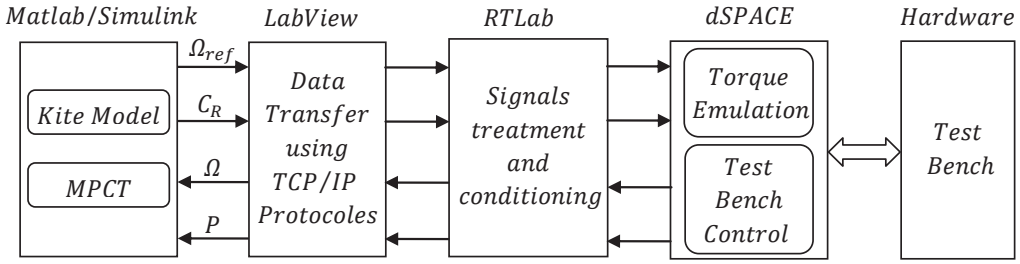

Figure IV.20: KGS real-time test platform scheme.

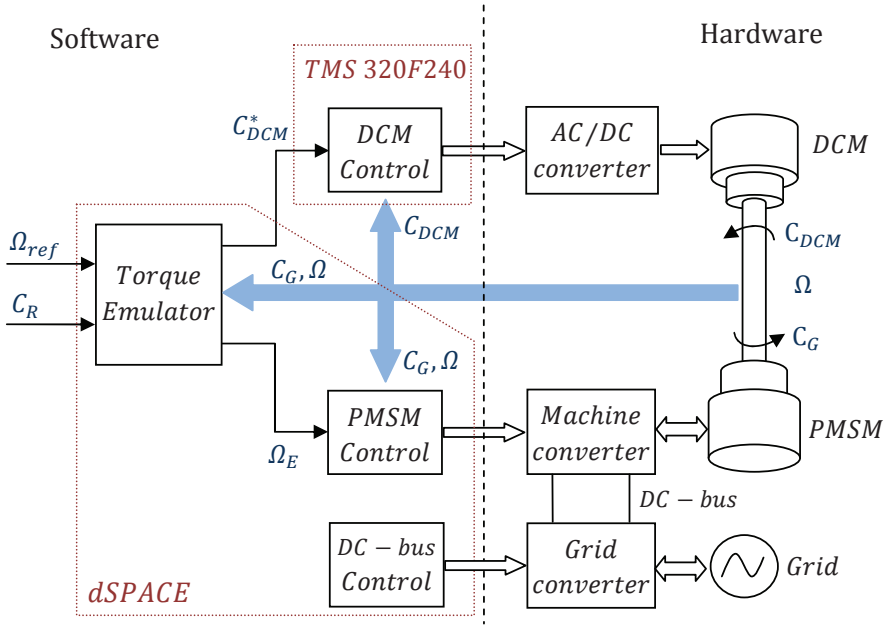

Figure IV.21: KGS test bench control scheme.

IV.4.d Validation

In this section the proposed control schemes are tested via simulation and on a PHIL simulator.

The KGS's parameters shown in Table.IV.1 are chosen in order to generate a radial velocity and traction torque that respect the limits imposed by the PHIL simulator [MBAB10]. The testing orbit is defined by the parametric equations (eq.IV.16) with a rotation 90^o and $\tau \in [0, 2\pi]$.

$$\theta(\tau) = 55^o + 10^o sin(2\tau), \ \phi(\tau) = 15^o sin(\tau) \tag{IV.16}$$

Note that the orbit initial inclination is 55^o which does not agree with the condition that let the assumption 'The tether is straight and inelastic" true (See Sec.II.2.b). But, with a tether's crosswind area much smaller than the kite surface, according to II.12, the tether's drag force can be neglected in front of the kite traction force, so the previous assumption applies here.

Applying the optimization algorithm proposed in section.III.2.a-ii results in the optimal tether radial velocity shown in Fig.IV.22 with a period $T = 20.6sec$.

An optimal control that minimizes the cost function of eq.III.18 is applied to find the roll angle needed for the kite to track the optimal orbit. The resulted trajectory is shown on Fig.IV.23.

Table IV.1: Kite Generator System Parameters

K	414	Gearbox factor * rotor diameter R (m)
V	4	Wind speed (m/sec)
Ω_{max}	210	Maximum rotation velocity (rd/sec)
Γ_{max}	30	Motor maximum torque (N.m)
p	4	Pole's pairs number
A, m	5, 3	Kite's area(m^2) and mass(Kg)
ρ_a	1.2	Air density (kg/m^3)
C_L	1.2	Lift coefficient
C_D	0.08	Drag coefficient
r_0	600	Initial tether length (m)

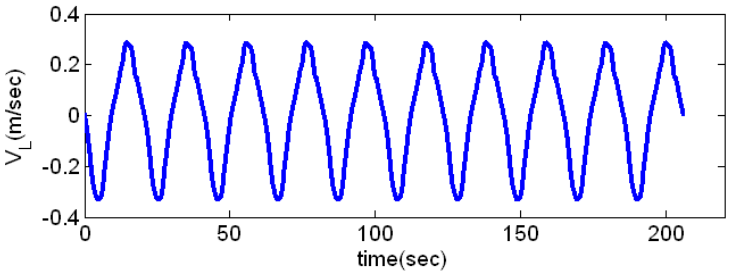

Figure IV.22: Optimal normalized radial velocity.

The tether's optimized radial velocity V_L as well as the traction force F^{trac} obtained from the kite model are transformed into a rotation velocity Ω_S and a torque C_R applied to the rotor (see Fig.IV.2). The transformation is done through a drum coupled to the PMSM through a gearbox. The simplest representation of this transformation is a multiplication by a constant as in the following equations:

$$\Omega_S = V_L K, \; C_R = \frac{F^{trac}}{K} \tag{IV.17}$$

In this case, the product factor K is found to be 414 in order to adapt to the PHIL simulator's PMSM. The obtained velocity and torque are then applied on the Matlab/Simulink model of the power transformation system .

The MPCT algorithm acts, as explained in section IV.3.a-iv, on the amplitude of the optimal radial velocity to follow slow changes of wind speed. To test the functioning of the MPCT algorithm, the wind speed is changed from $4m/sec$ to $5m/sec$. Fig.IV.24 shows the modification of the velocity amplitude because of the MPCT algorithm, and the resulted resistive torque; and finally the development of the average power per period. The maximum power cycle (MPC) is seemed to be tracked in 3 times the orbit period which is about $60sec$. The simulation shows that the estimated average produced power of the system, described in Table.IV.1, at a wind speed $5m/sec$ is $400W$.

The next step is to transform the mechanical power produced by the PMSM into an electrical power that can be injected into the grid. This can be insured by tuning different control levels paremeters presented in the general control scheme (Fig.IV.6). Remember that classical PID regulators are used to control the velocity and the currents of the machine-side converter, while for the grid-side converter's currents a resonant PID is implemented.

Figs.IV.25 shows the machine phase current I_{aS} and the DC bus U_{DC} voltage during one period of the rotation velocity Ω_S. It can be noticed that U_{DC} is well controlled with an error less than 0.9%.

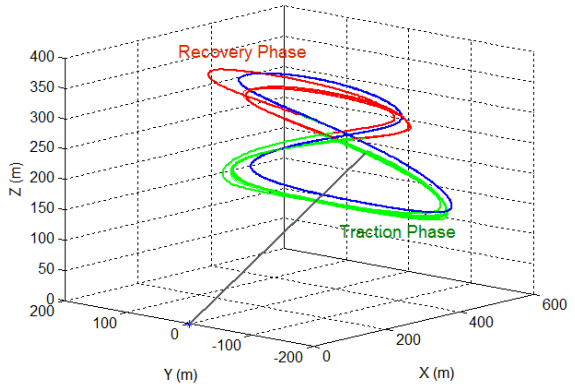

Figure IV.23: Orbit Tracking using optimal predictive control. In green: Traction phase, in red: Recovery phase.

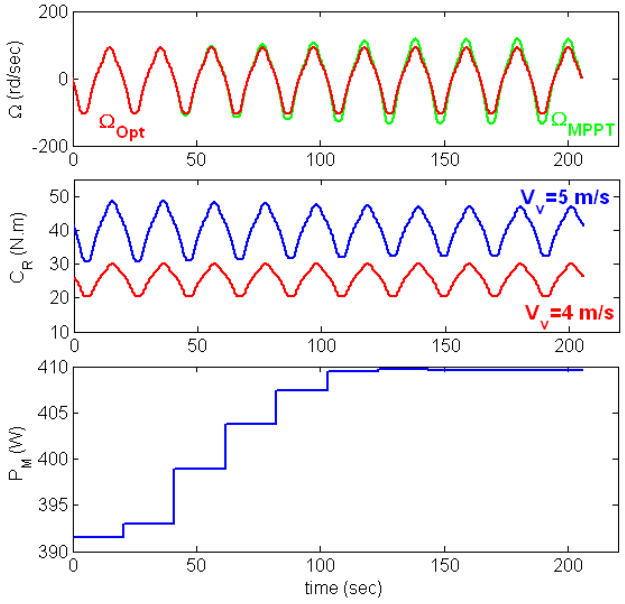

Figure IV.24: Application of MPCT algorithm on the rotation velocity when wind speed changes from 4 to $5m/s$ at instant $40sec$. Upper plot: In dashed red, the optimization resulted rotation velocity, in continuous blue, the MPPT rotation velocity. Center plot: The resistive torque (C_R), in dashed red, at wind speed $4m/sec$, in continuous blue, at $5m/sec$. Lower plot: The average mechanic power.

Fig.IV.26 shows a grid phase current I_{a-G} and the grid phases voltages $V_{a,b,c-G}$. The grid-side converter was successfully controlled to provide the grid with the current having only the $50Hz$ harmonic and is in phase with the voltage.

The previous simulation results are a first and initial step towards the PHIL validation. We remind that in this test the control strategy is divided into two "independent" problems, the kite orientation, that is control of θ, ϕ through the roll angle ψ, and the radial velocity control $\dot{r}$ through driving of the PMSM. Hence the MPPT algorithm acts only on the $\dot{r}$ regardless of the kite coordinates (θ, ϕ).

The setup of Fig.IV.21 was implemented to test the proposed control strategy. At a first step, radial velocity control via the PMSM, the torque emulation and the electrical variables control were tested through application of the optimized radial velocity V_L and the kite torque C_R resulted from KGS simulations in Chapter.III-section.III.2.b. V_L and C_R are scaled to match the experimental bench

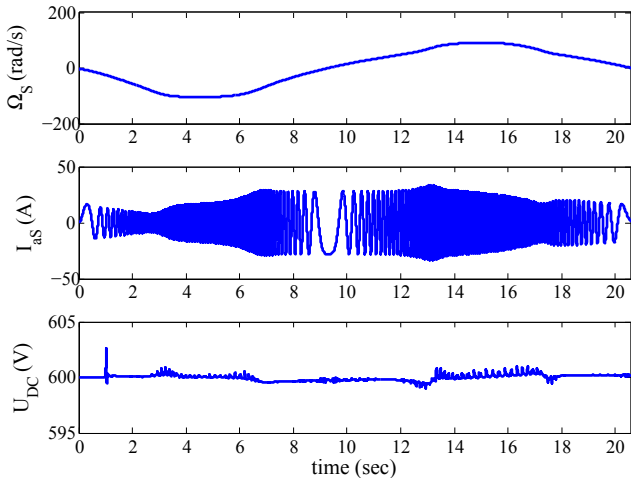

Figure IV.25: Starting from the upper plot: The PMSM rotation velocity (Ω_S), PMSM phase current (I_{aS}), DC bus voltage (U_{DC}).

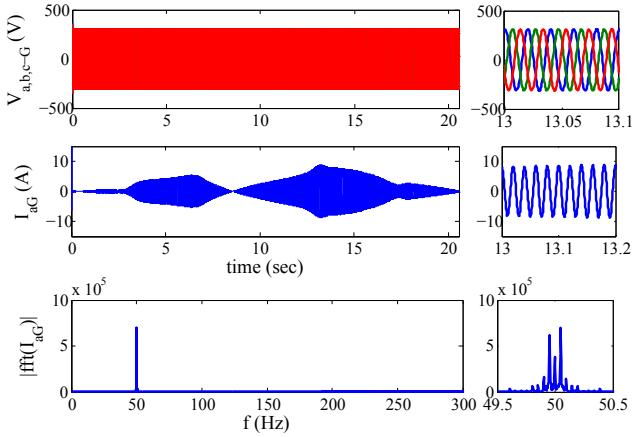

Figure IV.26: Starting from upper figure: Grid voltages, grid current (I_{aG}), its frequency analysis.

characteristics.

As observed in Fig.IV.27, the resulting rotation velocity have cyclic profile that varies in the range $[-1000, 1000]RPM$. Its variations are accompanied by synchronized equivalent variations in the kite torque, which shows how generated power is optimized from the machine point of view.

These variations are translated by machine currents whose frequency, amplitude and phase change accordingly. The frequency is related directly to the rotation speed:

$$f = \frac{\omega}{2\pi} = \frac{p\Omega}{2\pi}$$

Meanwhile the current amplitude represents the torque variations, and the phase represents the rotation velocity direction changes. Notice as well that the DC-bus voltage keeps a constant value despite the variations in the rotation velocity.

For the grid-side converter electrical variables, Fig.IV.28 shows the variations of the output current and the grid voltage following those of the rotation velocity. The current becomes zero before the rotation velocity reaches zero that is due to the losses in the converters elements. This explains also why the current amplitude is higher when the velocity is negative (Recovery phase) than when it is positive (Generation phase).

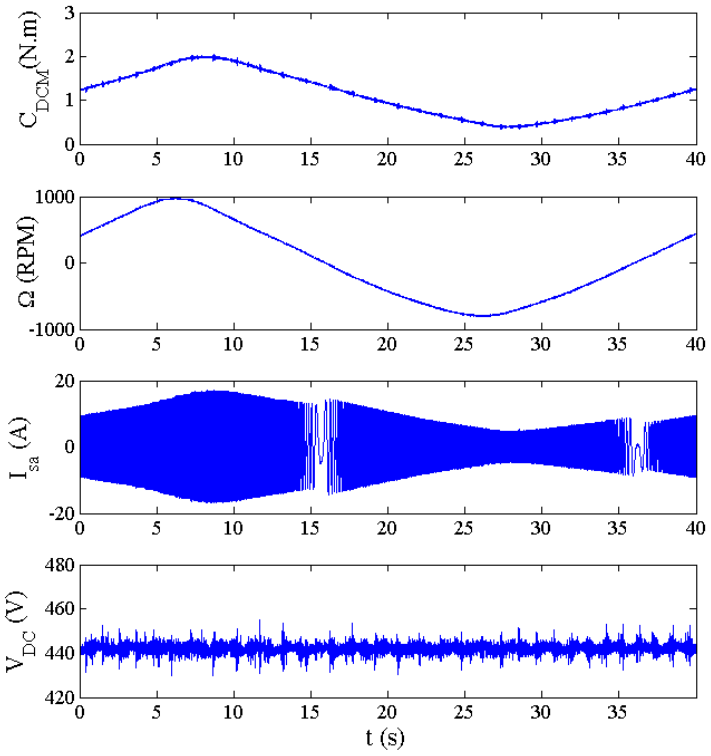

Figure IV.27: Starting from the upper plot: DCM torque (C_{DCM}), PMSM rotation velocity (Ω_s), PMSM phase current (I_{sa}), and DC bus voltage (U_{DC}).

Fig.IV.29 displays a closer look at current the voltage variations. It shows how the current is in phase with the voltage during the generation phase, and $\frac{\pi}{2}$ shifted during the recovery phase.

IV.5 Conclusion

This chapter proposed and tested a solution to grid-integrate the KGS or use it to supply an isolated load. The solution is a power transformation unit consisting of a PMSM and a power electronics interface.

For each connection type, a control scheme is proposed to insure the control of both the mechanical and electrical variables of the power transformation chain. The control laws are tested via simulation then validated on a half-software-half-hardware experimental bench called a Power Hardware-In-the-Loop Simulator.

Moreover, a Maximum Power Cycle Tracking algorithm was proposed to follow the optimal velocity profile that characterizes our relaxation cycle KGS in the case of slow variations of wind speed. This algorithm was tested on a Matlab/Simulink model of the system.

Finally, a fast benchmarking setup based on the previous PHIL simulator was built and tested and is ready to be implemented for the purpose of testing the MPCT algorithms and to assemble the kite model and orientation part with the power transformation unit part.

Further work will include testing under disturbances acting on the kite and will consider the case of unbalanced regimes. They will also take into account voltage dips propagating from the grid

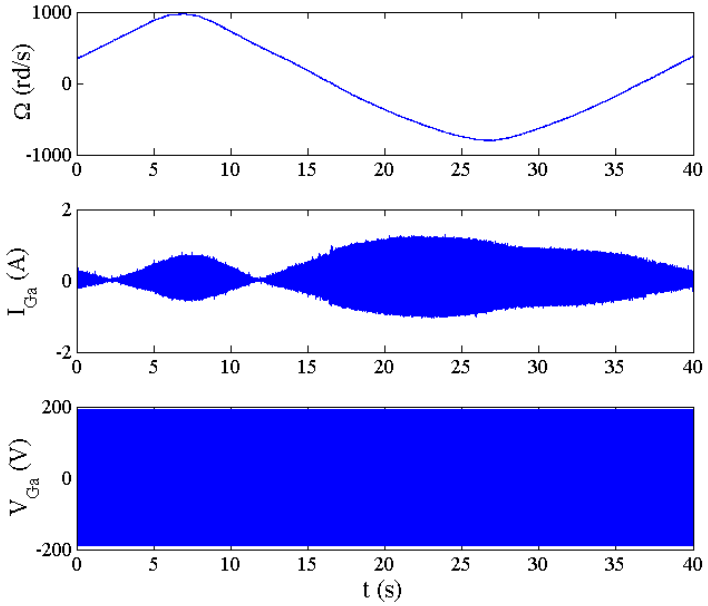

Figure IV.28: Starting from the upper plot: PMSM rotation velocity (Ω_s), grid phase current (I_{sa}), and grid phase voltage (V_{Ga}).

and the system's LVRT (Low Voltage Ride Through) capabilities. The system can also achieve ancillary services via reactive power control for example.

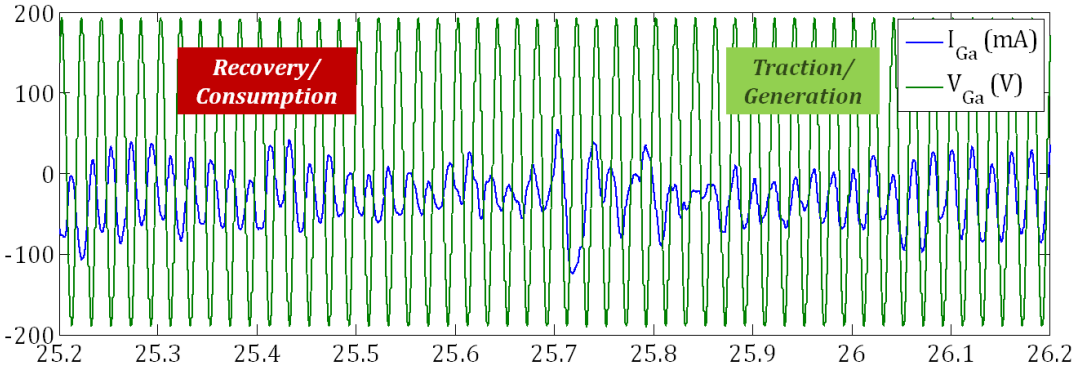

Figure IV.29: Zoom into the grid voltage and current changes when the PMSM changes its rotation direction.

General Conclusions

Although a lot of development has been achieved recently in the renewable energy field, more needs to be done in order to avoid future problems accompanying oil depletion and dependence, as well as nuclear energy safety and public acceptance issues. Of those renewable energy resources, high altitude wind energy (HAWE) is a promising resource because of its availability and regularity.

A solution to harness HAWE is the use of tethered kites. These simple structures allow us to reach high altitudes and transfer the wind energy mechanically to the ground where it is transformed into electrical and conditioned to integrate the grid. However, the limitations on tethers length and kite's height require us to pull down the kite periodically which results in a system that periodically generates/consumes energy and needs to be optimized to minimize the consumed power and maximizes the generation. The outcome system can be classified in the relaxation-cycles category.

This thesis had as main objective the optimization and control of renewable energy systems with relaxation cycles and their grid integration. A secondary yet important objective was to provide a mapping on the latest trends in wind and wave energy domain. The work was conducted in Grenoble electrical engineering laboratory G2Elab, with collaboration with the automatic department in GIPSA-Lab.

A special attention was paid to a kite-based wind system, named "kite generator system", as a representative of relaxation-cycle systems. It was chosen due to its simple structure yet complex dynamics and promising primary test results. The system is a part of the research on-going in GIPSA-lab on HAWE.

After a brief presentation of energy history and expectations, different solutions to harvest wind energy at high altitude and offshore wave energy were over-viewed and compared. Two types were particularly addressed: The kite generator system and the heaving point-absorber system. They both result in a relaxation-cycle when controlled to generate a maximum average power. Those were our case study.

As a first step, the simplified structure of each system as well as their power generation techniques were introduced and their models were developed. We noticed the similarity between both from the resulting power profile point of view. Hence, their grid integration problem can be handled similarly. However, since the kite-based system offers a set of very interesting problems when it comes to its flying part's orbit choice and orientation, it was the one chosen to develop the control strategies on.

The chosen KGS is a closed eight-shaped orbit: The generation (= traction) and the consumption (= recovery) phases occur during the same eight-shaped orbit. Two strategies to choose and control the orbit were proposed.

- ***Nonlinear predictive control (NMPC) based strategy:***

  Using a mathematical model of the system results in the expression of the average power as a function of the normalized tether's radial velocity. Maximizing this power yields the kite's orbit and radial velocity.

  A nonlinear model predictive control is applied to insure the orbit tracking by controlling the kite's roll angle and the traction force.

- ***Virtual constraints control (VCC) based strategy:***

  That is a novel method used recently in Robotics. The KGS is controlled by the attack angle only while the traction force is fixed and determined by the phase: Traction or recovery; which means that the system is under-actuated, and is controlled by forcing some virtual constraints among its variables.

To grid integrate the system or use it to supply an isolated load, a power transformation unit composed of a permanent magnet synchronous machine and a power electronics interface is proposed. In addition to insuring electrical variables control and accordance with the grid, the unit employs a Maximum Power Cycle tracking algorithm to follow the wind's slow variations regardless of the wind speed measurements. It acts on the tether's radial velocity.

Models of this unit were found and control schemes in both connection cases were proposed and validated via simulations and on a real-time hybrid Power Hardware-In-the-Loop simulator.

Another contribution of this thesis is a fast benchmarking setup based on the previous PHIL simulator. This setup offers an interface built on RT-lab between the PHIL simulator and a real-time digital simulator without the need to adapt the algorithms and models codes to RT-lab requirements, which facilitates and accelerates the testing procedure. It was built and tested and is ready to be implemented for the purpose of testing the MPCT algorithms and assembling the kite model and orientation part with the power transformation unit part.

The work realized during the thesis opened doors to many other problems including both the energy resource control and optimization and its grid integration.

Next work will validate the KGS on the proposed fast benchmarking setup before testing on a prototype. It will also test the effect of the disturbances that may act on the kite, or results from the grid such as voltage dips and Low Voltage Ride Through. We propose as well adding a flywheel storage unit and test the system in a stand-alone scenario.

Further work is to complete building an all automated prototype and to implement a more complex model of the KGS for flight simulation.

Chapter V

Résumé Français

V.1 Introduction

Pour répondre à la demande énergétique croissante et pour faire face à l'épuisement du pétrole, ainsi que les effets négatifs de l'avancement industriel et technologique de l'homme sur le climat, plusieurs solutions ont été proposées.

L'un des principaux défis est de décarboniser le réseau électrique en éliminant les générateurs d'électricité combustibles, et les remplaçant de préférence par des ressources qui respectent la nature et l'environnement et qui sont publiquement acceptées. C'est où les ressources énergétiques renouvelables soulèvent comme une solution prometteuse.

Dernièrement, beaucoup de recherche scientifique portant sur l'énergie renouvelable et qui visent à résoudre ses problèmes tels que l'efficacité et l'intégration du réseau, et d'explorer des nouvelles méthodes et structures pour les exploiter. L'axe de recherche ultérieure a conduit à la naissance de *systèmes d'énergie renouvelable à cycle de relaxation*. Ceux-ci ont un cycle de puissance périodique avec deux phases :

- Une ***phase de génération*** au cours de laquelle le système fonctionne dans sa "région de puissance", ce que lui permet de produire de l'électricité jusqu'à ce qu'il atteigne ses limits.
- Une ***phase de récupération*** qui réinitialise l'état du système afin que une nouvelle phase de génération démarre. Le système consomme de l'énergie pendant cette phase.

Une opération d'optimisation est donc nécessaire pour assurer la minimisation de l'énergie consommée et la maximisation de celle générée, tout en respectant les différentes contraintes sur le système lui-même, la source d'énergie primaire, le réseau ou encore les charges.

Cette thèse porte sur l'étude de ces systèmes de génération d'électricité à cycle de relaxation. Des exemples de tels systèmes comprennent les systèmes de traction à base d'aile volant, les systèmes houlomoteurs (utilisant l'énergie des vagues ou de la houle) et certains systèmes thermiques à base d'énergie renouvelable. Dans ce cadre, deux exemples ont été considérés :

- ***Système générateur de cerf-volant*** (KGS : Kite Generator System). Il s'agit d'une solution proposée pour extraire l'énergie du vent stable et forte en haute altitude. Son principe de fonctionnement est d'entraîner mécaniquement une génératrice électrique au sol en utilisant un ou plusieurs cerfs-volants captifs.
- ***Système flotteur oscillant*** (HPS : Heaving Point-absorber System). C'est un système d'énergie houlomotrice flottant qui emploie les oscillations des vagues pour tourner une génératrice électrique et produire de l'électricité. Fig.V.1 montre la structure simplifiée de ce système.

Ces deux systèmes ont été présentés et modélisés pendant la thèse, mais seulement le premier sera présenté en détails dans les sections suivantes. Ceci parce que nous estimons que le système de traction à base de cerf-volant port des défis plus importants et a un avenir prometteur.

En plus des problèmes classiques des ressources énergétiques renouvelables, celles avec un cycle de relaxation sont un domaine de défis ouverts très intéressant, tels que la recherche de solutions

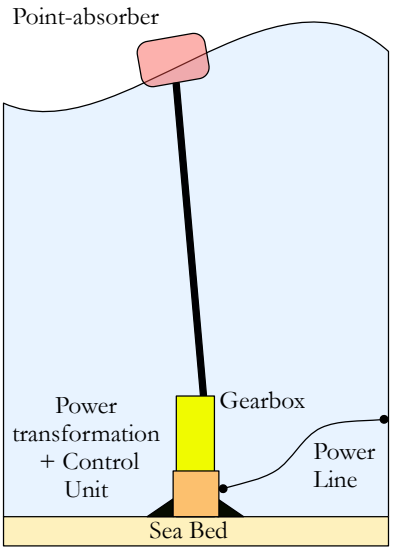

Figure V.1: The HPS simplified structure.

aux problèmes d'optimisation multi-dimensionnelles et le raccordement au réseau. Ces défis sont abordés dans cette thèse réalisé au seine du laboratoire de Génie Electrique de Grenoble (G2ELab) en collaboration avec le laboratoire de Grenoble Images Parole Signal Automatique (GIPSA-Lab). Ce résumé de thèse est organisée en quatre parties principales :

Le premier chapitre est une bref présentation de l'histoire de l'énergie renouvelable et son évolution en concentrant sur l'énergie éolienne et plus précisément l'énergie éolienne aéroportée. Le deuxième chapitre présent le système de traction à base de cerf-volant choisit pour cette étude et sa modélisation. Dans le troisième chapitre, les deux méthodes utilisées pour contrôler l'orientation et la stabilité du cerf-volant sont présentées et testées en simulation. Le quatrième chapitre implique le problème d'intégrer le système cerf-volant sur le réseau électrique. Les chemins de contrôle des variables mécaniques et électriques sont présentés et validés par des simulations ainsi que des tests sur un simulateur temps real (Hardware-in-the-loop Simulator).

V.2 Histoire

Plusieurs milliers des années en arrière l'énergie renouvelable était la source unique d'énergie. Elle a été utilisé pour entrainer les bateaux au longues de la Nile en Egypte il y a 10 siècles. Les restes d'éoliennes verticales en Iran (Fig.V.2) et les norias en Syrie sont des exemples du développement précoce dans les technologies d'énergie renouvelable.

Néanmoins, l'énergie renouvelable a été dominé par l'arrivée des combustibles fossiles dans le XIX^e et XX^e siècle. Ces combustibles étaient la base de la revolution industrielle. L'industrie automobile et la génération d'électricité étaient particulièrement dépendants de cette source d'énergie. En conséquence, le développement dans le domaine d'énergie renouvelable a pris beaucoup de recul. Fig.V.3 montre la dominance des énergies fossiles depuis l'année 1965.

La crise de 1973 aussi bien que les effets négatifs de réchauffement de la planète ont attiré l'attention encore une fois vers les ressources renouvelables qui promettent une énergie propre et durable. Ces ressources sont en concurrence avec l'énergie nucléaire qui offrent des prix compétitifs mais reste très peu acceptés publiquement et non accessibles à tous.

Même si l'énergie produite par des ressources renouvelable répond au moins de 2% de la demande

Figure V.2: Eolienne verticale à Nishtafun en Iran (600 AD).

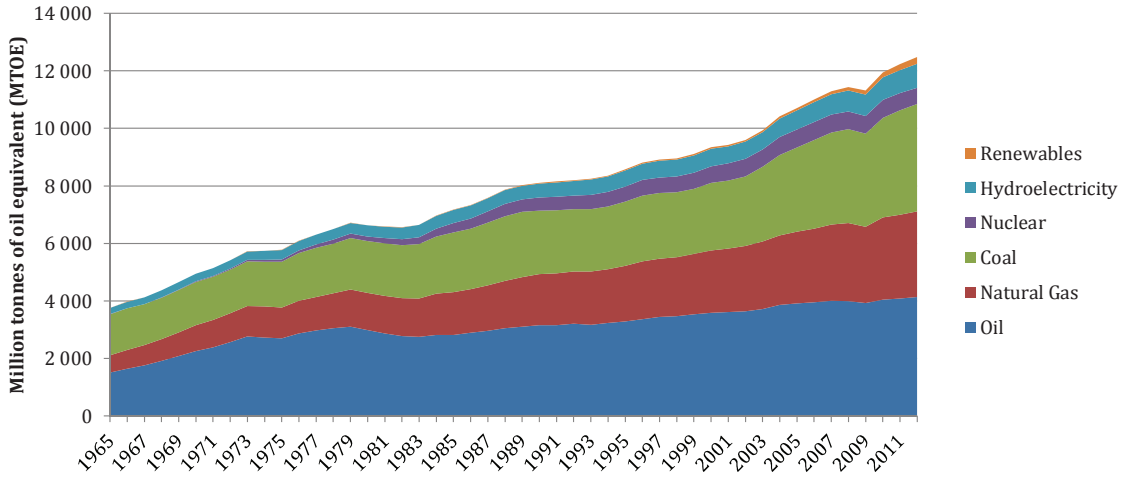

Figure V.3: Consommation mondiale d'énergie par type de ressource.

énergétique globale, sa puissance installée, à part celle de l'énergie hydraulique, a multiplié par 5 pendant les deux dernières décennies. Fig.V.4 montre la tendance selon laquelle la capacité installée de l'énergie éolienne, solaire et celle géothermique a augmenté entre 1995 et 2012.

V.2.a Energie Eolienne

Parmi les ressources renouvelable, l'énergie éolienne a subit la croissance la plus forte. En effet, sa capacité à multiplié par 9 depuis l'année 1995, ce qu'en fait la ressource avec la croissance la plus rapide de tous les temps.

Cette énergie est classiquement exploitée par des éoliennes. Un exemple de ceux-ci est représenté sur la Fig.V.5. Une telle éolienne est composée d'un rotor avec 3 pales connecté directement soit ou soit par une boite à vitesse avec une génératrice. L'éolienne est connectée directement ou via une interface d'électronique de puissance avec le réseau électrique. La génératrice, le rotor et leur contrôle sont portés dans une nacelle sur un mât.

Cette technologie a subit un développement et une recherche intense pendant les dernières trois décennies. Cette recherche a pour but l'augmentation de l'efficacité et la puissance nominale de l'éolienne. En observant le développement de l'industrie des éoliennes, une tendance d'augmenter leur taille est clairement distinguée. L'objective de ceci est de :

- Augmenter la surface de la région de travail (A) avec la quelle la puissance moyenne croît linéairement.

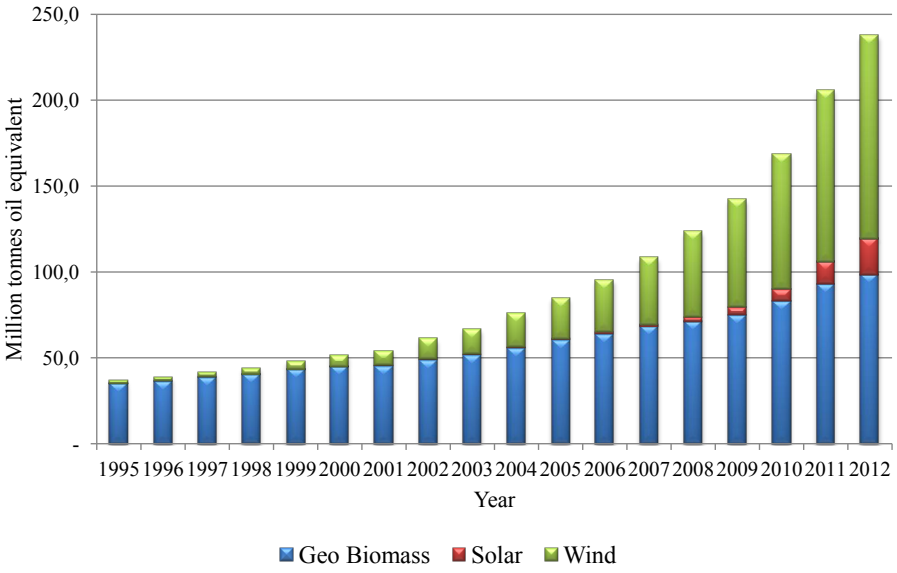

Figure V.4: Capacité installée mondiale.

- Augmenter la hauteur du rotor pour atteindre des vitesses de vent (V) plus importantes, régulières et constantes.

La Fig.V.6 montre un exemple de l'évolution de la vitesse du vent en fonction de l'altitude.

Néanmoins, l'augmentation de la taille des éoliennes est accompagnée par des difficultés techniques comme par exemple : la transportation, la maintenance et la fabrication, ainsi que l'investissement initial qui devient très important. En fait, doubler la hauteur de l'éolien multiplie le coût initiale par cinq! Et pourtant, 30% de la partie extérieur des pales est responsable de produire plus que 60% de la puissance nominale de l'éolienne. En effet, le reste des pales ainsi que le mât sont principalement existant pour soutenir les pointes des pales et transférer l'énergie produite au sol.

Ceci dit, et si nous réussissons à contrôler les pointes des pales à voler et exploiter l'énergie cinétique du vent et puis la transmettre au sol par un câble? Cette idée est derrière le concept des éoliennes aéroportées ou les éoliennes à haute altitude.

V.2.b Energie Eolienne Aéroportée

L'idée d'utiliser les cerf-volants ou les ailes volants pour exploiter l'énergie du vent en haute altitude HAWE (High Altitude Wind Energy) est apparue dans les années soixante-dix mais le premier à calculer l'énergie qui peut être générée par cette manière est M.Loyd qui a publié ses résultats dans le journal d'énergie en 1980.

L'idée principale dans ce papier est qu'un aile volant dans un champ de vent (V) vole à une vitesse G_eV où G_e est l'efficacité aérodynamique de l'aile. Ceci est utilisé pour générer de l'électricité par deux façons :

- ***La génération d'énergie à bord :*** Dans ce cas, la grande vitesse de l'aile est employée pour entrainer des éoliennes installées au bord et l'énergie électrique produite est ensuite transférée au sol par un câble conducteur. Ceci est appelé aussi le mode de trainée (Drag mode). La Fig.V.7 montre deux exemples des systèmes qui utilisent ce principe : La matrice des éoliennes embarquées de Joby et le Makani M1 de GoogleX.
- ***La génération d'énergie au sol :*** Dans ce cas, la force aérodynamique résultante est utilisée pour tracter le câble et trainer une machine électrique au sol, ceci est le mode de

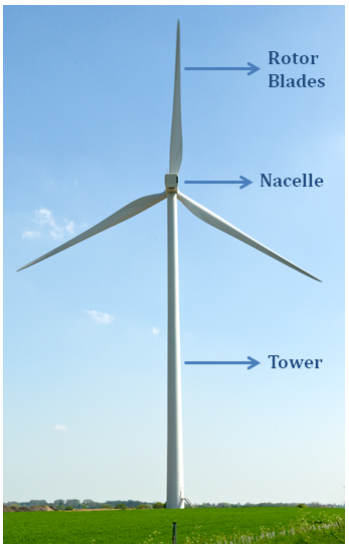

Figure V.5: Eolienne classique à trois pales.

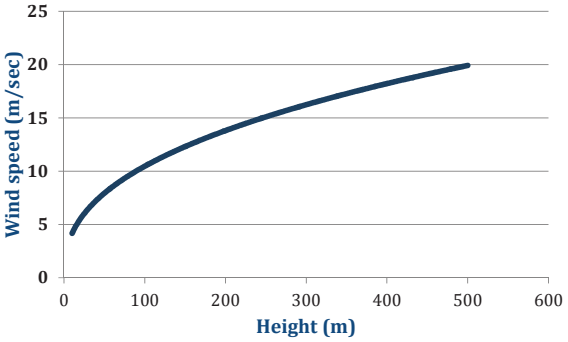

Figure V.6: Vitesse de vent en fonction de l'altitude.

portance (Lift mode). Fig.V.8 montre deux exemples de ces systèmes : Le premier est l'utilisation des cerf-volants par SkySails pour augmenter l'efficacité énergétique dans les bateaux 30%, et le deuxième est un prototype de KitGen en Italie.

L'énergie produite par les deux modes, est donnée par eq.V.1. En plus de la vitesse du vent, elle est une fonction des coefficients de portance C_L et de trainée C_D de l'aile, la surface A et la densité d'air ρ.

$$P_{max} = \frac{2}{27}\rho A C_L \left(\frac{C_L}{C_D}\right)^2 V^3 \tag{V.1}$$

Afin de voir le potentiel de cette idée, nous considérons un système éolien aéroporté avec les paramètres suivants : $V = 13m/s, C_L = 1, C_D = 0.07$. Un tel système a une densité surfacique de $40kW/m^2$ ce qui est 150 fois plus que le maximum de $0.26kW/m^2$ qui peut être obtenu par un système photovoltaique. Un autre exemple pour comparer :

En construisant un system éolien aéroporté rigide basé sur les ailes d'un avion Airbus-380 dont le surface est $845m^2$ et l'envergure est $80m$, le système résultant avec ses câbles et générateurs aura un poids totale de 40tons et une puissance nominale de $30MW$. Cette énergie peut-être produite

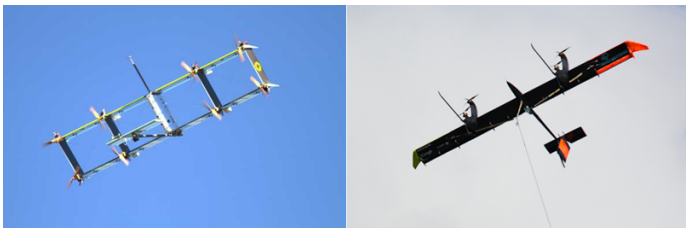

Figure V.7: A gauche : Le prototype de Joby, à droite : Le Makani M1 prototype.

Figure V.8: A gauche : Un cerf-volant de SkySails , à droite : Un prototype de KiteGen.

par quatre éoliennes Enercon $E126$ dont chacune a une puissance nominale de $7.5MW$ et un poids 3100tons. Cela montre la quantité des matérielles qui peut-être économisé en utilisant cette technologie.

La recherche à exploiter l'énergie de vent en haute altitude a déjà attirée l'attention des dizaines d'équipes académiques et industrielles dans le monde surtout depuis l'année 2005. Parmi les pionniers, les équipes de recherche à la Polytechnique de Turin en Italie (le projet KitGen) et à l'université de Delft aux Pays-bas, aussi que l'entreprise SkySail en Allemagne et Makani-Power aux Etats-Unis. Depuis 2008, la société de l'Energie Eolienne Aéroportée organise une conférence multi-disciplinaire annuelle (Airborne Wind Energy Conference AWEC) qui présent les dernières tendances et développements dans ce domaine, y compris le design, les matérielles utilisés, les méthodes de contrôle etc, ainsi que les défis aux quelles il faut faire face pour conduire la technologie jusqu'à la commercialisation.

V.3 Système Génératrice de Cerf-volant

Dans la suite, le système adopté pour cette étude est présenté et modélisé. Avant de montrer le choix du système, nous faisons une comparaison rapide entre les deux modes de génération dans les systèmes éoliens aéroportés. En général la génération au sol utilise des cerf-volants flexibles tandis que la génération à bord utilise des cerf-volants rigides. La comparaison est résumée sur le graphique de Fig.V.9.

La génération à bord en utilisant des cerf-volants rigides offre une densité surfacique plus importante grâce à leur efficacité aérodynamique mais la partie volant du système est très complexe et lourde par rapport à un système de génération au sol. Il est nécessaire d'utiliser un système de navigation embarqué en plus de turbines. Les cerf-volants flexibles sont beaucoup plus simples à piloter et leur partie volante est légère ce qui augmente la sûreté du système. En plus d'avoir une densité massique de puissance plus importante.

Pour les raisons citées ci-dessus, un système de traction à base de cerf-volant a été choisi pour étudier ses problèmes de contrôle et d'intégration au réseau. Dans les sections suivantes, la structure de ce système est présentée ainsi que sa modélisation.

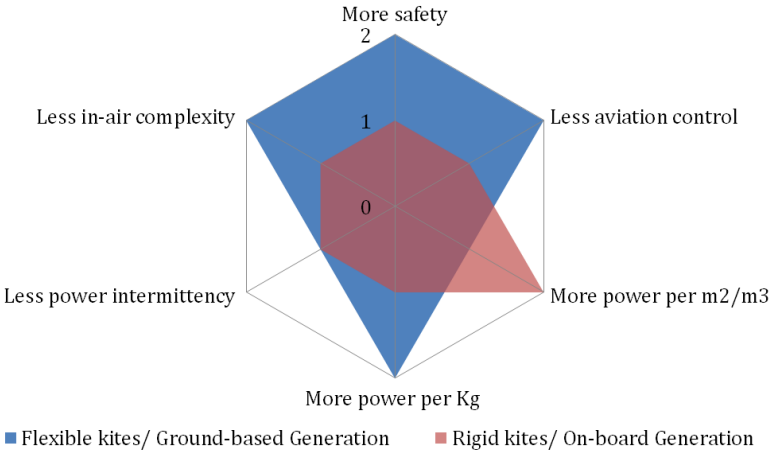

Figure V.9: La génération d'énergie à bord (Mode de trainée) vs la génération d'énergie au sol (Mode de portance).

V.3.a Structure

La structure simplifiée du système éolien aéroporté adopté sur cette étude est représenté dans La Fig.V.10. C'est un système de traction à base de cerf-volant nommé ***Kite Generator System (KGS)***. Le système est composé d'un cerf-volant attaché par un seul câble au sol. Le cerf-volant est orienté par un mécanisme installé à son niveau. Le câble transmet la traction causée par la portance appliquée sur le cerf-volant au sol où il entraîne une machine électrique. La puissance générée est injectée dans le réseau après un passage par une interface d'électronique de puissance.

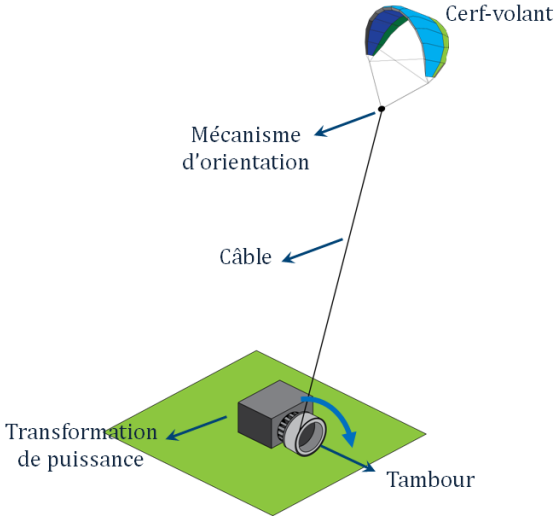

Figure V.10: Structure simplifiée de KGS.

La trajectoire du cerf-volant peut prendre plusieurs formes, la plus populaire est en forme d'un huit allongé ce qui maximise le vent de travers soufflé sur le cerf-volant. Il y a deux possibilités dans ce cas :

- Mode de pompage : Le cerf-volant suit la trajectoire tout en augmentant son altitude et lorsque il arrive à son altitude maximale, ou son longueur de câble maximal, il est tiré vers le bas. Cette opération consume de l'énergie et le résultat est un cycle de généra-

tion/consommation.

- Mode d'orbite fermée : Où le cerf-volant reste sur une seule trajectoire fermée pendent les quelles deux phases d'opération sont distinguées : Une phase de génération pendant la quelle le cerf-volant est en train de voler directement dans la direction du vent de travers et il tracte le câble, et une phase de consommation où le cerf-volant est tiré afin de fermer la trajectoire.

L'existence d'un cycle de génération/consommation nécessite d'une étape d'optimisation afin de maximiser la puissance moyenne produite en respectant les contraintes du système comme la longueur de câble, sa traction, les angles de vol, etc.

V.3.b Modélisation

Alors que l'objective de ce travail est d'optimiser et contrôler le KGS et les intégrer dans le réseau électrique, des hypothèses réalistes suivantes sont prises en compte :

- Un modèle d'un point de masse pour le cerf-volant et son câble. Un tel modèle est rugueux car il ne tient pas compte de la flexibilité et des déformations du cerf-volant mais il est utile pour contrôler et estimer la puissance générée.
- Une efficacité aérodynamique élevée.
- Un câble inélastique et droit. Cette hypothèse est correcte lorsque la longueur du câble est moins que $1000m$ et son inclinaison est inférieure à 80^o.
- Les dimensions du câble permettent de négliger sa force de portance et considérer sa trainée seulement.
- Le vent est uniforme avec une direction non-variable ce qui est en accord avec l'effet que le cerf-volant vole en haut altitude.
- Des informations sur la position et la vélocité du cerf-volant sont fournies par des capteurs et des observateurs.

Les dynamiques de cerf-volant sont décrites par la deuxième loi de Newton :

$$m\vec{\gamma} = \vec{F}_{grav} + \vec{F}^{aer} + \vec{F}_{trac} \tag{V.2}$$

Avec m la masse de cerf-volant, et $\vec{\gamma}$ est l'accélération :

$$\vec{\gamma} = \begin{bmatrix} r\ddot{\theta} + 2\dot{r}\dot{\theta} - r\dot{\phi}^2 \sin\theta\cos\theta \\ r\sin\theta\ddot{\phi} + 2\dot{\phi}(\dot{r}\sin\theta + r\dot{\theta}\cos\theta) \\ \ddot{r} - r(\dot{\theta}^2 + \dot{\phi}^2\sin^2\theta) \end{bmatrix} \tag{V.3}$$

La force aérodynamique $\vec{F}^{aer}$ est liée directement au vent effective W_e, qui est la différence entre la vitesse de vent et la vélocité du cerf-volant. Les composants de portance et de traînée sont exprimées par les equations V.4. Fig.V.11 montre les forces appliquées sur le cerf-volant.

$$\begin{array}{rcl} \vec{F}_D^{aer} & = & -\frac{1}{2}\rho_a A C_D |W_e|^2 \vec{x}_w \\ \vec{F}_L^{aer} & = & -\frac{1}{2}\rho_a A C_L |W_e|^2 \vec{z}_w \end{array} \tag{V.4}$$

Le modèle peut être présenté dans la forme générale :

$$\dot{x}(t) = f(x(t), u(t), P(t)) \tag{V.5}$$

avec des contraintes sur l'état $x(t)$ et le vecteur de contrôle $u(t)$,

$$x_{min} \leq x(t) \leq x_{max}, \quad u_{min} \leq u(t) \leq u_{max} \tag{V.6}$$

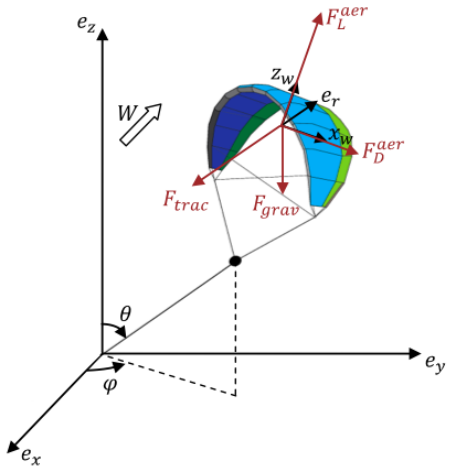

Figure V.11: Les forces du cerf-volant.

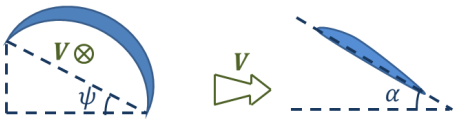

Figure V.12: A gauche : l'angle de roulis, à droite : l'angle d'attaque.

L'état contient des informations sur la position et la vélocité de cerf-volant représentées dans les coordonnées sphériques, tandis que le contrôle peut être importé sur l'angle de roulis, l'angle d'attaque et/ou la traction de câble. Fig.V.12 présente les angles de vol commandées. $P(t)$ contient les effets externes qui influencent le comportement du système, comme par exemple : les perturbations de vitesse du vent et les creux de tension du réseau.

La puissance moyenne produite par le système est le produit de la force de traction F_{trac} et la vitesse radiale de câble V_L :

$$\bar{P}_M = \frac{1}{T}\int_0^T F_{trac}^M(t)V_L(t)dt \tag{V.7}$$

L'objective d'optimisation est de maximiser cela en respectant les limites physiques du système.

V.4 Optimisation et Contrôle

Le système KGS décrit dans la sec.V.3 est un système non-linéaire, complexe, instable dans la boucle ouverte avec des contraintes sur l'état et le contrôle. Pour cela des méthodes non-conventionnelles sont nécessaires pour garantir le contrôle de cerf-volant afin de suivre une trajectoire spécifique qui maximise la puissance moyenne générée.

Dans la suite, deux stratégies d'optimisation et de contrôle sont explorées. La première utilise la commande prédictive (Model predictive control MPC) et la deuxième utilise une commande basée sur les contraintes virtuelles (Virtual Constraints Control VCC).

V.4.a Commande Prédictive

La stratégie est présentée dans la Fig.V.13 et peut être divisée en trois étapes :

- ***Choix d'orbite***

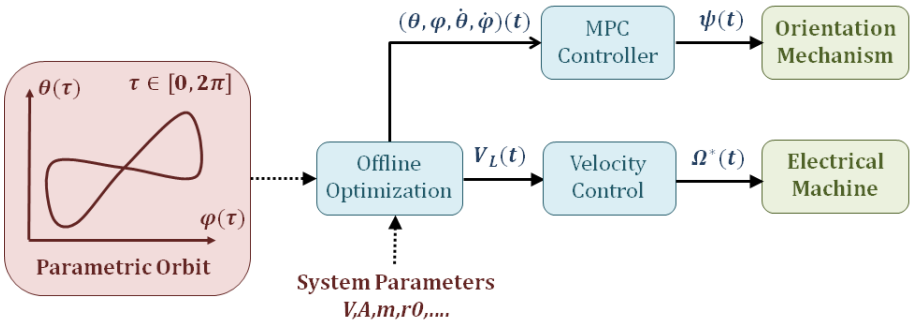

Figure V.13: Stratégie de contrôle utilisant la commande prédictive.

La première étape commence par définir une orbite paramétrique en forme d'un huit. L'orbite est présentée par les équations suivantes :

$$\begin{aligned} \theta(\tau) &= \theta_0 + \cos(Rot)\Delta\theta \sin(2\tau) - \sin(Rot)\Delta\phi \sin(\tau) \\ \phi(\tau) &= \phi_0 + \sin(Rot)\Delta\theta \sin(2\tau) + \cos(Rot)\Delta\phi \sin(\tau) \end{aligned} \tag{V.8}$$

Avec : r_0 la longueur initiale de câble, $\Delta\theta, \Delta\phi, \theta_0, \phi_0$ et Rot définissent les variations des paramètres θ et ϕ (Fig.V.14).

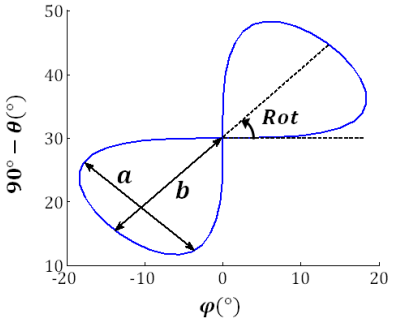

Figure V.14: Initial orbit parameters.

Le choix de ces paramètres est essentiel pour déterminer la puissance maximale qui peut être exploité. Par exemple, cette puissance croît avec la rotation d'orbite : Le maximum est à une rotation de 90^o, et elle a une valeur maximale à une certaine inclination θ_0 qui dépend de la nature du sol. La Fig.V.15 montre ces deux fonctionnalités.

- ***Optimisation de l'orbite***

Le problème d'optimisation comprend maximiser la puissance moyenne générée par le système en gardant la condition d'orbite fermée. Ceci est représentée dans le modèle mathématique simplifié décrit par Argatov [ARS09] par la suite :

$$\max_{v(\tau)} \left(\bar{P}_M(v)\right) = \max_{v} \left(\frac{1}{2}\rho_a A C_L G_e^2 V^3 J_0(v)\right) \tag{V.9}$$

Avec :

$$\int_0^{2\pi} \frac{vh(\tau)}{w_{\|} - v} d\tau = 0$$

Le résultat de cette optimisation est la vitesse radiale du câble $\hat{v}(\tau)$ et le vecteur de temps correspondant $t(\tau)$.

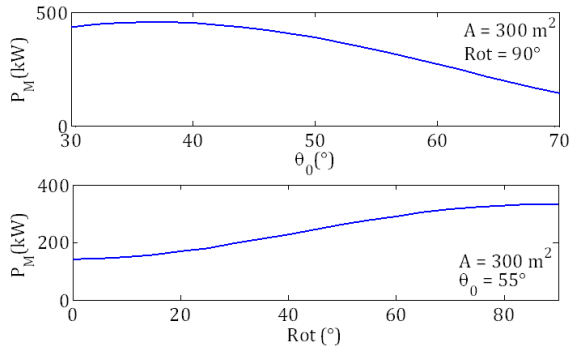

Figure V.15: En haut : La puissance mécanique moyenne en fonction de l'angle d'inclination θ_0, en bas : En fonction de la rotation d'orbite *Rot*.

- ***Poursuite de l'orbite***

  Les variables de référence à suivre sont la vitesse radial V_L et la position angulaire $\theta(t)$ et $\phi(t)$. A fin de suivre la référence, la vitesse radial est contrôlée par la machine électrique au sol et l'angle de roulis ψ est commandé pour orienter le cerf-volant et suivre les angles $\theta(t)$ et $\phi(t)$.

  La commande prédictive cherche de commander l'angle ψ qui minimise la fonction de coût :

$$\min_u \|(\ddot{x}_{ref} - \ddot{x}) + \lambda_1 (\dot{x}_{ref} - \dot{x}) + \lambda_2 (x_{ref} - x)\|^2$$

  Avec $x = [\theta, \phi, \dot{\theta}, \dot{\phi}]$ et $u = \psi$.

L'application

Table.V.1 montre les paramètres principaux du système KGS, et Fig.V.16 montre les orbites de teste. Orbite 2 est le résultat de pivoter la première orbite à 90°, tandis que l'orbite 3 est le résultat de l'amplification de l'orbite 1.

Table V.1: Les paramètres du système cerf-volant KGS

V	4	Vitesse de vent (m/s)
A	5	Surface du cerf-volant (m^2)
C_L	1.5	Coefficient de portance
C_D	0.15	Coefficient de tra înée

Les profils des vitesses radiales optimales sont montrés dans la Fig.V.17. Pivoter l'orbite à 90° s'est traduit par doubler la période de profil de vitesse, ainsi que doubler les dimensions d'orbite conduit aussi à doubler la période de vitesse radiale.

Table.V.2 inclut les valeurs de puissance moyenne et période correspondantes à chaque orbite. Ces résultats étaient attendus et sont en accord avec les résultats de [ARS09].

V.4.b Les Contraintes Virtuelles

Les contraintes virtuelles sont des relations entre les variables d'un système Lagrange sous-actionnés forcées par une feedback. Cette idée a été déjà étudiée et appliquée dans le domaine de la robotique pour résoudre des problèmes de balance et des mouvements périodiques. Parmi les applications :

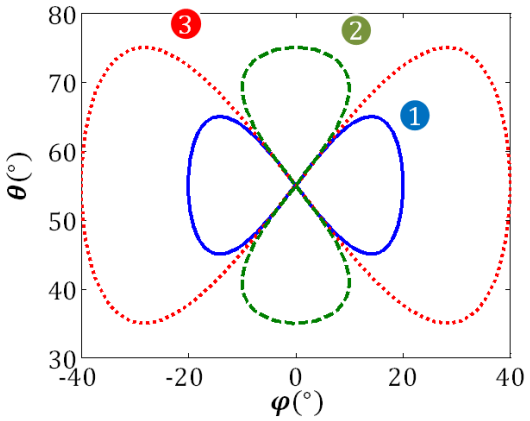

Figure V.16: Orbite paramétriques de teste.

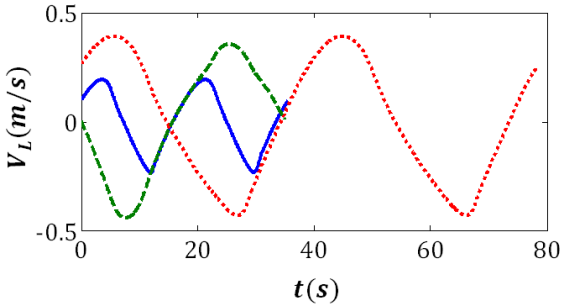

Figure V.17: La vitesse radial optimale correspondante.

Le Rabbit robot, le pendule inversée, etc.

En général, un système est exprimé dans eq.V.10 où :

- $q = [q_1, q_2, ..., q_n]$ est le vecteur des coordonnés généralisés et $\dot{q}$ est son vecteur de vélocité.
- u est le vecteur des entrées de commande et B est la matrice de contrôle.
- $L(q, \dot{q})$ est le Lagrangian de système.

Ce système est sous-actionné si :

$$dim(u) < dim(q)$$

.

$$\frac{d}{dt}(\frac{\partial L}{\partial \dot{q}}) - \frac{\partial L}{\partial q} = B(q)u \tag{V.10}$$

Renforcer des contraints virtuelles qui relient tous les coordonnés $[q_2, ..., q_n]$ à q_1 mène au système auxiliaire avec un cycle limite exprimé dans eq.V.11.

$$\alpha(q_1)\ddot{q_1} + \beta(q_1){\dot{q_1}}^2 + \gamma(q_1) = 0 \tag{V.11}$$

Selon [SPCdW05], la stratégie de rétraction utilisée pour renforcer les contraintes virtuelles mène à la génération d'un mouvement périodique de tout les dégrées de liberté du système. Cette idée est employée pour assurer la suite et la stabilisation du système cerf-volant KGS sur une orbite.

L'application des contraintes virtuelles pour contrôler le vol de cerf-volant est une nouvelle approche proposée pour la première fois avec cette thèse. Dans cette application, un KGS qui fonctionne en

Table V.2: La période et la puissance moyenne des orbites optimisées

Orbite	1	2	3
$P_M(W)$	240	840	844
Période (s)	35.4	35.0	78.4

mode pompage en deux dimensions est choisit. Ce modèle représente le indoors prototype réduit construit et testé à GIPSA-Lab [AHB11a]. Le cerf-volant a deux dégrées de liberté : une translation r et une rotation θ et il est contrôler en commandant l'angle d'attaque α, ceci est représenté dans Fig.V.18. La force de traction est constante dans ce cas.

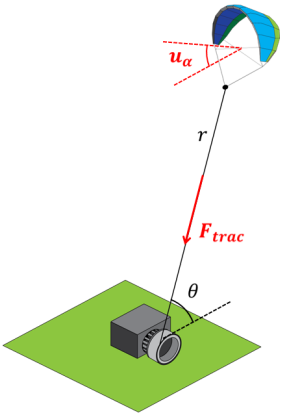

Figure V.18: KGS en mode pompage en deux dimensions.

La méthodologie suivie est présentée dans la Fig.V.19. Les étapes de celle-ci sont expliquées par la suite.

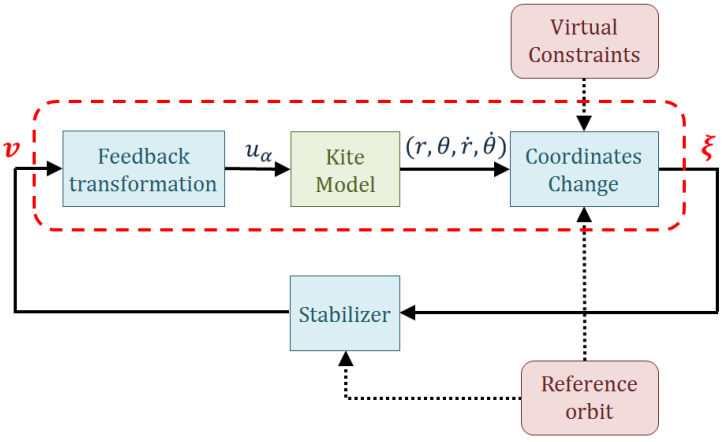

Figure V.19: Diagramme de la méthodologie VCC.

- ***Le Modèle Sous-actionné de KGS***

  Le modèle adopté pour le système est donné par :

$$D(\theta, r)\begin{bmatrix}\ddot{\theta}\\ \ddot{r}\end{bmatrix} + C(\theta, r, \dot{\theta}, \dot{r})\begin{bmatrix}\dot{\theta}\\ \dot{r}\end{bmatrix} + \nabla P(\theta, r) = B(\theta, r)\alpha_u \tag{V.12}$$

où :

- La matrice d'inertie est :

$$D(\theta, r) = \begin{bmatrix} Mr & 0 \\ 0 & (M + M_{IM}) \end{bmatrix} \tag{V.13}$$

- La matrice de Coriolis est :

$$C(\theta, r, \dot{\theta}, \dot{r}) = \begin{bmatrix} 2M\dot{r} & 0 \\ -Mr\dot{\theta} & 0 \end{bmatrix} \tag{V.14}$$

- La fonction d'énergie potentielle est :

$$\nabla P(\theta, r) = \begin{bmatrix} bv_r^2 \sin(\theta - \alpha_w) \\ -bv_r^2 \cos(\theta - \alpha_w) \end{bmatrix} - \begin{bmatrix} av_r^2(\frac{\partial C_l}{\partial \alpha}\alpha_w + C_{L0})\cos(\theta - \alpha_w) \\ av_r^2(\frac{\partial C_l}{\partial \alpha}\alpha_w + C_{L0})\sin(\theta - \alpha_w) \end{bmatrix} + \begin{bmatrix} W\cos\theta \\ W\sin\theta + T \end{bmatrix} \tag{V.15}$$

- et la matrice de contrôle est :

$$B = av_r^2 \frac{\partial C_l}{\partial \alpha} \begin{bmatrix} \cos(\theta - \alpha_w) \\ \sin(\theta - \alpha_w) \end{bmatrix} \tag{V.16}$$

- ***Les Dynamiques Réduites***

En appliquant le contraint virtuelle :

$$r = h(\theta)$$

les dynamiques réduites résultantes de système sont :

$$\alpha(\theta)\ddot{\theta} + \beta(\theta)\dot{\theta}^2 + \gamma(\theta) = 0 \tag{V.17}$$

- ***La Linéarisation en feedback Partielle***

Alors que l'objective de contrôle est d'assurer que $(y = r - h(\theta) = 0)$, le changement de coordonnées de $[r, \theta, \dot{r}, \dot{\theta}]$ à $[y, \theta, \dot{y}, \dot{\theta}]$ est plus représentative du problème. Le résultat de ce changement de coordonnées est un système partiellement linéaire

$$\begin{cases} \alpha(\theta)\ddot{\theta} + \beta(\theta)\dot{\theta}^2 + \gamma(\theta) = g_y(\theta, \dot{\theta}, \ddot{\theta})y + g_{\dot{y}}(\theta, \dot{\theta})\dot{y} + g_v(\theta)v \\ \ddot{y} = v \end{cases} \tag{V.18}$$

En [SRPS05], les auteurs proposent d'ajouter une nouvelle variable I qui exprime la distance de l'orbite de référence et qui facilite le design de stabilisateur. Les nouvelles coordonnées $\xi = [I, y, \dot{y}]^T$ mènent à la représentation de eq.V.19.

$$\begin{cases} \dot{I} = \frac{2\dot{\theta}}{\alpha(\theta)}\left[g_y(t)y + g_{\dot{y}}(t)\dot{y} + g_v(t)v - \beta(\theta)I\right] \\ \ddot{y} = v \end{cases} \tag{V.19}$$

- ***Le Design de Contrôleur***

La représentation d'état du système linéaire variant dans le temps (eq.V.19) est :

$$\dot{\xi} = A(t)\xi + b(t)v \tag{V.20}$$

Le choix de la variable de feedback v peut être inspiré de [SRPS05] où un contrôleur LQR classique est utilisé.

L'application

Afin de montrer l'efficacité de cette méthode, une simulation sur Matlab qui utilise les paramètres de prototype indoors de GIPSA-Lab est réalisée. L'objective est de stabiliser le cerf-volant autour d'une orbite périodique en contrôlant l'angle d'attaque seulement. La Fig.V.20 montre l'orbite de référence et l'orbite du cerf-volant dans l'espace de phase $(\theta, \dot{\theta})$. La Fig.V.21 montre l'évolution des variables du système ainsi que le contrôle de l'angle d'attaque. Renforcer les contraintes virtuelles a donné lieu à un système exponentiellement stable sur son cycle limite, et le résultat est que tout les dégrés de liberté du système finissent par suivre un mouvement périodique.

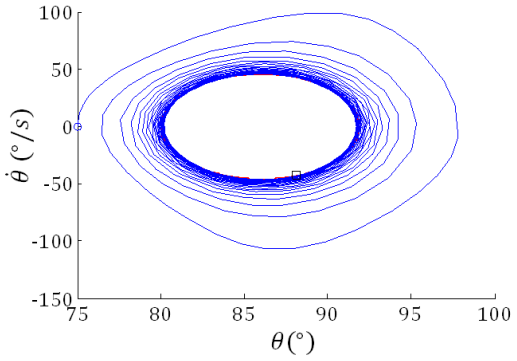

Figure V.20: Le phase plot.

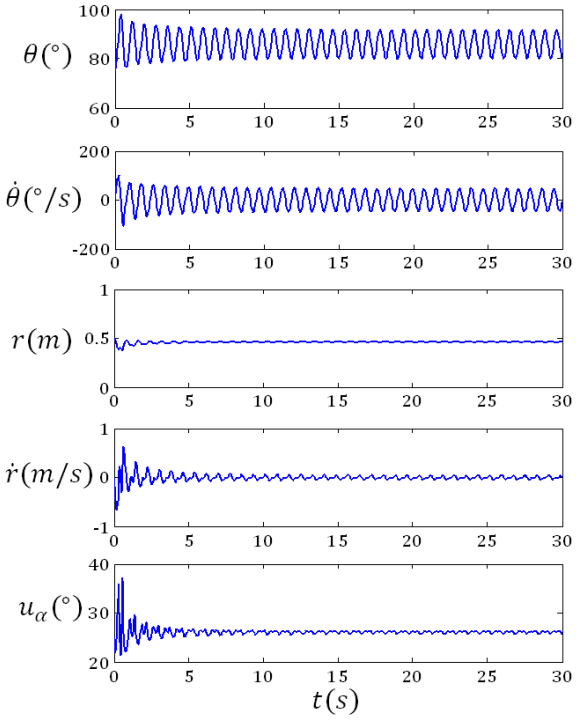

Figure V.21: Développement des variables du système.

V.5 Intégration au Réseaux

L'intégration du système cerf-volant (KGS) sur le réseau électrique ou son utilisation pour alimenter une certaine charge est réalisé à travers d'une interface de transformation de puissance. Cette interface est représentée sur la Fig.V.22.

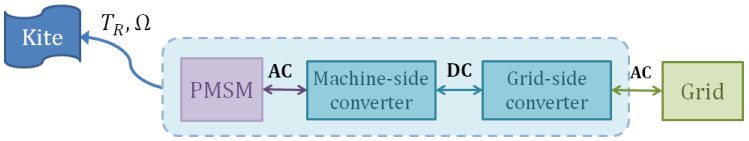

Figure V.22: Evolution des variables du système.

L'interface est composée d'une machine électrique qui transforme la puissance mécanique exploitée par le cerf-volant et transmise par le câble en puissance électrique avec une fréquence variable. Celle-là est ensuite standardisée et injectée dans le réseau ou utilisée pour alimenter une charge.

Dans la suite, l'interface de transformation de puissance est détaillée et modélisée puis son chemin de contrôle est présenté. Ensuite, un simulateur **Hardware-In-the-Loop (HIL)** qui permet de tester les chemins de contrôle proposés est présenté ainsi que l'implémentation de KGS sur celui-ci. En fin, les résultats de validation de KGS en simulation et sur le HIL sont présentés.

V.5.a L'Interface de Transformation de Puissance

La transmission de couple entre le cerf-volant et la machine électrique est exprimée par l'équation mécanique (eq.V.21)

$$C_G - C_R - D\Omega_S = J\frac{d\Omega_S}{dt} \tag{V.21}$$

oú :

- $\Omega_S = \frac{V_L}{K}$ est la vitesse de rotation, avec K combine le facteur de la boîte de vitesse et le diamètre du tambour R.
- J est l'inertie totale du cerf-volant, de tambour et de rotor.
- C_G est le couple générateur.
- D est l'estimation de facteur d'amortissement.

La chaîne de transformation de puissance est représentée dans la Fig.V.23. La machine utilisée est une machine synchrone à aimants permanents présentée par son modèle électrique de Behn-Eschenburg. Deux convertisseurs à transistors sont implémentés pour installer le KGS sur le réseau ou pour alimenter une charge isolée.

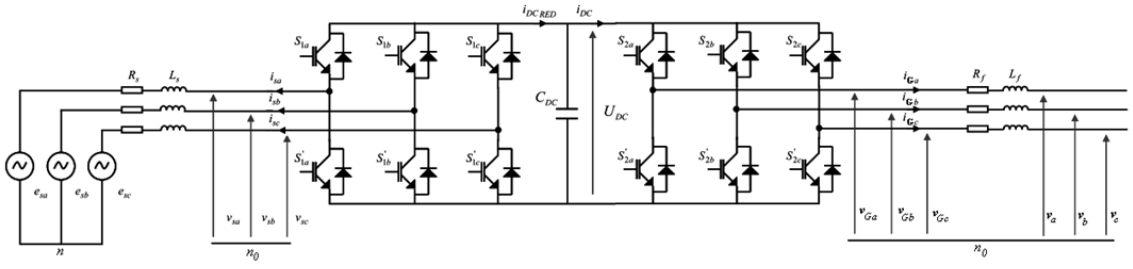

Figure V.23: Représentation électrique de la machine synchrone à aimants permanents et les convertisseurs AC/DC et DC/AC.

Afin de contrôler le flux d'énergie dans la chaîne, le chemin de contrôle de la Fig.V.24 est appliqué. Il est divisé en trois niveaux :

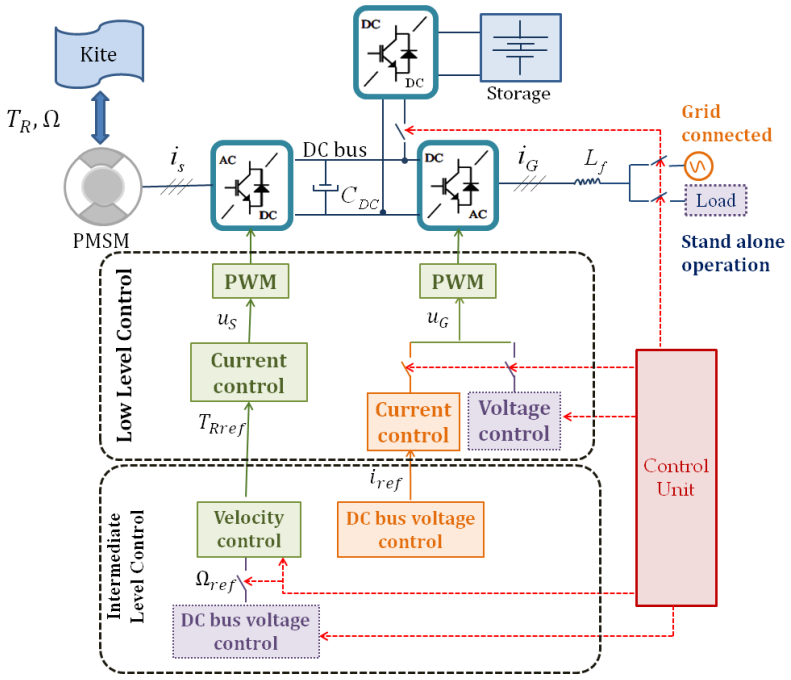

Figure V.24: Chemin de contrôle générale de l'interface de transformation de puissance.

- ***Niveau bas de contrôle***

  Ce niveau génère les signaux MLI (Modulation de largeur d'impulsion) qui contrôlent la fermeture et l'ouverture des interrupteurs des convertisseurs afin de contrôler, soit le courant, soit la tension des convertisseurs selon le type de connexion (Réseau ou charge).

- ***Niveau intermédiaire de contrôle***

  Ce niveau de contrôle génère les références nécessaires pour le niveau précédent. La vitesse de la machine est contrôlée par le convertisseur côté machine. La tension de bus continu est contrôlée soit en commandant le courant du convertisseur côté réseau dans le cas de connexion réseau, soit en contrôlant la vitesse de rotation de la machine en cas de connexion avec une charge.

- ***Niveau haut de contrôle***

  Ce dernier niveau de contrôle est responsable de générer les signaux de référence manquants et contrôler le flux d'énergie dans l'ensemble. Deux cas sont distingués :

  - ***La connexion au réseau fort infini***

    Dans ce cas, le KGS injecte la puissance générée dans le réseau pendant sa phase de génération et il obtient la puissance nécessaire pour sa phase de récupération du réseau. Ici, le convertisseur coté machine contrôle la vitesse de rotation de la MSAP afin de maximiser la puissance moyenne et le convertisseur coté réseau contrôle la tension du bus continu.

  - ***La connexion avec une charge isolé***

    Ce cas nécessite l'addition d'un stockage d'énergie pour alimenter le KGS pendent sa

phase de récupération. Le convertisseur coté machine contrôle la tension du bus continu et celui coté charge contrôle la tension qui aliment la charge.

Au plus, ce niveau de contrôle inclut un algorithme de poursuite de maximum de puissance qui ressemble à un algorithme de "Maximum power point tracking" utilisé dans les éoliennes classiques pour chercher la vitesse de rotation qui maximise la puissance. Dans le cas du système KGS, l'algorithme cherche le profile de vitesse radiale de câble qui maximise la puissance moyenne, dans ce cas l'algorithme est nommé : Maximum Power Cycle Tracking (MPCT).

V.5.b Validation

Afin de valider les stratégies de contrôle proposées, un banc expérimental "Hardware-In-the-Loop" construit à G2ELAB est utilisé. Ce banc offre:

- Une flexibilité pour tester des scénarios de gestion de l'énergie illimitée et des architectures de contrôle différentes sans devoir changer la structure physique du plateforme;
- Un coût réduit par rapport à un prototype;
- Une facilité et sécurité d'application;
- Un contrôle non destructif.

Dans ce banc la partie volant de syst ème KGS ainsi que le tambour sont remplacés par une machine à courant continue, bien que le reste du système (MSAP + interface d'électronique de puissance) est physiquement existant. Le modèle de cerf-volant aussi bien que les lois de commande des variables mécaniques et électriques du système sont implémentés sur un simulateur digital. Fig.V.25 représente le HIL banc expérimental et Fig.V.26 montre les mesures des différents variables du système en simulation et sur le HIL simulateur.

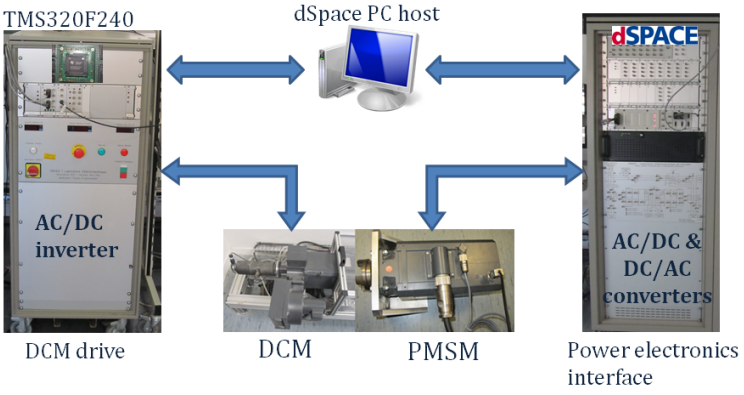

Figure V.25: Représentation du banc expérimental.

V.6 Conclusion

Ceci est un résumé français de thèse intitulé "Optimisation de contrôle commande des systèmes de génération d'électricité à cycle de relaxation". Le résumé a commencé par un introduction du sujet de thèse et focaliser sur la présentation de case d'étude qui est le système de traction à base de cerf-volant (Kite Generator System : KGS). Ce système a été modélisé et deux méthodologies de contrôle étaient présentées afin d'optimiser son orbite et garantir la suivie ainsi que la stabilisation

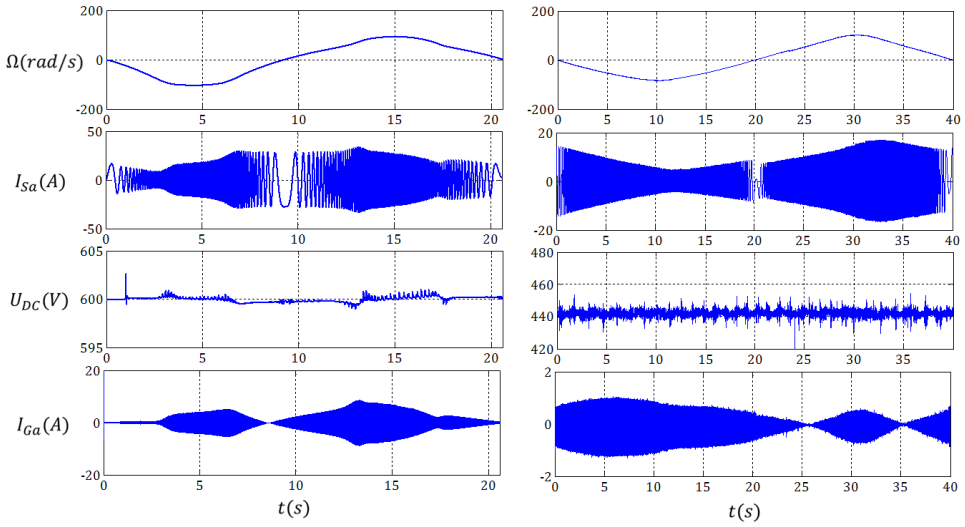

Figure V.26: Validation des chemins de contr ôles: A gauche en simulation, A droite sur le HIL simulateur.

de cerf-volant sur cette orbite.

La première méthode utilise l'approche de commande prédictive (Model predictive control : MPC) qui a était déj à utilisé dans la bibliographie et a montré des résultats très satisfaisant, à part le temps de calcul de contrôle qui est important. La deuxième méthode utilise une nouvelle approche celui de renforcement des contraintes virtuelles (Virtual constraints control : VCC). Cette approche est inspirée de la robotique où elle a été appliquée dans des dizaines des application afin de résoudre les problèmes de mouvement periodic et de stabilité. On a montré la possibilité d'appliquer le VCC sur le système KGS et des résultats prometteurs ont été trouvé.

En suite, le problème d'intégration du système cerf-volant sur le réseau, ce que n'a pas été traité auparavant, a été adressé. L'interface avec le réseau a été présentée ainsi que les chemins de commande complets pour le cas de connection avec un réseau fort infini ou une charge isolée. Le test de ces chemin a été accomplit par les simulation et sur un simulateur Hardware-in-the-loop.

Ce travail est un premier au niveau de la France dans le domaine d'énergie de vent en haut altitude. C'est une base très riche pour démarrer des travaux avenir dans:

- Le contr ôle de la partie volant du syst ème en prenant compte des variation de direction de vent, les perturbation, le vol sans vent, etc.
- L'intégration sur un réseau isolé et prendre en compte l'effet de creux de tension, l'addition d'un stockage qui utilise un flywheel, etc.
- Généraliser les résultats obtenus sur des autre systèmes à cycle de relaxation.

Bibliography

[ABR08] M. Andreica, S. Bacha, and D. Roye, *Micro-hydro water current turbine control for grid connected or islanding operation*, Power Electronics Specialists Conference, 2008. PESC 2008. IEEE, IEEE, 2008, pp. 957–962.

[AC09] C.L. Archer and K. Caldeira, *Global assessment of high-altitude wind power*, Energies **2** (2009), no. 2, 307–319.

[ADS13] U. Ahrens, M. Diehl, and R. Schmehl, *Airborne wind energy*, Springer (2013).

[AHB11a] M.S. Ahmed, A. Hably, and S. Bacha, *Grid-connected kite generator system: Electrical variables control with MPPT*, Industrial Engineering Conference, Melbourne, Australia (2011).

[AHB11b] ———, *Power maximization of a closed-orbit kite generator system*, 50th Conference on Decision and Control Conference (IEEE CDC), Orlando, USA, 2011.

[AHB12] ———, *High altitude wind power systems: A survey on flexible power kites*, International Conference on Electrical machines, Marseille, France (2012).

[AHJ10] K. Aleklett, M. Höök, and K. Jakobsson, *The peak of the oil age–analyzing the world oil production reference scenario in world energy outlook 2008*, Energy Policy **38** (2010), no. 3, 1398–1414.

[AJ05] C.L. Archer and M.Z. Jacobson, *Evaluation of global wind power*, Journal of Geophysical Research **vol.110, D12110** (2005).

[AMBA09] J. Aubry, B. Multon, and H. Ben Ahmed, *Optimisation en couplage fort du pilotage et de la chaîne de conversion tout-électrique du houlogénérateur searev*, Actes d'Électrotechnique du futur (2009).

[AMCHB12] M.S. Ahmed, S.C. Murillo-Cruz, A. Hably, and S Bacha, *A comparative study on a pumping wave energy conversion system*, Industrial Electronics (ISIE), 2012 IEEE International Symposium on, IEEE, 2012, pp. 1419–1424.

[AMCR14] D. Abbes, A. Martinez, G. Champenois, and B. Robyns, *Real time supervision for a hybrid renewable power system emulator*, Simulation Modelling Practice and Theory **42** (2014), 53–72.

[And09] A. M. Andreica, *Optimisation énergetique de chaînes de conversion hydroliennes: modélisation, commandes et réalisations expérimentales*, Ph.D. thesis, PhD dissertation, Grenoble University, 2009.

[ARS09] I. Argatov, P. Rautakorpi, and R. Silvennoinen, *Estimation of the mechanical energy output of the kite wind generator*, Renewable Energy **34** (2009), 1525–1532.

[AS10a] I. Argatov and R. Silvennoinen, *Energy conversion efficiency of the pumping kite wind generator*, Renewable Energy **35(5)** (2010), 1052–1060.

[AS10b] I. Argatov and R. Silvennoinen, *Structural optimization of the pumping kite wind generator*, Structural and Multidisciplinary Optimization **40** (2010), no. 1, 585–595.

[AS13] ———, *Efficiency of traction power conversion based on crosswind motion*, Airborne Wind Energy, Springer, 2013, pp. 65–79.

[Atl] European Wave Energy Atlas.

[AWE10] American Wind Energy Association AWEA, *U.S. wind industry annual market report: year ending 2009*, Washington, D.C. (2010).

[Bal08] G. Baldwin, *Kite power for heifer international's overlook farm*, Ph.D. thesis, Worcester Polytechnic Institute, 2008.

[BBM13] L. Belhadji, S. Bacha, and I. Munteanu, *Adaptive mppt applied to variable-speed microhydropower plant*, Energy Conversion, IEEE Transactions on **28** (2013), no. 1, 34–43.

[BDC04] A. Babarit, G. Duclos, and A.H. Clément, *Comparison of latching control strategies for a heaving wave energy device in random sea*, Applied Ocean Research **26** (2004), no. 5, 227–238.

[BEBC07] S. Ben Elghali, M. Benbouzid, and J. Charpentier, *Marine tidal current electric power generation technology: State of the art and current status*, Electric Machines & Drives Conference, 2007. IEMDC'07. IEEE International, vol. 2, IEEE, 2007, pp. 1407–1412.

[Bel90] R. Beltrán, *Introducción a la mecánica de fluidos*, MacGraw-Hill, 1990.

[BF75] K. Budar and J. Falnes, *A resonant point absorber of ocean-wave power*, Nature **256** (1975), no. 5517, 478–479.

[BO07] J. Breukels and W.J. Ockels, *A multi-body dynamics approach to a cable simulation for kites*, Proceeding of the IASTED Asian Conference on Modelling and Simulation, ACTA Press, 2007, pp. 168–173.

[BO11] J. H. Baayen and W.J. Ockels, *Tracking control with adaption of kites*, IET control theory & applications **6** (2011), no. 2, 182–191.

[Bra10] S. Brabeck, *Skysails–new energy for fishing trawlers*, First International Symposium on Fishing Vessel Energy Efficiency. May, Vigo, Spain, 2010.

[Bre11] J. Breukels, *An engineering methodology for kite design*, Ph.D. thesis, PhD dissertation, Delft, 2011.

[BTDB10] C. Beels, P. Troch, and G. De Backer, *Numerical implementation and sensitivity analysis of a wave energy converter in a time-dependent mild-slope equation model*, Coastal Engineering **57** (2010), no. 5, 471–492.

[Bur63] A. F. Burstall, *A history of mechanical engineering*, M.I.T. Press (Cambridge, Mass), 1963.

[BVJH09] T. Brekken, A. Von Jouanne, and H.Y. Han, *Ocean wave energy overview and research at oregon state university*, Power Electronics and Machines in Wind Applications PEMWA, IEEE, 2009, pp. 1–7.

[BWF02] C.B. Boake, T. Whittaker, and M. Folley, *Overview and initial operational experience of the limpet wave energy plant*, Proceedings of The Twelfth, 2002, pp. 586–594.

[Car] http://www.carnegiewave.com CarnEnergyWave.

[CBG05] A Clément, A Babarit, and JC Gilloteaux, *The searev wave energy converter*, 6th European Wave and Tidal Energy Conference, 2005.

[CdW04] C. Canudas-de Wit, *On the concept of virtual constraints as a tool for walking robot control and balancing*, Annual Reviews in Control **28** (2004), no. 2, 157–166.

[CFBM10] O. Craciun, A. Florescu, S. Bacha, and I. Munteanu, *Hardware-in-the-loop testing of pv control systems using rt-lab simulator*, Power Electronics and Motion Control Conference (EPE/PEMC), 2010 14th International, IEEE, 2010, pp. S2–1.

[CFIM06] M. Canale, L. Fagiano, M. Ippolito, and M. Milanese, *Control of tethered airfoils for a new class of wind energy generator*, Proceedings of the 45th IEEE Conference on Decision and Control, 2006.

[CFM07] M. Canale, L. Fagiano, and M. Milanese, *Power kites for wind energy generation, fast predictive control of tethered airfoils*, IEEE Control Systems Magazine (2007), 25–38.

[CFM10] ———, *High altitude wind energy generation using controlled power kites*, IEEE Transactions On Control Systems Technology **18(2)** (2010), 279 – 293.

[CM10] Luca Consolini and Manfredi Maggiore, *Virtual holonomic constraints for euler-lagrange systems*, Symposium on Nonlinear Control Systems (NOLCOS), 2010.

[CMF02] A. Clément, P. McCullen, and A. Falcão, *Wave energy in europe: current status and perspectives*, Renewable and Sustainable Energy Reviews **6** (2002), no. 5, 405–431.

[DBS05] M. DIEHL, H.G. BOCK, and J.P. SCHLODER, *A real-time iteration scheme for nonlinear optimization in optimal feedback control*, SIAM J. CONTROL OPTIM. **43(5)** (2005), 1714ï¿½1736.

[dHAEO06] A. de Heredia, P. Antoniewicz, and I. Etxeberria-Otadui, *A comparative study between the dpc-svm and the multi-resonant controller for power active filter applications*, Industrial Electronics, 2006 IEEE International Symposium on, vol. 2, IEEE, 2006, pp. 1058–1063.

[Die01] M. Diehl, *Real time optimization for large scale nonlinear processes*, Ph.D. thesis, University of Heidelburg, 2001.

[Dra61] A.G. Drachmann, *Heron's windmill*, Centaurus **7** (1961), 145–151.

[Dun14] Storm Dunker, *Ram-air wing design considerations for airborne wind energy*, Airborne Wind Energy, Springer, 2014, pp. 517–546.

[Fag09] L. Fagiano, *Control of tethered airfoils for high altitude wind energy generation*, Ph.D. thesis, Politechnico di Torino - Doctoral School, 2009.

[Fal02] J. Falnes, *Ocean waves and oscillating systems: linear interactions including wave-energy extraction*, Cambridge Univ Pr, 2002.

[Fal07] Johannes Falnes, *A review of wave-energy extraction*, Marine Structures **20** (2007), no. 4, 185–201.

[Fal10] A. Falcão, *Wave energy utilization: A review of the technologies*, Renewable and sustainable energy reviews **14** (2010), no. 3, 899–918.

[FBMB12] A. Florescu, S. Bacha, I. Munteanu, and A. Bratcu, *Results concerning ultracapacitor-based energy management strategy within electric vehicles*, System Theory, Control and Computing (ICSTCC), 2012 16th International Conference on, IEEE, 2012, pp. 1–7.

[FH07] A. Furey and I. Harvey, *Evolution of neural networks for active control of tethered airfoils*, Advances in Artificial Life (2007), 746–755.

[FHGD11] H.J. Ferreau, B. Houska, K. Geebelen, and M. Diehl, *Real-time control of a kite-model using an auto-generated nonlinear mpc algorithm*, Proc. of the IFAC World Congress, vol. 18, 2011.

[Fin08] M. Finley, *The oil market to 2030: Implications for investment and policy*, Economics of Energy and Environmental Policy **1** (2008), no. 1.

[FJH09] A. Falcão, P. Justino, and J. Henriques, *Reactive versus latching phase control of a two-body heaving wave energy converter.*

[Flo10] *The race for great lakes wind power*, Lilith News (July 2010).

[FMP09] L. Fagiano, M. Milanese, and D. Piga, *High-altitude wind power generation for renewable energy cheaper than oil*, in Sustainable development: a challenge for European research, Brussels, May 2009.

[FMP10] L. Fagiano, M. Milanese, and D. Piga, *High-altitude wind power generation*, Energy Conversion, IEEE Transactions on **25** (2010), no. 1, 168–180.

[FMP11] ———, *Optimization of airborne wind energy generators*, International Journal of Robust and Nonlinear Control (2011).

[Fri10] D. Fridley, *Nine challenges of alternative energy*, The post carbon reader: managing the **21** (2010).

[FRSJ08] L. Freidovich, A. Robertsson, A. Shiriaev, and Rolf Johansson, *Periodic motions of the pendubot via virtual holonomic constraints: Theory and experiments*, Automatica **44** (2008), no. 3, 785–791.

[FS12] U. Fechner and R. Schmehl, *Design of a distributed kite power control system*, IEEE International Conference on Control Applications (CCA), Dubrovnik, Croatia (2012).

[FTBV11] A. Florescu, H. Turker, S. Bacha, and E. Vinot, *Energy management system for hybrid electric vehicle: Real-time validation of the vehlib dedicated library*, Vehicle Power and Propulsion Conference (VPPC), 2011 IEEE, IEEE, 2011, pp. 1–6.

[Gam07] V.K. Gam, *The lanchester−betz−joukowsky limit*, Wind Energy, John Wiley and Sons, (2007).

[GBS10] S. Groot, J. Breukels, and R. Schmehl, *Multibody system reduction for derivation of a flight dynamics model for real-time control of kites*, Submitted to AIAA Journal of Guidance, Control and Dynamics (2010).

[GEOBR06] H. Gaztanaga, I. Etxeberria-Otadui, S. Bacha, and D. Roye, *Real-time analysis of the control structure and management functions of a hybrid microgrid system*, IEEE Industrial Electronics, IECON 2006-32nd Annual Conference on, IEEE, 2006, pp. 5137–5142.

[GHG10] R. Gomes, J. Henriques, and L. Gato, *Ips 2-body wave energy converter: acceleration tube optimization*, International Journal of Offshore and Polar Engineering **20** (2010), no. 4, 247–255.

[Gom] David Gomberg, *Kite history: A simple history of kiting, http://www.gombergkites.com/nkm/hist1.html.*

[GRBB11] M. Gonzalez, B. Raison, S. Bacha, and L. Bun, *Fault diagnosis in a grid-connected photovoltaic system by applying a signal approach*, IECON 2011-37th Annual Conference on IEEE Industrial Electronics Society, IEEE, 2011, pp. 1354–1359.

[Gri09] S. Griffith, *Saul griffith on kites as the future of renewable energy*, TED Talks (2009).

[HD06] B. Houska and M. Diehl, *Optimal control of towing kites*, 45th IEEE Conference on Decision and Control, pages 2693-2697, San Diego, CA, USA 2006.

[HD07] ———, *Optimal control for power generating kites.*

[HD10] ———, *Robustness and stability optimization of power generating kite systems in a periodic pumping mode*, IEEE Multi - Conference on Systems and Control, 2010, pp. 2172–2177.

[HLAD13] A. Hably, R. Lozano, M. Alamir, and J. Dumon, *Observer-based control of a tethered wing wind power system : indoor real-time experiment*, ACC - American Control Conference, Washington, DC, USA, June 2013.

[HR11] L. Hughes and J. Rudolph, *Future world oil production: growth, plateau, or peak?*, Current Opinion in Environmental Sustainability **3** (2011), no. 4, 225–234.

[Hus02] M. Hussain, *Dependence of power law index on surface wind speed*, Energy conversion and management **43** (2002), no. 4, 467–472.

[IEA11] IEA, *CO2 emissions from fuel combustion highlights 2011.*

[IHD07] A. Ilzhofer, B. Houska, and M. Diehl, *Nonlinear MPC of kites under varying wind conditions for a new class of large-scale wind power generators*, International Journal Of Robust And Nonlinear Control **17** (2007), 1590–1599.

[Ipp08] M. Ippolito, *Vertical axis wind turbine with control system steering kites*, February 27 2008, EP Patent 1,672,214.

[JE] http://www.jobyenergy.com/ Joby Energy.

[KAB08] J. Krenciszek, S. Akindeinde, and H. Braun, *Mathematical modeling of the pumping kite wind generator: Optimization of the power output*, URL: http://www.win.tue.nl/casa/meetings/special/ecmi08/pumping-kite.pdf, 2008.

[KI98] A. Kolmogorov and A. Iushkevich, *Mathematics of the 19th century: Function theory according to chebyshev, ordinary differential equations, calculus of variations, theory of finite differences. iii*, vol. 3, Springer, 1998.

[KS46] R. Kloeffler and E. Sitz, *Electric energy from winds*, The College, 1946.

[LJADH12] R. Lozano Jr, M. Alamir, J. Dumon, and A. Hably, *Control of a wind power system based on a tethered wing*, IFAC second EGNCA, Bangalore, India (2012).

[LO05] B. Lansdorp and W.J. Ockels, *Comparison of concepts for high-altitude wind energy generation with ground based generator*, Proceedings of the NRE 2005 Conference, Beijing, China, 2005, pp. 409–417.

[Loy80] M.L. Loyd, *Crosswind kite power*, J. ENERGY **4(3)** (1980).

[LP08] D. Lacroix and M. Paillard, *L'avenir des énergies renouvelables marines. synthèse de l'étude prospective ifremer sur les énergies renouvelables marines à l'horizon 2030*, Futuribles (2008), no. 345, 43–60.

[LRO05] B. Lansdorp, B. Remes, and W.J. Ockels, *Design and testing of a remotely controlled surfkite for the laddermill*, World Wind Energy Conference, Melbourne, Australia, 2005.

[LW06] B. Lansdorp and P. Williams, *The laddermill - innovative wind energy from high altitudes in holland and australia*, Windpower 06, Adelaide, Australia, 2006.

[mak] *Makani power, http://www.makanipower.com/.*

[Mar13] D. Markovic, *The second industrial revolution*, 2013.

[MBAB10] I. Munteanu, A. Bratcu, M. Andreica, and S. Bacha, *A new method of real-time physical simulation of prime movers used in energy conversion chains*, Simulation Modelling Practice and Theory **18** (2010), 1342–1354.

[MBB10] I. Munteanu, A.I. Bratcu, and S. Bacha, *Hardware-in-the-loop-based simulator for a class of variable-speed wind energy conversion systems: Design and performance assessment*, IEEE Transactions On Energy Conversion **25** (JUNE 2010), 564–576.

[MBBG07] I. Munteanu, S. Bacha, I.A. Bratcu, and J. Guiraud, *Conception systématique des simulateurs temps réel hardware-in-the-loop: Application aux systèmes de conversion éolienne*, Journal européen des systèmes automatisés **41** (2007), no. 9-10, 1139–1164.

[MBBR10] I. Munteanu, A.I. Bratcu, S. Bacha, and D. Roye, *Hardware-in-the-loop-based simulator for a class of variable-speed wind energy conversion systems: Design and performance assessment*, Energy Conversion, IEEE Transactions on **25** (2010), no. 2, 564–576.

[McC74] M.E. McCormick, *Analysis of a wave energy conversion buoy*, Journal of Hydronautics **8** (1974), no. 3, 77–82.

[Meg] *Magenn, http://www.magenn.com/.*

[MOS99] J.P. Meijaard, W.J. Ockels, and A.L. Schwab, *Modelling of the dynamic behaviour of a laddermill, a novel concept to exploit wind energy*, Proceedings of the III Symposium on Cable Dynamics, 1999, pp. 229–234.

[Mul03] B. Multon, *Production d'énergie électrique par sources renouvelables*, Techniques de l'ingénieur. Génie électrique **8** (2003), no. D4005, D4005–1.

[mun]

[NFM11] C. Novara, L. Fagiano, and M. Milanese, *Direct data-driven inverse control of a power kite for high altitude wind energy conversion*, IEEE International Conference on Control Applications (CCA), 2011, pp. 240–245.

[Ock96] W.J. Ockels, *Patent 1004508*, no. 1004508.

[Ock01] _____, *Laddermill, a novel concept to exploit the energy in the airspace*, Aircraft Design **4** (2001), 81–97.

[Ock06] W.J. Ockels, *Laddermill-sailing, ship propulsion by wind energy independent from the wind direction!*

[OG08] D. Olinger and J.S. Goela, *Performance characteristics of a one-kilowatt scale kite power system*, Proceedings of Energy Sustainability (2008).

[OGBR08] D. Ocnasu, C. Gombert, S. Bacha, and D. Roye, *Real-time hybrid facility for the study of distributed power generation systems*, Revue des Energies Renouvables **11** (2008), 343–356.

[OS92] R. Outbib and G. Sallet, *Stabilizability of the angular velocity of a rigid body revisited*, Systems & Control Letters **18** (1992), no. 2, 93–98.

[Pet10] Global British Petroleum, *Bp statistical review of world energy*, 2010.

[PO06] A.R. Podgaets and W.J. Ockels, *Three-dimensional simulation of a laddermill*, Proceedings of the 3rd Asian Wind Power Conference, Beijing, China, 2006.

[PO07a] ———, *Flight control of the high altitude wind power system*, Proceedings of the 7th Conference on Sustainable Applications for Tropical Island States, 2007.

[PO07b] ———, *Robust control of laddermill wind energy system*, Proceedings of the Wind Power Shanghai Conference, China, 2007.

[RBMJ10] M. Ruellan, H. BenAhmed, B. Multon, and C. Josset, *Design methodology for a searev wave energy converter*, Energy Conversion, IEEE Transactions on **25** (2010), no. 3, 760–767.

[SCdW03] A. Shiriaev and C. Canudas-de Wit, *Virtual constraints: a constructive tool for orbital stabilization of under-actuated nonlinear systems*, Personal Communication (2003).

[Sch12] R. Schmehl, *Large-scale power generation with kites*, Leonardo Times (2012), 21–22.

[SFG10] A. Shiriaev, L. Freidovich, and S. Gusev, *Transverse linearization for controlled mechanical systems with several passive degrees of freedom*, IEEE Transactions on Automatic Control **55** (2010), no. 4, 893–906.

[Skya] *Sky wind power, http://www.skywindpower.com/.*

[Skyb] *Skysails, http://www.skysails.info.*

[SPCdW05] A. Shiriaev, J.W. Perram, and C. Canudas-de Wit, *Constructive tool for orbital stabilization of underactuated nonlinear systems: Virtual constraints approach*, Automatic Control, IEEE Transactions on **50** (2005), no. 8, 1164–1176.

[SRPS05] A. Shiriaev, A. Robertsson, J. Perram, and A. Sandberg, *Periodic motion planning for virtually constrained (hybrid) mechanical systems*, CDC-ECC'05 - 44th IEEE Conference on Decision and Control, European Control Conference, Seville, Spain, IEEE, December 2005, pp. 4035–4040.

[SRPS06] A Shiriaev, A Robertsson, J Perram, and A Sandberg, *Periodic motion planning for virtually constrained euler–lagrange systems*, Systems & control letters **55** (2006), no. 11, 900–907.

[Str11] E. Strickland, *Explainer: What went wrong in japan's nuclear reactors*, IEEE Spectrum (13 May 2011).

[Swi] *Swiss kite power, http://www.swisskitepower.ch.*

[Tju94] K.J. Tjugen, *Tapchan ocean wave energy project*, Proc. European Wave Energy Symposium, Edinburgh, Scotland, ISBN 0-903640-84-8, 1994, pp. 265–270.

[TKKFM06] J. Tedd, J.P. Kofoed, W. Knapp, and E. Friis-Madsen, *Wave dragon: prototype wave power production.*

[TPK09] J. Tedd and J. Peter Kofoed, *Measurements of overtopping flow time series on the wave dragon, wave energy converter*, Renewable Energy **34** (2009), no. 3, 711–717.

[TRV07] R. Thresher, M. Robinson, and P. Veers, *To capture the wind*, IEEE power & energy magazine (2007), 34–46.

[Ver] G. Vergnano, *High altitude wind generation: The rotokite*, SEQUOIA IT.

[Win] *Windlift, http://www.windlift.com.*

[WLO07a] P. Williams, B. Lansdorp, and W. Ockels, *Modeling and control of a kite on a variable length flexible inelastic tether*, AIAA Guidance, navigation and control conference, South Carolina, USA, 2007.

[WLO07b] P. Williams, B. Lansdorp, and W. Ockels, *Optimal cross-wind towing and power generation with tethered kites*, AIAA Guidance, Navigation and Control Conference and Exhibit, 2007.

[WLRO08] P. Williams, B. Lansdorp, R. Ruiterkamp, and W. Ockels, *Modeling, simulation, and testing of surf kites for power generation*, No. AIAA **6693** (2008).

[WMS10] S. Westerberg, U. Mettin, and A. Shiriaev, *Motion planning and control of an underactuated 3dof helicopter*, IROS - IEEE/RSJ Intelligent Robots and Systems, Leiden, Netherlands, IEEE, June 2010, pp. 3759–3764.

[WST08] P. Williams, D. Sgarioto, and P.M. Trivailo, *Constrained path-planning for an aerial-towed cable system*, Aerospace Science and Technology **12** (2008), no. 5, 347–354.

[YHT00] R.W. Yemm, R.M. Henderson, and C. Taylor, *The opd pelamis wec: Current status and onward programme*, Proc. 4th European Wave Energy Conference, Alborg Denmark, 2000.

Publications

International journals

Mariam Ahmed, Ahmad Hably, Seddik Bacha, *Kite Generator System Modeling and Grid Integration*, Sustainable Energy, IEEE transactions on, Vol 4, No 4, Octobre 2013, Pages 968-976.

International conferences

Mariam Ahmed, Ahmad Hably, Seddik Bacha, *Kite Generator System Periodic Motion Planning Via Virtual Constraints*, IECON 2013 - 39th Annual Conference of the IEEE Industrial Electronics Society, Austria-Vienna, Pages 1-6.

Mariam Ahmed, S-C Murillo-Cruz, Ahmad Hably, Seddik Bacha, *A comparative study on a pumping wave energy conversion system*, Industrial Electronics (ISIE), 2012 IEEE International Symposium on, China- Hangzhou, Pages 1419-1424.

Mariam Ahmed, Ahmad Hably, Seddik Bacha, *High altitude wind power systems: A survey on flexible power kites*, Electrical Machines (ICEM), 2012 XXth International Conference on, France-Marseilles, Pages 2085-2091.

Mariam Ahmed, Ahmad Hably, Seddik Bacha, *Grid-connected kite generator system: Electrical variables control with MPPT*, IECON 2011 - 37th Annual Conference on IEEE Industrial Electronics Society, Australia-Melbourne, Pages 3152-3157.

Mariam Ahmed, Ahmad Hably, Seddik Bacha, *Power maximization of a closed-orbit kite generator system*, Decision and Control and European Control Conference (CDC-ECC), 2011 50th IEEE Conference on, USA-Orlando, Pages 7717-7722.